JYU DISSERTATIONS 602

Alejandro Ortiz Cortes

Palladium: a Study of Nuclear Deformation of a Refractory Element

Laser Spectroscopy at the IGISOL (Jyväskylä, Finland) and S3-LEB (GANIL, France)

JYU DISSERTATIONS 602

Alejandro Ortiz Cortes

Palladium: a Study of Nuclear Deformation of a Refractory Element

Laser Spectroscopy at the IGISOL (Jyväskylä, Finland) and S3-LEB (GANIL, France)

Academic dissertation to be publicly discussed, by permission of
the Faculty of Mathematics and Science of the University of Jyväskylä,
at at the guest house of Ganil, Normandy University, on January 26, 2023.

JYVÄSKYLÄ 2023

Editors
Ilari Maasilta
Department of Physics, University of Jyväskylä
Ville Korkiakangas
Open Science Centre, University of Jyväskylä

ISBN 978-951-39-9287-3 (PDF)
URN:ISBN:978-951-39-9287-3
ISSN 2489-9003

Permanent link to the online version of this publication: http://urn.fi/URN:ISBN:978-951-39-9287-3

ABSTRACT

At this work, laser spectroscopy measurements on the Pd isotopic chain using different techniques are presented. Thanks to the chemically insensitive IGISOL ion-guide production method, it has been possible to reduce the existing gap in optical spectroscopy data below Z=50, created by the refractory character of these elements. A study of the deformation of palladium nuclei on the mass region $98 \leq A \leq 118$ is performed comparing the results of two collinear laser spectroscopy measurements with state-of-art Fayans and Gogny calculations.

Having 6 protons and 4 holes on his valence shell, palladium is located at the mid-shell $\pi g_{9/2}$, between the strongly deformed systems around zirconium (Z=40, N=60) and the spherical systems close to tin (Z=50), and are thus expected to exhibit a rather transitional character. The interpretation of the results have been done using axial and triaxial perspectives. The mean square charge radii have been extracted for the ground state of the even-even palladium isotopes on the mass region $98 \leq A \leq 118$ and together with the magnetic dipole moments, electric quadrupole moments, nuclear spins and mean square charge radii of the odd-A ^{99,101,113,115}Pd and the isomeric state of ^{115}Pd.

Complementing this work, this thesis includes the work with Fabry-Pérot interferometers to support laser spectroscopy measurements.

To prepare future experiments towards the proton drip line, laser resonant ionization spectroscopy measurements of stable palladium isotopes have been performed suing two different approaches. On one side, the production study of stable palladium production test using a hot-cavity catcher is presented. On the other side, the offline test and development of resonant ionization palladium schemes has been performed at the GISELE offline laser laboratory.

Résumé

Dans ce travail, des mesures par spectroscopie laser sur la chaîne isotopique du Pd utilisant différentes techniques sont présentées. Grâce à la méthode de production de guides d'ions IGISOL chimiquement insensibles, il a été possible de réduire l'écart existant dans les données de spectroscopie optique en dessous de Z = 50, créé par le caractère réfractaire de ces éléments. Une étude de la déformation des noyaux de palladium sur la région de masse $98 \leq A \leq 118$ est effectuée en comparant les résultats de deux mesures de spectroscopie laser colinéaire avec des calculs de Fayans et Gogny de pointe.

Possédant 6 protons et 4 trous sur sa couche de valence, le palladium se situe au milieu de la couche $\pi g_{9/2}$, entre les systèmes fortement déformés autour du zirconium (Z=40, N=60) et les systèmes sphériques proches de l'étain (Z=50), et devraient donc présenter un caractère plutôt transitoire. L'interprétation des résultats a été faite en utilisant des perspectives axiales et triaxiales. Les rayons de charge carrés moyens ont été extraits pour l'état fondamental des isotopes pairs-pairs du palladium sur la région de masse $98 \leq A \leq 118$ et avec les moments dipolaires magnétiques, les moments quadripolaires électriques, les spins nucléaires et les rayons de charge carrés moyens de l'od-A ^{99,101,113,115}Pd et l'état isomérique de ^{115}Pd.

En complément de ces travaux, cette thèse inclut le travail avec les interféromètres Fabry-Pérot pour supporter les mesures de spectroscopie laser.

Afin de préparer les futures expériences vers la ligne d'égouttement de protons, des mesures par spectroscopie d'ionisation résonnante laser des isotopes stables du palladium ont été réalisées selon deux approches différentes. D'un côté, l'étude de production d'un test de production stable de palladium à l'aide d'un capteur à cavité chaude est présentée. D'autre part, le test hors ligne et le développement des schémas d'ionisation résonante du palladium ont été réalisés au laboratoire laser hors ligne GISELE.

Tiivistelmä

Tässä työssä esitellään palladiumin radioaktiivisille isotoopeille eri tekniikoilla tehtyjä laserspektroskopiamittauksia. Palladiumisotoopit tuotettiin kemiallisesti epävalikoivalla IGISOL ioniohjainmenetelmällä, jolla voidaan tuottaa protoniluvun Z=50 alla olevia vaikeasti irtoavia ytimiä, joita ei ole ennen tutkittu optisin menetelmin. Palladiumytimien muodonmuutosta massa-alueella $98 \leq A \leq 118$ tutkitiin vertaamalla kahden kollineaarisen laserspektroskopiamittauksen tuloksia viimeisimpiin Fayansin ja Gognyn funktionaaleilla tehtyihin teoreettisiin laskelmiin.

Palladiumin valenssikuori muodostuu kuudesta protonista sekä 4 reiästä. Se sijaitsee $\pi g_{9/2}$ keskikuorella, zirkoniumia lähellä olevien voimakkaasti muotoutuneiden ydinjärjestelmien (Z=40, N=60), sekä pallomaisten lähellä tinaa (Z=50) olevien järjestelmien välissä. Tämän takia palladiumisotooppien odotetaan ilmentävän transitionaalisia ominaisuuksia. Tässä työssä saatuja tuloksia on tulkittu aksiaalisesta sekä triaksiaalisesta näkökulmasta. Keskimääräiset neliölliset varaussäteet on mitattu parillis-parillisten palladiumisotooppien perustiloille massa-alueella $98 \leq A \leq 118$. Magneettiset dipolimomentit, sähköiset kvadrupolimomentit, ydinspinit ja keskimääräinen neliöllinen varaussäde mitattiin paritonmassaisille ^{99101113115}Pd isotoopeille. Lisäksi määritettiin ^{115}Pd isomeerisen tilan säde. Nämä uudet tulokset keskimääräisistä neliöllisistä varaussäteistä ja kvadrupolimomenteista valaisevat ytimien muodon kehitystä palladiumin isotooppiketjussa. Tuloksissa voidaan nähdä viitteitä, että mitattujen neutronirikkaan ytimien muodonmuutos on luonteeltaan pehmeä.

Laserspektroskopiatyön lisäksi tähän opinnäytetyöhön sisältyy kehitystyötä Fabry-Pérot-interferometreillä, joita tullaan käyttämään tulevissa tulevia laserspektroskopiamittauksissa. Lisäksi tulevien protoni drip-linjaa koskevien kokeiden valmistelemiseksi stabiilien palladiumisotooppien laser resonanssi-ionisaatio spektroskopia mittauksia on suoritettu kahdella eri lähestymistavalla. Ensimmäisellä näistä tutkittiin stabiilien palladiumisotooppien tuotantoas kuumaalla ontelosiepparilla. Toisella lähestymistavalla kehitettiin palladiumin resonanssi-ionisaatiomenetelmiä GISELE-offline laserlaboratoriossa, tarkoituksena etsiä siirtymiä, jotka olisivat tarpeeksi herkkiä ydinten tutkimiseen.

Author Alejandro Ortiz Cortés
GANIL
Caen, France

Department of Physics
University of Jyväskylä
Jyväskylä, Finland

Supervisors Dr. Lucia Caceres
GANIL
Caen, France

Prof. Iain Moore
Department of Physics
University of Jyväskylä
Jyväskylä, Finland

Dr. Herve Savajols
GANIL
Caen, France

Reviewers Prof. Michael Block
Johannes Gutenberg-Universität Mainz
Mainz, Germany

Dr. David Verney
Université Paris Saclay
Paris, France

Opponents

Prof. Michael Block
Johannes Gutenberg-Universität Mainz
Mainz, Germany

Dr. David Verney
Université Paris Saclay
Paris, France

Contents

Chapter 1

Introduction

Since the discovery of the atomic nucleus by Rutherford in 1911, nuclear physics has attracted the attention of many experimentalists and theorists. At the beginning of the field, the measurement of stable and long live isotopes presented a rich picture of nuclear properties. This early work provided the basis of nuclear theory due to the development of the nuclear shell model, which successfully described many of these properties and gave birth to the magic numbers.

The creation of radioactive ion beam facilities allowed access to a new world of isotopes far from stability. This lead to the observation of many fascinating phenomenon, which, even now, challenge our understanding. One example is the variety of different shapes and sizes that the nucleus can exhibit together their evolution.

From one side, the atomic nuclei can present various shapes beyond spherical: prolate [1], oblate [2], pear-shaped [3] or halo nuclei [4]. From the other side, the different shapes are not exclusive, being possible the coexistence [5] and the rapid changes [6] between them.

High-resolution laser spectroscopy has long been established as a powerful tool in the study of nuclear shape. Laser spectroscopy techniques provide access to model-independent nuclear data through the interplay between atomic electrons and nucleon structures, tracking nuclear spins, moments and charge radii across long chains of isotopes [7]. Nevertheless, there are existing gaps in optical spectroscopy data of radioactive nuclei, due to the challenges on their production. One of them is located on the region from Z=43 to Z=47, due to the refractory character of these elements. Palladium (Z=46) is located alongside this elements.

The contribution of this thesis lies in the measurement of spins, changes in the mean-squared charge radius and electromagnetic moments of palladium in the mass range $98 \leq A \leq 118$. This thesis is structured as follows.

In chapter 2, the nuclear background needed to understand this thesis is presented. The chapter is divided in three sections. The first section provide provide an insight on the nuclear models and calculations used for this work. The second section introduce the nuclear observables studied. And the third section consist on an overview of physical phenomenon present at the region of the nuclear chart where palladium is located.

In chapter 3, different concepts from laser spectroscopy are presented. Atomic structure and atomic-nuclear interaction provide an understanding on isotope shift and hyperfine splitting and the introduction on laser optics presents the basis of laser wavelength generation and selection. Finally, the chapter ends with an introduction and comparison between the different laser spectroscopy techniques.

In chapter 4, the different experimental setups used at this work are presented. Chapter 5 contains the work performed with Fabry-Pérot interferometers to support laser spectroscopy measurements.

Chapter 6 focus on the analysis of the collinear fluorescence laser spectroscopy experiment performed at the IGISOL facility in Jyväskylä, Finland. The interpretation of the results of the measurements are presented at chapter 7.

The thesis ends at chapter 8 with an outline of the future measurements which will complement this thesis, including the preparation that has been already been done.

Chapter 2

Nuclear structure

2.1 Nuclear models

2.1.1 Introduction to nuclear models

The atomic nucleus is a complex many-body system with protons and neutrons interacting with each other. The nucleus behave as a N-body quantum system, where N is the number of nucleons described by their wave-function Ψ [8]. The nuclear Hamiltonian is composed by the sum of kinetic energy T of the individual particles and the potential energy $\hat{V}$, coming from the interaction between the N-particles. The nuclear Hamiltonian be mathematically described using the Schrödinger equation:

$$T = \sum_{i}^{N} -\frac{\hbar^2}{2m_i}\nabla^2 \qquad \hat{V} = \sum_{i<j}^{N} v_{i,j} + \sum_{i<j<k}^{N} v_{i,j,k} + \sum_{i<j<k<l}^{N} v_{i,j,k,l} \ ...$$

$$(T + \hat{V})|\Psi\rangle = E|\Psi\rangle \tag{2.1}$$

The equation will have solutions only for certain values of the energy E, which will correspond with the different nuclear levels (the level with minimum energy will become the ground state). In order to obtain the energy of the levels, Equation 2.1 requires accurate formulation of the contributions from all N-body interactions generated by three different forces (strong, weak and electromagnetic). To describe

the nuclear force, dedicated experiments are performed to study specific properties of the nucleus and to test and benchmark state of art nuclear theories.

Magic numbers and mean field potential

The initial attempts of solving the Schrödinger equation based on atomic theory where hindered by the absence of a potential created by an external agent [8]. The introduction of the self-consistent potential by the shell model allowed to rewrite the many-body problem as a simple system where the nucleons move independently in an average potential created by other nucleons (self-consistent field). The Hamiltonian is reduced to an independent particle motion under an external field and a residual interaction treated as a perturbation [9]:

$$H = H_{MF} + H_{res} \tag{2.2}$$

$$H_{MF} = T + U \qquad H_{res} = V - U$$

The mean potential, U, will be optimal when minimizes the residual interaction, being closer to the sum of all free nucleon-nucleon interaction V. Originally, this field was considered static and spherical, being constant up to the nuclear radii and zero outside.

The potential looked to reproduce the gaps related with the single particle level energies at the magic numbers. The harmonic oscillator was chosen as the central potential for two principle reasons: It provides a remarkably good approximate solution to many nuclear problems and it is particularly easy to handle mathematically [10].

$$V(r) = \frac{1}{2}M\omega^2 r^2 \qquad E_{nl} = (2n + l - \frac{1}{2})\hbar\omega \tag{2.3}$$

The harmonic oscillator potential was found not enough to reproduce the nuclear potential. The l^2 term was added to enhance the attractive behavior of the nuclear force. The introduction of the spin-orbit interaction by Maria Goeppert Mayer and J. Hans D. Jensen had a relevant role on the formulation of the magic numbers [11] and leaded to an accurate description of the nuclear masses and binding energies for stable isotopes.

The spin-orbit interaction is the coupling of the intrinsic spin of the nucleon ($s = 1/2$) and the orbital angular momentum l giving rise to the total angular momentum $j = l + s$. The energy split of the levels due to the spin-orbit term is given by the formula:

$$\langle \overrightarrow{l} \cdot \overrightarrow{s} \rangle_{j=l+1/2} - \langle \overrightarrow{l} \cdot \overrightarrow{s} \rangle_{j=l-1/2} = \frac{\hbar^2}{2}(2l+1) \tag{2.4}$$

Therefore, due to the spin-orbit term, the force felt by a nucleon differs according to whether its spin and orbital angular momenta are aligned parallel or antiparallel. This results on a rearrangement of the shell levels to obtain the magic numbers. The central potential on the shell model can be describes as a surface-corrected, isotropic harmonic oscillator, plus a strong attractive spin-orbit term [12]:

$$U(r) = \frac{1}{2}\hbar\omega r^2 + D\overrightarrow{l}^2 + C\overrightarrow{l} \cdot \overrightarrow{s} \tag{2.5}$$

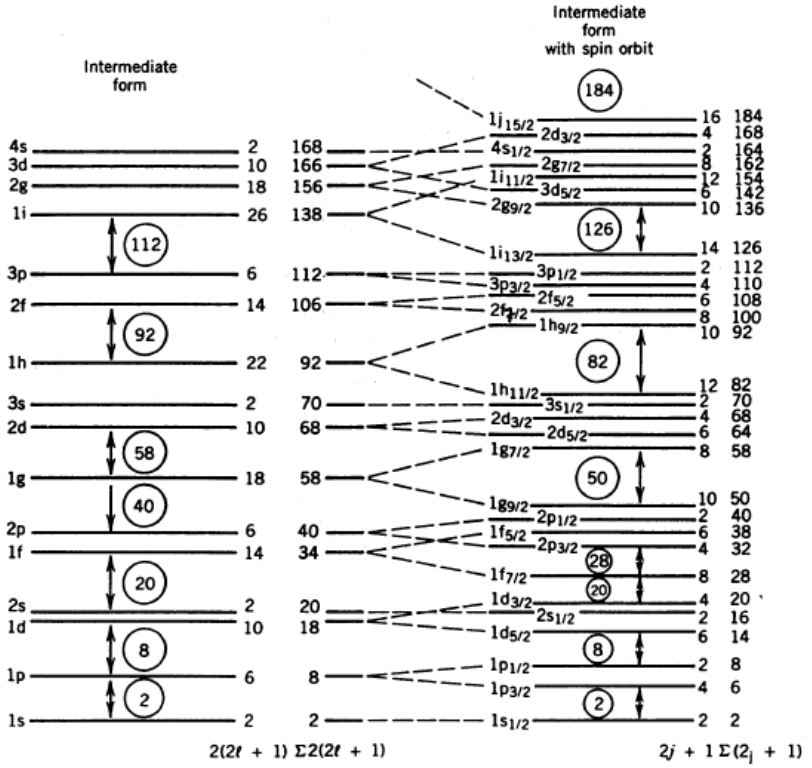

Figure 2.1: *Shell model level scheme with and without the spin-orbit term [10]*

The mean field potential can be calculated self-consistently, on example is the commonly used Hartree–Fock method [13, 14]. During the process, the Slater determinants are used to calculate the energy of the levels, using the antisymmetrized wave-functions $\phi_{\alpha i}$ of the given single-particle states with a normalization factor A:

$$E_{gs} \;=\; \langle \Psi_0 | H | \Psi_0 \rangle \qquad\qquad \Psi_0(r_1, r_2, ..., r_N) \;=\; A \prod_{i=1}^{N} \phi_{\alpha i}(r_i) \tag{2.6}$$

The selection of the optimal one-quasi-particle states can be determined by minimizing the ground-state energy E_{gs} using a Rayleigh-Ritz variational approximation [15] with a consistent iteration method:

$$\phi_\alpha(r) \;\longrightarrow\; \phi_\alpha(r) + \delta\phi_\alpha(r) \tag{2.7}$$

Leading to a Schrödinger equation [16] where the simple potential term has been replaced by the mean field functional of the unknown wave functions ($V_{H(F)}(\{\phi_i(r)\})$):

$$-\frac{\hbar^2}{2m_i}\nabla^2\phi_\alpha(r) \;+\; V_{H(F)}(\{\phi_i(r)\})\phi_\alpha(r) \;=\; \epsilon_i\phi_\alpha(r) \tag{2.8}$$

Nuclear density functional theory

From the section above, the mean field potential can be understood as a single-particle potential which represents the interaction between one nucleon and the remainder of the nucleus. The motion of a nucleon in such potential can be inferred from the effective mass m^* [17]. This effective mass is dependent on the level density, however this relation does not appear within the simple Hartree-Fock method [18]. As a consequence, in order to improve the reproduction of empirical nuclear data, a density-dependent effective nucleon-nucleon interaction was introduced on the mean field Hamiltonian:

$$E[\rho] \;=\; \langle \Phi | H[\rho] | \Phi \rangle \;=\; \int \xi(r) d^3r \tag{2.9}$$

Two examples of commonly used effective nucleon-nucleon interactions with a density-dependent term are the Gogny Force [19] and the Skyrme force [20].

At Equation 2.9, the total energy E is written in terms of the energy density ξ, called energy density functional (EDF). This term mimic many-body correlations as effect of nucleonic densities and currents. The EDF can be directly parameterised in terms of local densities [21], instead of using a density-dependent interaction. Generally, EDF use the binding energy to minimize their errors respect very accurate experimental data. After parameterization, the nuclear EDF must remain invariant under parity, isospin, rotational, translational or time-reversal transformations [18]. One example of this class of EDF is Fayans functionals [22].

2.1.2 Nuclear calculations

During this section, the theoretical calculations which have been used to interpret the experimental results obtained by this work will discussed.

Fayans functionals

Fayans EDF is an universal nuclear density functional developed with the aim of improve the description of nuclear masses and radii and describing not only atomic nuclei but also objects such as neutron stars [23].

On classic Fayans functionals, the density functional can be decomposed into volume, surface, and spin-orbit terms [24]:

$$\xi_{Fy} = \xi^{v}_{Fy}(\rho) + \xi^{s}_{Fy}(\rho) + \xi^{ls}_{Fy}(\rho, J) \tag{2.10}$$

The density gradient dependency on the surface and spin-orbit terms, makes Fayans a sensitive and flexible functional to study odd-even effects on mass and charge radii [25].

As mention above, the parameterization on EDF is performed using the binding energy of previously measured nuclei. The binding energy is calculated with the Fayans functional plus three terms representing the kinetic energy, Coulomb and pairing:

$$E^{Fy} = \epsilon^{kin} + \int d^3r \xi^{Fy} + \epsilon^{coul} + \epsilon^{pair} \tag{2.11}$$

Starting from the first functional FaNDF0 [23], versions with different specifications and parameterizations have been developed leading to the most recent Fy(std) [24] and Fy(Δr,HFB) [26].

Fy(std) and Fy(Δr,HFB) are not calculated purely as a Fayans functional being a mixed functional, taking the kinetic energy and Coulomb terms directly from Skyrme EDF and the volume and surface terms remaining from FaNDF0.

These functionals has been calculated using HF+BCS [27], the wave-functions are approximated by the HF orbitals with relative occupations given by the standard BCS amplitudes. In addition, the pairing has been stabilized using variational formulation avoiding unphysical behavior [28]. For a more extensive explanation of the calculations see [24].

Both Fayans functional have been optimized with respect the same experimental data set (SV-min) [29]. However for Fy(Δr,HFB) has been included the differential charge radii of calcium isotopes. The different parameterization is expected to provide to Fy(Δr,HFB) a better adjustment of the pairing [30].

For this Fayans calcualtions, M.Kortelainen has used an axially symmetric harmonic oscillator basis for solving the HF equations with the modified computer code HFBTHO [31]. The pairing strength parameters have been locally adjusted by scaling all pairing channel EDF parameters to reproduce the odd-even mass staggering for the Pd isotopes on $N = 70$.

Gogny force

The Gogny force is an effective density dependent interaction created on the early seventies by the French physicist Daniel Gogny [32]. The main characteristic was the creation of a finite range interaction where the pairing force derived from the same central potential than the particle-hole (p–h) channel. The Gogny force is composed from four terms:

$$\nu(1,2) = \nu_C(1,2) + \nu_{LS}(1,2) + \nu_{DD}(1,2) + \nu_{Coul}(1,2) \tag{2.12}$$

The central potential (ν_C) was based on Brink-Boeker force [33]. ν_C is a linear combination of two Gaussians containing the terms for spin and isospin channels. The two body spin–orbit interaction (ν_{LS}) is a zero range term taken from the Skyrme functional. The density-dependent term (ν_{DD}) is pure phenomenological and ν_{Coul} is the standard Coulomb potential [34].

The mean field potential is calculated using the HF or Hartree–Fock–Bogoliubov (HFB) approach and the parameterization is perform over 14 adjustable parameters fitted to experimental data. Some examples of parameterization using the Gogny force are D1 [35], D1' [19], D1S [36], D1N [37] and D1M [38]. For this work, the Gogny interaction parameters have been adjusted using the D1S paremeterization.

Gogny mean field calculations have been performed using HFB wave functions with blocking, i.e., breaking the time-reversal symmetry. The HFB energy curves have been explored along the axial quadrupole deformation blocking different K-quantum numbers which are the projection of the angular momentum along the z-axis of the intrinsic reference frame. By minimizing the HFB energy on the blocked wave functions the different states has been identified by their K-quantum number.

In Figure 2.2 the implementation of the method is shown for the ^{105}Pd. In Figure 2.2(a)-(b), the proton and neutron self-consistent single-particle energies are represented as function of the axial quadrupole deformation. As can be observed, the degeneracy of the spherical orbits is broken depending on the value of K-quantum number. This process allows the selection of the relevant single-particle orbits for each deformation, being those, the ones who cross the Fermi energies represented by thick dashed-dotted lines. Subsequently, the HFB equations are solved for each deformation resulting on the HFB energy curves presented at Figure 2.2(c).

This method is restricted to axial calculations. As a result, beyond mean field calculations has been performed in order to include triaxiality.

Beyond mean field calculations allow to deal with large amplitude collective motions combining symmetry restoration and the Generator Coordinate Method (GCM) [39]. The GCM method consist on constructing the many-body wave function as a linear superposition of many-body states described using collective degrees of freedom [40].

On the frame of beyond mean field, Gogny force calculations have been performed for this work within the symmetry-conserving configuration mixing (SCCM) vari-

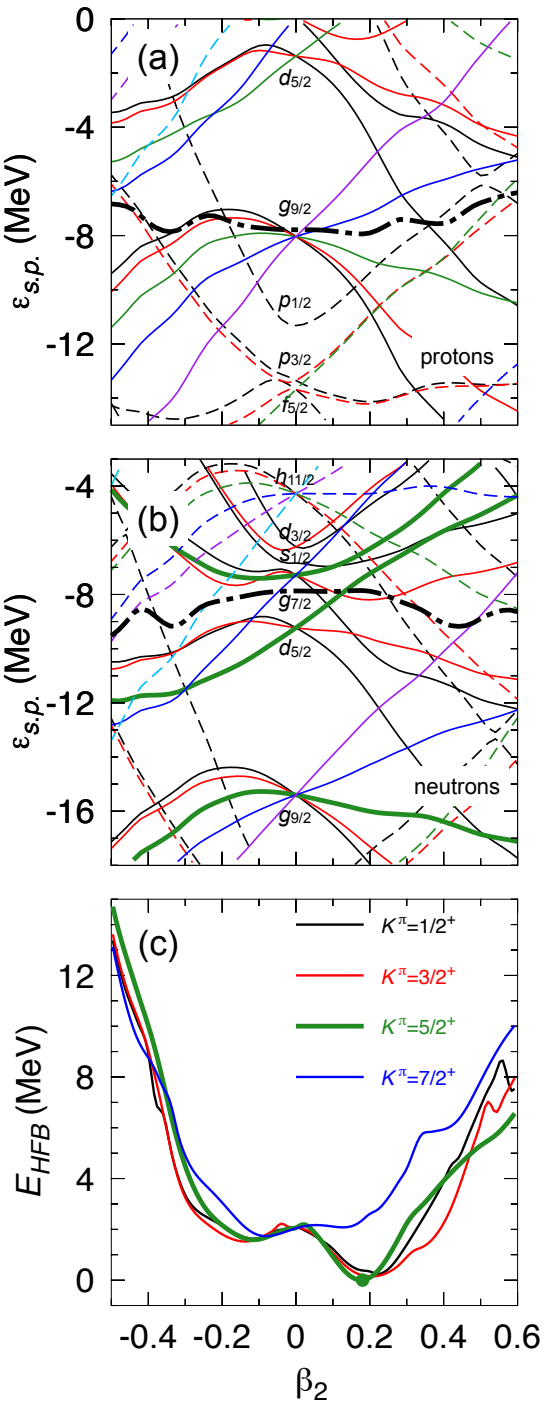

Figure 2.2: *HFB energy curves calculated using Gogny mean field calculations for* ^{105}Pd *with different blocking configurations.*

ational method [41].

On the SCCM method the HFB wave functions are defined along quadrupole (axial and triaxial) shapes. The HFB energy is minimized using the particle number variation after projection (PNVAP) approach with constraints on the quadrupole degrees of freedom. The potential energy surfaces generated give an insight on the collective character of the nucleus. In addition, coefficients of the mixing of the different shapes are found variationally within the generator coordinate method (GCM), restoring the symmetries of the system when projecting particle number and angular momentum of the wave functions. Energy levels, charge radii and electromagnetic properties can be extracted from the expectation values of the corresponding operators on the SCCM nuclear states.

At this point, parity and time-reversal symmetry breaking intrinsic states have not been implemented for the SCCM method. As a consequence, the calculation is limited to even-even nuclei.

2.2 Nuclear ground-state properties

One approach to improve our understanding on the nuclear many body problem is the study of the ground and isomeric states properties. This section will provide an overview of these observables.

2.2.1 Nuclear spin

The nucleons inside the nucleus are arranged in orbitals as has been described on section 2.1.1. This orbitals are characterized by parity $\pi_i = (-1)^{\ell}$ and a total angular momentum j_i, which is the coupling of the orbital angular momentum ℓ_i and a spin angular momentum s_i.

The nuclear spin I is the result of the coupling between the different orbitals. Depending on the nuclear state, The nuclear spin can be calculated in terms of the total angular momentum of the orbitals (jj-coupling) or in terms of the spin and orbital momentum of the nucleus (ls-coupling).

$$LS\ coupling \quad \longrightarrow \quad \hat{\vec{I}} = \hat{\vec{L}} + \hat{\vec{S}} \qquad \hat{\vec{L}} = \sum_i^A \hat{\vec{\ell_i}} \qquad \hat{\vec{S}} = \sum_i^A \hat{\vec{s_i}}$$

$$jj\ coupling \quad \longrightarrow \quad \hat{\vec{I}} = \sum_i^A \hat{\vec{j_i}} \qquad \hat{\vec{j_i}} = \hat{\vec{\ell_i}} + \hat{\vec{s_i}} \tag{2.13}$$

On even-Z and even-N nuclei thanks to the pairing force, all nucleons are coupled pairwise leading to a total spin $I^\pi = 0^+$. For odd-A nuclei, I^π can be calculated as a linear combination of the different orbits. In case that both protons and neutrons numbers are odd, the total spin can be determined by the vector coupling of the unpaired protons and neutrons $|j_\pi - j_\nu| \leq I \leq |j_\pi + j_\nu|$. The ground state nuclear spin will be the candidate which lowest energy and can often be estimated using the Paar's parabola rule [42].

2.2.2 Charge radius

The size of a nucleus is one of its more fundamental properties. Commonly, this radius has been measured as the size of the electromagnetic charge created by the proton and neutron distributions, since the early Rutherford scattering experiment [43]. The charge radii can be defined from the radial moments of the nuclear charge density distribution [44]:

$$\langle r_{ch}^n \rangle = \frac{1}{Ze} \int r^n \rho_{ch}(r, \theta, \phi) dV \tag{2.14}$$

Even if all the radial moments contribute to the charge radii, radial moments higher than $n = 2$ are only accessible by high-precision experimental techniques [45]. Generally, the monopole moment ($\langle r_{ch}^2 \rangle$) is used to characterize the nuclear size. In contrast, the averaged contribution of the higher radial moments is negative and much smaller. In order to simplify text, the 'ch' subscript will be disregarded for the rest of this thesis. The contribution of the radial moments higher than two on the charge radii are shown at Figure 2.3 against the mass number. As can be observed, the contributions escalates with mass, however, the maximmum contribution still being smaller than 8%.

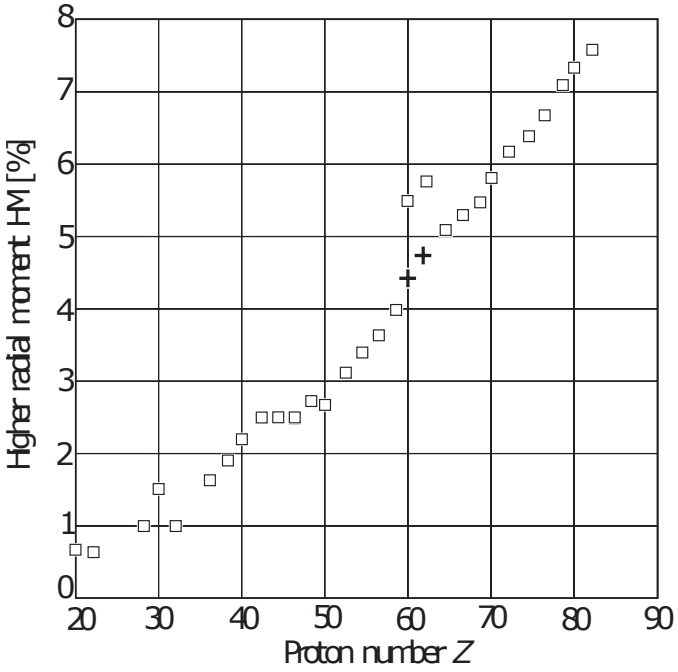

Figure 2.3: *Averaged contribution of higher radial moments HM (in percent), averaged over the different isotopes of one element calculated from elastic electron scattering results. The contribution is negative. [44]*

In experimental measurements, the total contribution of all radial moments can be measured comparing two isotopes through the nuclear parameter $\Lambda^{A,A'}$:

$$\Lambda^{A,A'} = (\delta\langle r^2\rangle^{A,A'} + \frac{C2}{C1}\delta\langle r^4\rangle^{A,A'} + \frac{C3}{C1}\delta\langle r^6\rangle^{A,A'} \ ... \ ) \tag{2.15}$$

Where C_n are the tabulated Seltzer coefficients [46].

2.2.3 Nuclear magnetic dipole moment

When a charged particle has an orbital movement, generates a magnetic moment proportional of its orbital moment.

$$\overrightarrow{\mu} = \frac{e}{2m}\overrightarrow{l} \tag{2.16}$$

The magnitude $\frac{e\hbar}{2m}$ is called nuclear magneton μ_N. Due to the orbital movement of the nucleons, all nuclei with non-zero spin have an observable magnetic moment. The magnetic dipole operator is defined as:

$$\mu = \left(\sum_{i=0}^{Z} g_L^{\pi} L_i + \sum_{i=0}^{Z} g_S^{\pi} S_i + \sum_{i=0}^{N} g_L^{\nu} L_i + \sum_{i=0}^{N} g_S^{\nu} S_i \right) \mu_N \tag{2.17}$$

Where g_L and g_S are the orbital and spin gyromagnetic factors for neutrons and protons.

The magnetic-dipole moment can be obtained as the expectation value of the z-component of the magnetic dipole operator where the spin projection is maximal $I = m$:

$$\mu = \langle I, m = I | \mu | I, m = I \rangle = \left(\frac{I}{I+1} \right)^{\frac{1}{2}} \langle I || \mu || I \rangle \tag{2.18}$$

Where $\langle I||\mu||I\rangle$ is the reduced matrix element from the Wigner-Eckart theorem. For n particles within a particular single-particle orbital j:

$$g = \frac{\mu(j^n, I)}{I} = \frac{\mu(j)}{j}$$

Being g the g-factor. From the last correlation, it can be deduce that the g-factor of a nuclear state with pure configuration should be equal to the g-factor of a single nucleon in that orbit. This single particle g-factors are called the the Schmidt g-factors [47] and by comparison with the experimental g-factor are a sensitive tool to study valence particle occupation and characterize the many-body correlations and collective behavior in the nuclei.

2.2.4 Nuclear electric quadrupole moment

The electric quadrupole moment is the result of the charge distribution inside the nucleus. The electrical quadrupole moment tensor can be defined as:

$$Q_{ij} = e\sum_{l=0}^{Z}(3r_{il}r_{jl} - r_l^2) \tag{2.19}$$

From the expression, the quadrupole moment can be described as an indicator of a charge distribution asymmetricity or non-spherical shape. Alternatively, Equation 2.19 is more often written in terms of spherical tensors:

$$Q_m = e\sqrt{\frac{4\pi}{5}}\sum_l r_l^2 Y_m^2(\theta_l, \phi_l) \tag{2.20}$$

The spectroscopic quadrupole moment is the expectation value of the electric quadrupole operator in the spin aligned state $m = I$:

$$Q_s = \langle I, m = I|Q_2|I, m = I\rangle = \sqrt{\frac{I(2I-1)}{(2I-1)(2I+3)(I+1)}}\langle I||Q_z||I\rangle \tag{2.21}$$

Where $\langle I||Q_z||I\rangle$ is the reduced matrix element from the Wigner-Eckart theorem. Equation 2.21 can be rewritten obtaining the relation between the spectroscopic and the intrinsic quadrupole moments, which is the quadrupole moment on the intrinsic frame.

$$Q_0 = \frac{(2I+3)(I+1)}{3K^2 - I(I+1)}Q_s \tag{2.22}$$

Where K is the spin projection on the nuclear symmetry axis. In case of static deformation the intrinsic quadrupole moment is linked to the deformation parameter.

$$Q_0 = eZ\sqrt{\frac{5}{\pi}}\langle r^2\rangle\langle\beta\rangle\left(1 + \frac{\langle\beta\rangle}{8}\sqrt{\frac{5}{\pi}}\right) \tag{2.23}$$

2.2.5 Nuclear deformation

Nuclear deformation can not be directly extracted from the measurements performed during this thesis. However, information about deformation can be inferred from two of the measured observables (charge radii and quadrupole electric moment).

Nuclear deformation is used to characterize nuclei with non-spherical shape. From a simple liquid drop model point of view, non-spherical nuclear shapes can be expressed in terms of the length of the radius vector pointing from the origin (center of mass) to the surface of the nucleus [48]:

$$R(\theta,\phi) \;=\; R_0(1+\alpha_{00}+\sum_{\lambda=1}^{\infty}\sum_{\mu=-\lambda}^{\lambda}\alpha^*_{\lambda\mu}Y_{\lambda\mu}(\theta,\phi)) \tag{2.24}$$

where R_0 is the spherical radius, α the deformation coefficients and λ and μ are, respectively, the mode and order of the deformation. In this thesis, the discussion will remain on quadrupole deformations ($\lambda = 2$).

For quadrupole deformations, Equation 2.24 will be dependent on five $\alpha^*_{\lambda\mu}$ parameters. By transforming the framewotk to Euler angles, these five parameters are reduced to three variables a_{20}, a_{22} and a_{2-2}, as function of the the axial elongation (β) and the triaxiality parameter (γ):

$$a_{20} \;=\; \beta cos\gamma \qquad\qquad a_{22} \;=\; a_{2-2} \;=\; \frac{1}{\sqrt{2}}\beta sin\gamma \tag{2.25}$$

As a result, nuclear shapes can be expressed on a plane dependent of β and γ as is shown at Figure 2.4. Note that the interval $0 < \gamma < 60$ is enough to illustrate all quadrupole shapes, being $\gamma \neq 0$ triaxial shapes.

The mean-square charge radii can indicate nuclear deformation when its value deviates from the spherical prediction. Assuming a constant density, a spherical nucleus will exhibit the smallest radii between nucleus with equal volume, i.e., an increase on deformation leads on an increase of the mean-square charge radii. The mean-squared charge radius of an axially symmetric deformed nucleus can be parameterized relative to its spherical radii $\langle r^2_{sph}\rangle$ and its quadrupole deformation parameter β.

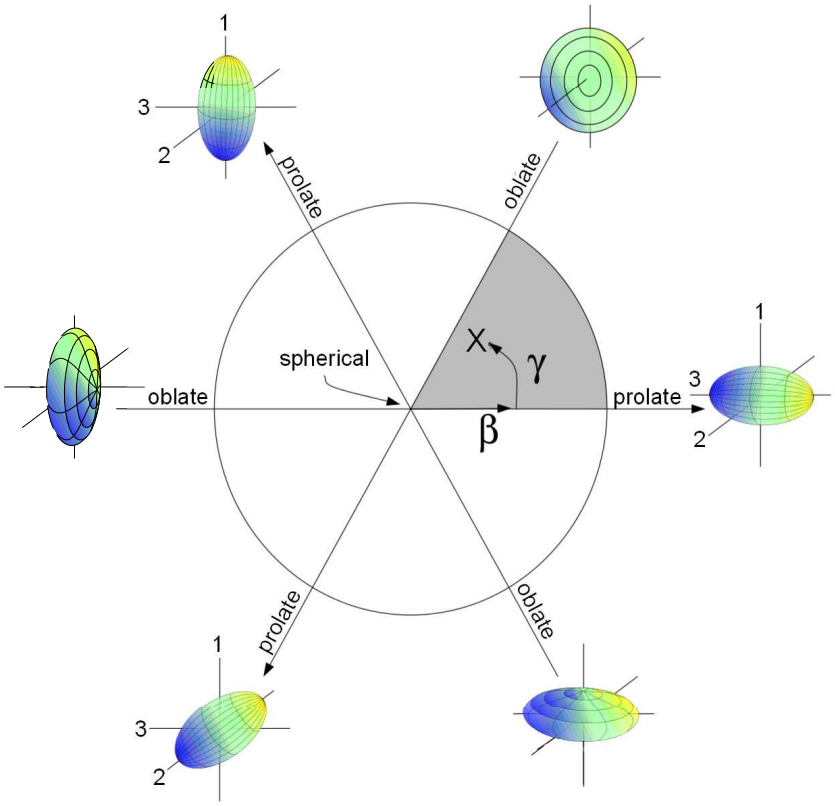

Figure 2.4: *Representation of the nuclear shape evolution in the β, γ plane. β is the axial elongation and γ is the triaxiality parameter. [49]*

$$\langle r^2 \rangle = \langle r^2_{sph} \rangle (1 + \frac{5}{4\pi} \langle \beta^2 \rangle) + 3\sigma^2 \tag{2.26}$$

where σ is a constant representing the nuclear surface diffuseness parameter.

This effect can be observed at the so-called 'kinks' [7]. This 'kinks' are sudden changes in the slope of the charge radius at isotopic chains when crossing magic numbers.

The trends on mean-square charge radii also allows the study of the odd-even staggering (OES), which accounts on the difference on average radius between odd-N and even-N neighbours. The most common case of OES is when the charge radii on even-N isotopes is larger than the average of its odd-N neighbour, this effect has been usually explain as the suppression of pair scattering by the unpaired neutron [50]. As a result, pairing has been consider as the dominant contributor on the odd-even staggering. In contrast, inverted OES, meaning that odd-A isotopes

has an average larger radii, has been linked to octupole deformation [51] or deformation induced by the valence neutron [52]. Leading structure effects become more and more important in the last years [53].

2.3 Region of interest

Palladium with 46 protons is located at the nuclear chart bellow the magical tin. This region has awaken the interest of the field due to its richness of nuclear properties. Specially the surroundings of the double magic ^{100}Sn and the $N = Z$ line, a schematic overview can be observed at Figure 2.5.

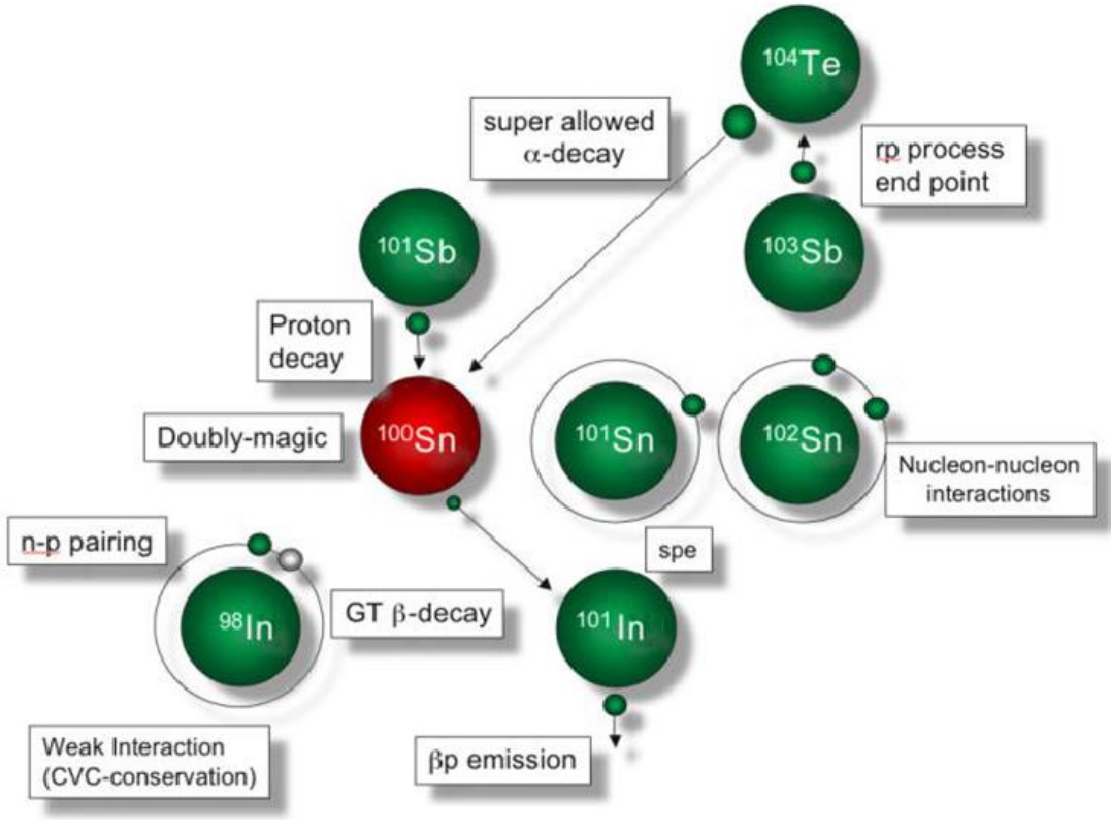

Figure 2.5: *Schematic overview of physical phenomena surrounding ^{100}Sn. Picture from D. Seweryniak.*

The nucleons on the N=Z line provide an unique opportunity to study nucleon-nucleon interactions between protons and neutrons in identical single-particle orbits. The effects of the nucleon-nucleon interaction can be shown on the evolution

of the single particle energies [54] or on the spin-aligned coupling schemes related with the T=0 and T=1 pairing interaction [55], among other phenomena. In addition, this region exhibits interesting decay patterns as the super-allowed beta-decay of ^{100}Sn [56].

From the observables perspective, the mean-square charge radii provides an insight on the deformation across the region. At Figure 2.7 is plotted the differences on mean square charge radii ($\delta\langle r^2\rangle$) for the elements on this region, except palladium. A smooth evolution is observed on the heavier elements of the region. The parabolic behavior is related to quadrupole contributions in a core polarisation model [57]. In contrast, a sudden increase on $\delta\langle r^2\rangle$ is observed on the lighter elements around N=60, being a indication of a shape change.

These two different trends are related to the single particle behavior close to the magic numbers against more collective systems approaching Z=40. Spectroscopic information between the two regions will provide an insight on the transition between the single particle picture and the collective framework. However, optical measurements are hindered by the refractory character of this elements, due to their difficult production at ISOL type facilities.

Another interesting feature which is present at Figure 2.7 are the kinks at the shell closures. When crossing the N=50 shell closure, a large increase on the mean square charge radii has been shown for Ag [58], when compared to lighter systems as Mo [59], Nb [60] or Zr [61].

In order to provide a better understanding of these phenomenons, the mean square charge radii and electromagnetic moments of palladium have been measured on this thesis.

2.3.1 Palladium motivation

A systematic measurement of ground state observables across the palladium isotopic chain will be used to study the transition between the strongly deformed systems around Zr(Z=40, N=60) and the more spherical systems approaching Sn.

Despite the richness on interesting phenomena mentioned above, experimental information concerning the ground-state properties at the palladium neutron deficient region is scarce. A measurement of the mean-square charge radii towards and beyond N=50 will provide good experimental data to test and benchmark theoretical calculations, together to improve the current understanding about the

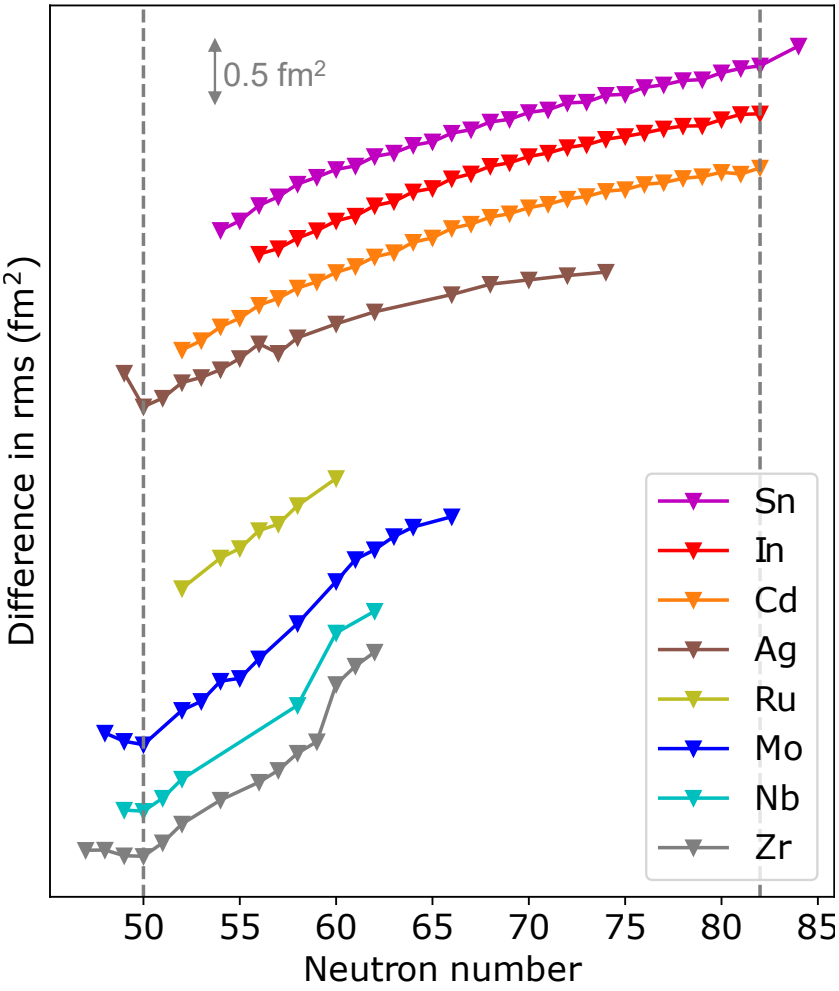

Figure 2.6: *Changes in rms charge radii as a function of neutron number for Sn(Z=50), In(Z=49), Cd(Z=48), Ag(Z=47), Ru(Z=44), Mo(Z=42), Nb(Z=41) and Zr(Z=40). Each element is separated 0.5 fm² for each proton added at N=60. Picture updated from [7].*

magnitude of the "kink".

Regarding deformation, it exists a disagreement on the origin and character of deformation on palladium isotopes on the mass range $110 < A < 118$. On one hand, the decay pattern of $^{110-116}$Pd was found to be compatible with a γ-soft rotor [62]. This interpretation was complemented by a later γ-γ-γ coincidence measurement [63] which expanded the prolate deformation to $^{109-123}$Pd isotopes. Theoretical deformed Skyrme-Hartree-Fock calculations predicted prolate deformation for ground states [64], supporting the experimental measurements. On the

other hand, oblate-driving proton $(g_{9/2})_2$ quasiparticle alignment from the prompt γ ray spectra of ^{112,114,116}Pd suggested an oblate-deformed core [65]. Potential energy surfaces (PESs) calculated using the Triaxial Projected Shell Model (TPSM) approach suggested a γ-soft nature [66].

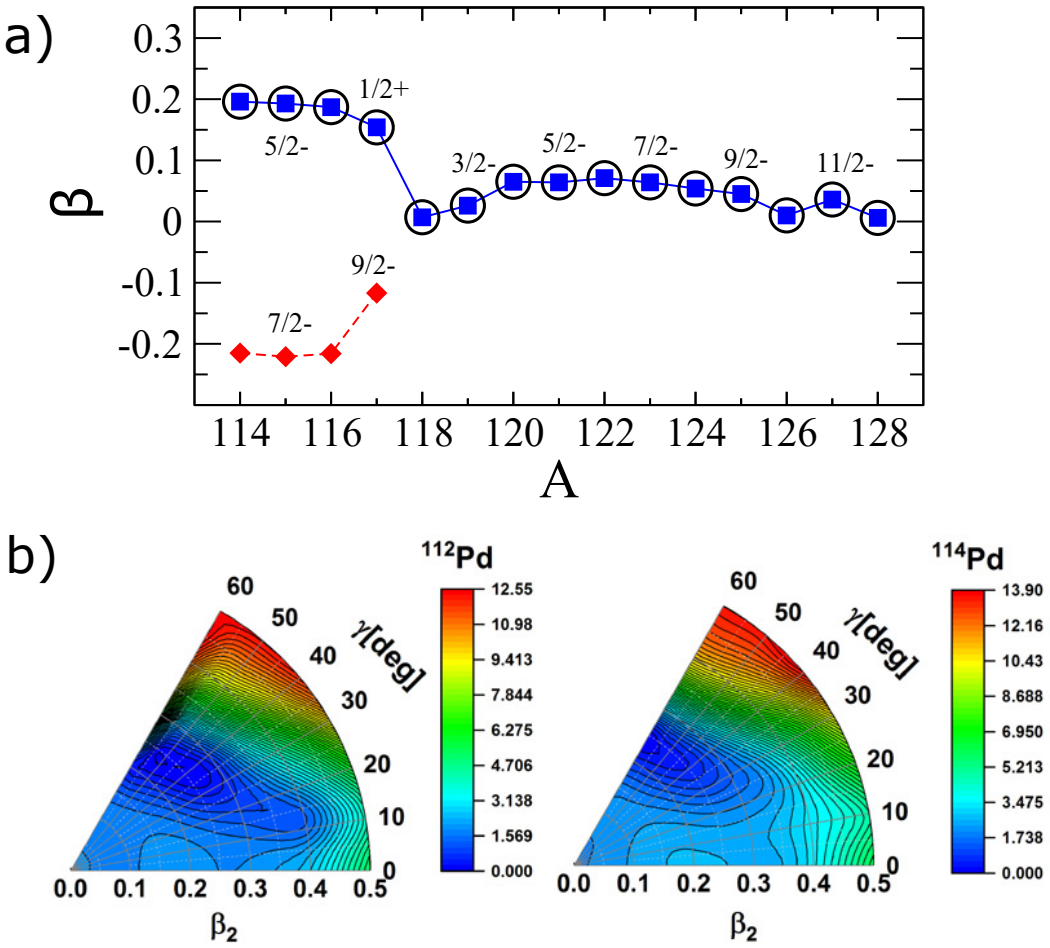

Figure 2.7: *Theoretical calculations of deformation for neutron rich Pd isotopes. a) Isotopic evolution of the quadrupole deformation parameter β [64]. b) Mean filed potential energy surfaces for ^{112,114}Pd isotopes [66]*

Another discussion related with palladium neutron rich isotopes is the discussion related to the spin assignment on ^{115}Pd ground and isomeric states. Two different pairs of spin assignments have been proposed based on the observed E3 γ-transition between the isomeric and ground states [67]. $3/2^+$ and $9/2^-$ spin for the ground (^{115}Pd) and isomeric state (^{115}Pd^m) was proposed by [68] while $1/2^+$ and $7/2^-$ was proclaimed by [69].

Chapter 3

Concepts from Laser spectroscopy

3.1 Atomic structure

The nuclei is surrounded by electrons forming atoms. Assuming a point-like nucleus, the electrons are structured in atomic levels determined by their movement in the Coulomb field generated by the nucleus. An overview on atomic structure is going to be presented at this section, for a more detailed explanation look [70].

The description of an atomic system is given by its Schrödinger equation [71]:

$$i\hbar\frac{\partial\Psi}{\partial t} \;=\; \hat{H}\Psi \tag{3.1}$$

where $\hbar$ is the reduced Planck constant and i is the imaginary unit. Starting with the simplest atom, hydrogen, with only one electron moving in a symmetric potential. Its Hamiltonian can be written as:

$$-\frac{\hbar^2}{2m_1}\Delta_1\psi - \frac{\hbar^2}{2m_2}\Delta_2\psi - \frac{q_2 q_1^2}{4\pi\varepsilon_0 r}\psi \;=\; E\psi(\overrightarrow{r_1},\overrightarrow{r_2}) \tag{3.2}$$

where m_1, $q_1 =^- e$ and $\overrightarrow{r_1}$ are the mass, charge and radius vector of the electron; $m_2 \gg m_1$, $q_2 =^+ Ze$ and $\overrightarrow{r_2}$ are the mass, charge and radius vector of the nucleus; Δ_i is the Laplace operator with respect to $\overrightarrow{r_i}$ and $\psi(\overrightarrow{r_1},\overrightarrow{r_2})$ the wave function. The first term and second term describe the kinetic energy of the electron and nucleus

and the third term the potential energy of the Coulomb interaction between the two particles depending on the distance $r = |r_1 - r_2|$.

In case of multielectronic systems, an additional term needs to be added on Equation 3.2 in order to take into account interelectronic repulsions between pairs of electrons.

$$\hat{H_{rep}} = \sum_{i=1}^{N} \sum_{j>i}^{N} \frac{e^2}{|\overrightarrow{r_i} - \overrightarrow{r_j}|} \tag{3.3}$$

The Hamiltonian can be rewritten into a term (H_{CM}) describing the center of mass, and a second term (H_r) describing the position r of a particle with reduced mass μ relative to that of the nucleus at $r = 0$ in a coulomb filed with potential energy E_{pot}. As the Coulomb potential is spherical, the wave function can be rewritten as the combination of a radial function $R(r)$ and spherical functions Y_l^m (angular dependence).

$$\psi(r, \vartheta, \varphi) = R(r) Y_l^m(\vartheta, \varphi) \tag{3.4}$$

On this configuration, the radial electron distribution will depend on the discrete eigenvalues E_n:

$$E_n = -\frac{\mu Z^2 e^4}{8\varepsilon_0^2 h^2 \cdot n^2} = -Ry\frac{Z^2}{n^2} \qquad Ry = \frac{\mu e^4}{8\varepsilon_0^2 h^2} \tag{3.5}$$

The energy E_n of an atomic state depends in this model solely on n, the principal quantum number. In this approximation, the atomic states energetically-degenerate on different states which are possible combinations of l and m (projection of the angular momentum $\overrightarrow{l}$ onto the quantization axis with $2l + 1$ possible values) for the same n and same energy [70].

In order to reproduce the electronic level structure, relativistic contributions have to be taken into account. The first one is a shift on the energy generated by a small decrease on the electron's kinetic energy, due to its mass in the Coulomb field, which makes the total energy of an eigen-state dependent to l [72].

$$\Delta E_r = -E_{nr}\frac{Z^2\alpha^2}{n}\left(\frac{3}{4n} - \frac{1}{l + 1/2}\right) \qquad \alpha = \frac{e}{4\pi\varepsilon_0\hbar c} = \frac{1}{137} \tag{3.6}$$

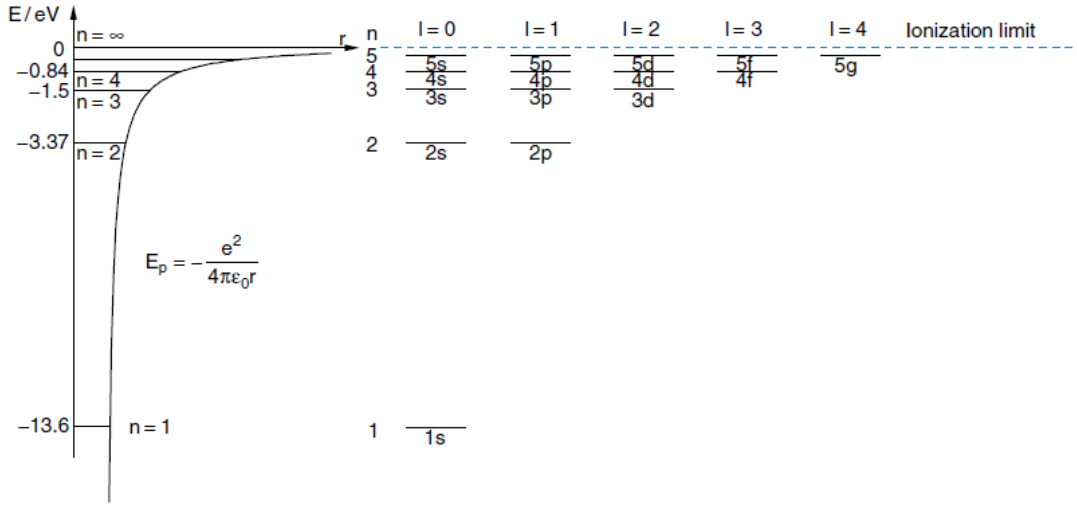

Figure 3.1: *Level scheme of the H atom, drawn on a correct scale according the Schrödinger equation.*

The second correction is related to the treatment of the electron as a point charge particle. The quantum mechanical expectation value, obtained with the hydrogen wavefunction ψ gives the Darwin term [73]:

$$W_D \;=\; \frac{Ze^2\hbar}{\varepsilon_0 m_e^2 c^2}|\psi(0)|^2 \;=\; 4Z^4 m_e c^2 \alpha^4 \tag{3.7}$$

The third relativistic contribution is the interaction between the orbital magnetic moment and the spin moment of the electron ($s_e = \pm\frac{1}{2}\hbar$) [74]. The spin-orbit coupling split the energy levels E_n into the fine structure components which energies can be calculated as:

$$E_{n,l,s} \;=\; E_n - \mu_s \cdot B_l \;=\; E_n + \frac{\mu_0 Ze^2}{8\pi m_e^2 r^3}(s \cdot l) \tag{3.8}$$

This equation can be simplified introducing the total angular momentum as a vector sum of orbital angular momentum l and electron spin s ($j = l + s$, $j^2 = l^2 + s^2 - 2l \cdot s$).

$$E_{n,l,s} \;=\; E_n + \frac{a}{2}[j(j+1) - l(l+1) - s(s+1)] \qquad a \;=\; \frac{\mu_0 Ze^2\hbar}{8\pi m_e^2 r^3} \tag{3.9}$$

Inside the Coulomb field with $E \propto 1/r$ the energy of a fine structure component does not depend on the quantum number l. Therefore, the fine structure can be calculated as:

$$E_{n,j} = E_n[1 + \frac{Z^2\alpha^2}{n}\left(\frac{1}{j+\frac{1}{2}} - \frac{3}{4n}\right)] \tag{3.10}$$

3.2 Atomic-nuclear interaction

The electronic fine structure reproduce the atomic energy levels, however do not take account the effect of the finite size (no-point size) of the nucleus. The finite size entails shifts on the electronic levels and the interaction between the nuclear electromagnetic field and the electron cloud. The first consequence is related with the isotope shift and the second leads to an additional splitting of the atomic levels, called hyperfine splitting.

By studying these effects of the atom-nucleus interaction, the nuclear properties can be extracted in a nuclear-model independent way, as will be shown at this section.

3.2.1 Isotope shift

Considering a given transition on the atomic fine structure, is called isotope shift to the difference on the transition energy between isotopes of the same element with mass A and A'. In laser spectroscopy, this property is observed as a shift on the transition frequency (or centroid of the hyperfine structure) between two isotopes.

$$IS^{A,A'} = \nu^A - \nu^{A'} \tag{3.11}$$

This effect is created by the difference in mass, size and shape between isotopes due to their different number of neutrons. Thereby, the isotope shift can be separated into two main contributions, the mass shift arising from the change in total mass of the system and the field shift which arise from the change in the spatial distribution of the nuclear charge [75].

$$\delta\nu^{A,A'} = \delta\nu_{MS}^{A,A'} + \delta\nu_{FS}^{A,A'} \tag{3.12}$$

Mass shift

The mass shift can be explained as the effect of the change on the reduced mass of the electron in the electron-nucleus system.

$$\delta\nu_{MS}^{A,A'} = M\frac{m_{A'} - m_A}{m_{A'}m_A} \tag{3.13}$$

being M the mass shift factor. The energy of the fine structure levels change as an effect of the recoil motion of the nucleus and can be calculated using the relativistic nuclear recoil operator [76]:

$$R_{i,j} = \frac{\overrightarrow{p_i} \cdot \overrightarrow{p_j}}{2M} - \frac{Z\alpha}{2Mr_i}(\overrightarrow{\alpha_i} + \frac{(\overrightarrow{\alpha_i} \cdot \overrightarrow{r_i})\overrightarrow{r_i}}{r_i^2}) \cdot \overrightarrow{p_j} \tag{3.14}$$

For two electrons i and j, where M is the nuclear mass, Z the nuclear charge, p the kinetic moment of the electrons, r is the relative position of the electrons respect of the nucleus, α the fine-structure constant and $\overrightarrow{\alpha}$ is the Dirac (4x4) matrix.

The mass shift can be separated into two different terms. The normal mass shift ($\sum_i R_{ii}$) which is the nuclear recoil against an individual electron momenta and the specific mass shift ($\sum_{i\neq j} R_{ij}$) which is the nuclear recoil against the correlated electron motion.

The normal mass shift has always a positive value which can be calculated accurately from the transition frequency $M_{NMS} = \nu(\frac{m_e}{m_u})$, where m_e and m_u are the mass of the electron and nucleon, respectively. On contrast, the specific mass shift can take both positive and negative values, and is challenging to calculate, increasing the difficulty as increasing the proton number. However the specific mass shift can be experimentally obtained by combining optical data with muonic or K X-ray measurements.

As the mass shift is uniquely related with the mass of the nucleus does not gives any new information about the nuclear observables.

Field shift

The field shift accounts for the different charge distribution between two isotopes. The electrons can only experience a different potential when they reside inside the nucleus with a probability $|\Psi_e(0)|^2$. Therefore, is called field shift to the perturbation of binding energy that results from the spatial overlap of the electron wave function, $\psi_e(r)$, and the nuclear volume.

Assuming the electron wave function constant across the nuclear volume, the field shift can be formulated as:

$$\delta\nu_{FS}^{A,A'} = \frac{Ze^2}{6\hbar\epsilon_0}\Delta \mid \psi_e(0) \mid^2 \delta\langle r^2\rangle^{A,A'} = F\lambda^{2A,A'} \tag{3.15}$$

where, $\hbar$ is the Planck's constant, ϵ_0 is the electric constant, $\Delta \mid \psi_e(0) \mid^2$ is the change in electron density inside the nucleus between the two atomic levels involved on the transition and $\lambda^{A,A'}$ is the nuclear parameter introduced at subsection 2.2.2.

The nuclear parameter $\lambda^{A,A'}$ take into account all moments on the charge radii. Commonly this parameter is approximated to the root mean-square (rms) charge radii, however, the contribution higher order terms grows with the mass (see Figure 2.3). Taken all considerations into account, the field shift can be correlated with the rms charge radii by the following equation:

$$\delta\nu_{FS}^{A,A'} = F\lambda^{A,A'} = F(\delta\langle r^2\rangle^{A,A'} + \sum_{n=1}^{\infty} C_n \delta\langle r^{2n+2}\rangle^{A,A'}) \tag{3.16}$$

where C_n are the Seltzer coefficients [77].

From the field shift can be extracted information about the mean square charge radii in a model independent way. The sensitivity of this observable changes with the mass number in a way that can be approximated to $\propto \frac{Z^2}{\sqrt[3]{A}}$. In addition, lower valence orbitals, exhibit larger field shifts. In general, in heaver isotopes the field shift is orders of magnitude larger than the mass shift, however in lighter nuclei the mass shift is dominant, as can be shown at Figure 3.2.

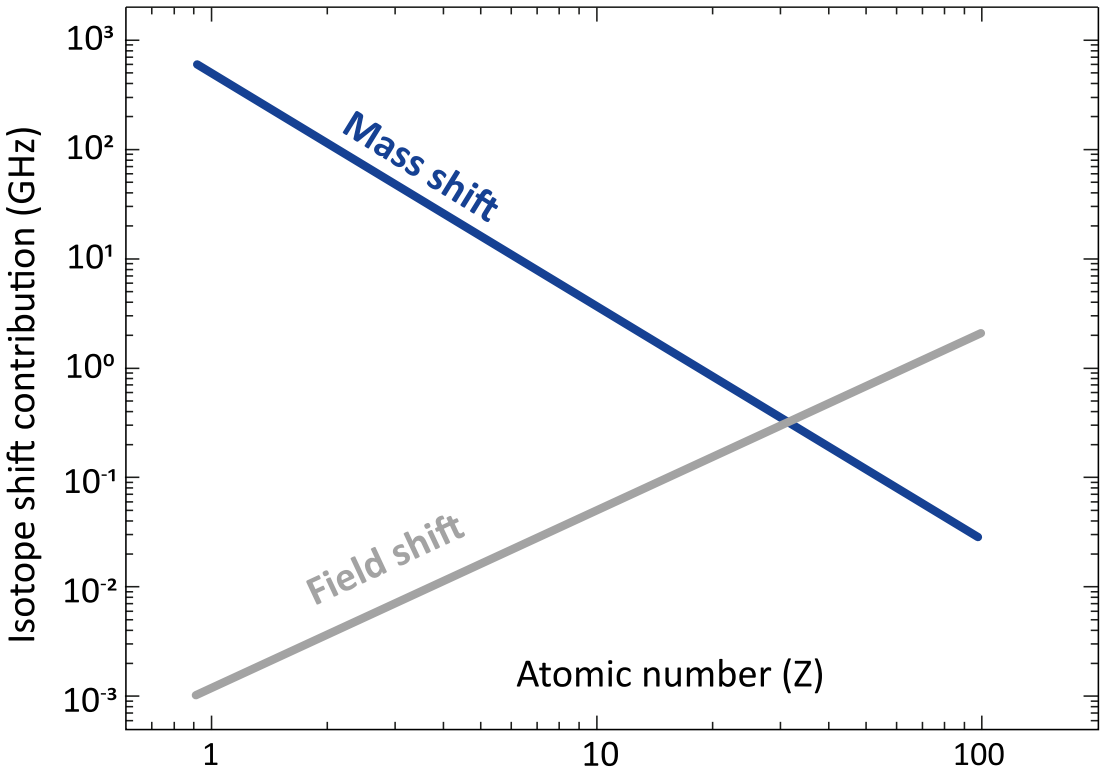

Figure 3.2: *Mass and field shift contribution as a function of the atomic number Z without taking into account relativistic effects. [78]*

King plot method

As mention above, the isotope shift is the combination of the mass and field shift. The expression of the isotope shift for a transition i is obtained combining Equation 3.13 and Equation 3.16.

$$\delta\nu_i^{A,A'} = M_i \frac{m_{A'} - m_A}{m_{A'} m_A} + F_i \delta\langle r^2 \rangle^{A,A'} \tag{3.17}$$

The mass and field factors are only transition-dependent, therefore, independent of the nuclear properties. Can be obtained empirically via the King plot technique, where the M and F are the mass and field factors, respectively.

The technique consist on removing the mass-dependence of the isotope shift equation using the reduced mass $\mu^{A,A'}$, which is sometimes called $\kappa^{A,A'}$.

$$\mu^{A,A'}\delta\nu_i^{A,A'} = M_i + F_i\mu^{A,A'}\delta\langle r^2\rangle^{A,A'} \qquad \mu^{A,A'} = \kappa^{A,A'} = \frac{m_{A'}m_A}{m_{A'} - m_A} \tag{3.18}$$

Knowing the change in the mean-square charge radii of few isotopes and measuring their isotope shifts, it is possible to obtain the mass and field factors of a selected transition by fitting Equation 3.18 with a linear regression (Figure 3.3).

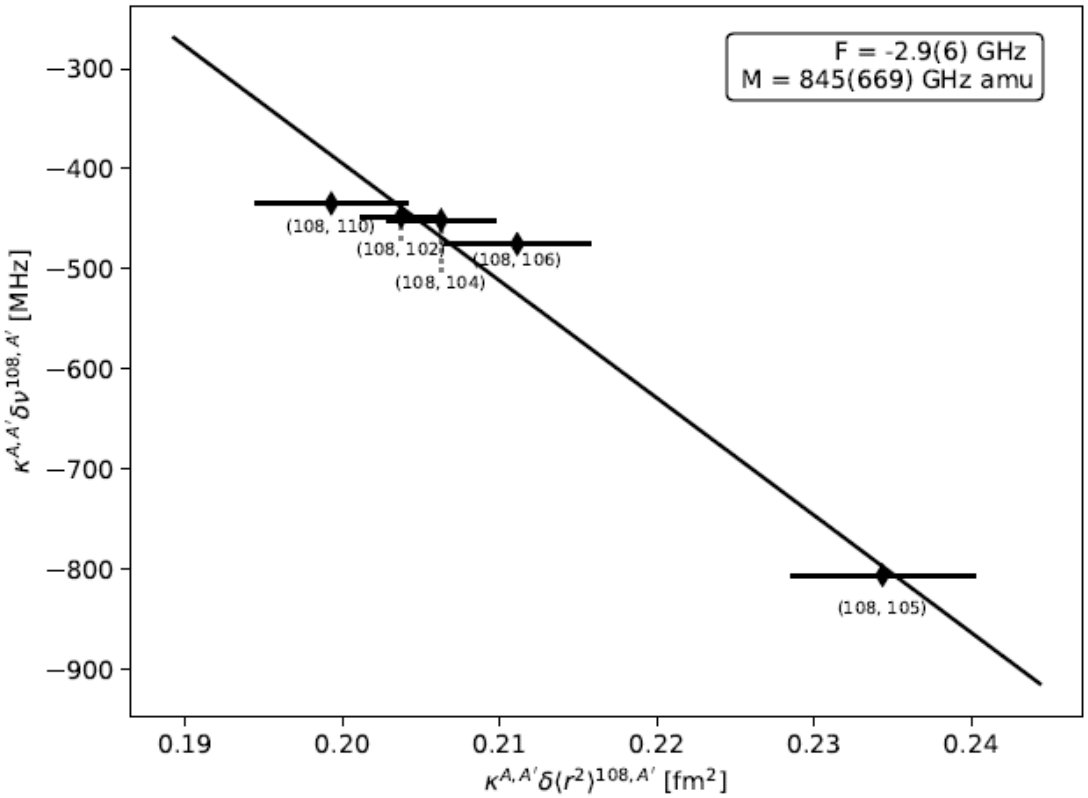

Figure 3.3: *Example of a King plot for Pd isotopes using known rms charge radii of all stable isotopes [44] and measured isotope shifts with respect to the reference isotope $A = 108$. Statistical error bars on the isotope shifts are within the data points [79].*

3.2.2 Hyperfine Splitting

The calculation of the fine structure energy levels does not take into account the coupling of the electrons with the electromagnetic field of the nucleus. The

coupling of the static multipole interaction with the nuclear moments and the fields generated by the electrons leads to small shifts and splittings on the atomic fine level structure. Is called hyperfine structure because this perturbations are in the order of μeV compared to meV in the fine structure levels.

The coupling between the nuclear spin I and the atomic spin J establish a new quantum number F (total angular momentum). The coupling of both spins gives rise to a range of F values between $|I - J| \leq F \leq |I + J|$. The energy of the F hyperfine levels can be calculated using the Hamiltonian. The Hamiltonian can be decomposed in different orders corresponding to the nuclear electromagnetic moments. Only the moments with even parity (odd-order magnetic moments and the even-order electric moments) will have non-zero contribution to the hyperfine energies.

$$H = H_{E0} + H_{M1} + H_{E2} + H_{M3} + \ ... \ , \qquad E_{IJF} = \langle I, J, F|H|I, J, F\rangle \quad (3.19)$$

With each order in the expansion, the complexity of the Hamiltonian increases and have progressively smaller effects. The higher order which has been measured is the magnetic octupole moment [80, 81], however, only the nuclear magnetic dipole and electric quadrupole moments will be studied within this thesis.

Magnetic dipole moment

The interaction between the nuclear magnetic moment and the magnetic field produced by the electrons ($E = \overrightarrow{\mu}_I \cdot \overrightarrow{B}_e$) can be formulated as:

$$H_{hfs}^{M1} = -\int_V B d\mu = -\frac{\mu B_0}{\hbar^2 IJ} I \cdot J \quad (3.20)$$

The integral have been resolved assuming that the magnetic field is constant over the nuclear volume. The resulting Hamiltonian is composed by atomic constants which can be put together in a hyperfine dipole parameter $A = \frac{\mu B_0}{\hbar^2 IJ}$. Therefore, the energy splitting of the hyperfine structure due to the magnetic dipole moment can be written as:

$$\Delta E_{M1} = \frac{1}{2}\frac{\mu B_0}{\hbar^2 IJ}[F(F+1) - I(I+1) - J(J+1)] = \frac{1}{2}AK \quad (3.21)$$

Where K accounts for the coupling of the nuclear and atomic spins ($I \cdot J = K = F(F+1) - I(I+1) - J(J+1)$).

Electric quadrupole moment

The nuclear electric quadrupole moment is an observable that describes the charge distribution throughout the nuclear volume. It contributes to the perturbation of the hyperfine F-states, due to its interaction with the electric field gradient generated by the electrons. The energy splitting induced by the electric quadrupole moment can be written as:

$$\Delta E_{E2} = eQ_s\langle\frac{\partial^2 V_e}{\partial z^2}\rangle\frac{3K(K+1) - 4I(I+1)J(J+1)}{8I(2I-1)(2J-1)} = B\frac{3K(K+1) - 4I(I+1)J(J+1)}{8I(2I-1)(2J-1)} \quad (3.22)$$

Introducing the hyperfine parameter $B = eQ_s\langle\frac{\partial^2 V_e}{\partial z^2}\rangle$, where $_s$ is the spectroscopic quadrupole moment, introduced at subsection 2.2.4.

3.2.3 Energy splitting

Combining Equation 3.21 and Equation 3.22, the total energy splitting results:

$$\frac{\Delta E}{\hbar} = \frac{K}{2}A + \frac{3K(K+1) - 4I(I+1)J(J+1)}{8I(2I-1)(2J-1)}B \quad (3.23)$$

In the optical measurements, the transitions between two HFS states at different fine structure levels are measured, obtaining the positions of the resonances (γ) relative to the centroid (ν). Figure 3.4 shows the hyperfine spectrum of resonant transitions between two atomic levels.

$$\gamma = \nu + \frac{\Delta E^u - \Delta E^l}{\hbar} \quad (3.24)$$

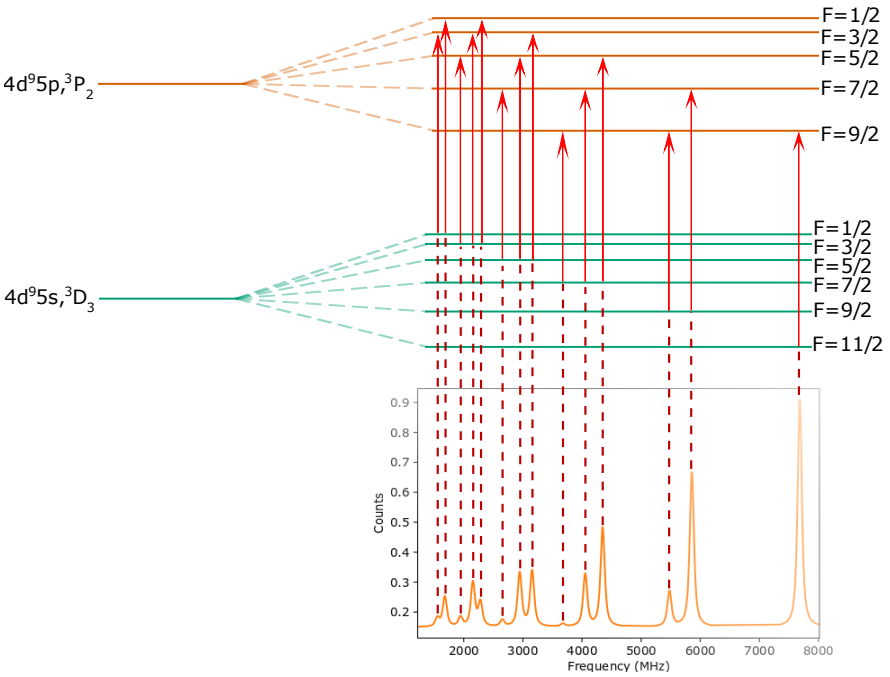

Figure 3.4: *Calculated optical spectrum of the ^{101}Pd ground state ($I = 5/2$) and corresponding level scheme. Each peak corresponds to a transition between hyperfine components of the lower and upper J-states involved in the selected atomic transition.*

The transtition intensities between to hyperfine states F and F' can be calculated using the Wigner 6J-symbol, these relative intensities are colloquially referred to as the Racah intensity.

$$I(F, F') = (2F + 1)(2F' + 1) \begin{Bmatrix} F' & J' & I \\ J & F & 1 \end{Bmatrix}^2 \tag{3.25}$$

3.2.4 Hyperfine anomaly

Is called hyperfine anomaly to the modification of the value of the hyperfine parameter A for electron wave functions which have non-zero probability of residing in the nucleus.

The correction is generated by two effects. The first effect leads to the extended nuclear magnetization across the nuclear volume, the Bohr-Weisskopf effect [82].

And the second is the modification of the electron wavefunctions by the extended nuclear charge distribution, the "Breit–Rosenthal–Crawford– Schawlow" correction [83, 84].

$$A = A_{point}(1+\epsilon_{BW})(1+\epsilon_{BR}) \tag{3.26}$$

Due to the difficulty of calculate A_{point} with sufficient precision for ordinary atoms, the hyperfine anomaly is usually determined from the ratio between two isotopes.

$$\frac{A_1}{A_2} = \frac{g_I(1)}{g_I(2)}\frac{(1+\epsilon_{BW}(1))(1+\epsilon_{BR}(1))}{(1+\epsilon_{BW}(2))(1+\epsilon_{BR}(2))} \tag{3.27}$$

where $g_I = \frac{\mu}{I}$ are the g-factors of the corresponding nucleus.

These corrections (ϵ) are usually in the order of 10^{-3} times the hyperfine parameter A. In addition, the "Breit–Rosenthal–Crawford– Schawlow" (ϵ_{BR}) is in most of nuclei much smaller than the Bohr-Weisskopf effect (ϵ_{BW}). For these reasons, Equation 3.27 is normally approximated to:

$$\frac{A_1}{A_2} \approx \frac{g_I(1)}{g_I(2)}(1+\Delta) \tag{3.28}$$

where Δ is the differential hyperfine structure anomaly parameter [85].

3.3 Laser optics

In laser spectroscopy, the production of laser beams with accurate wavelength are fundamental to measure hyperfine transitions. This section provide a brief overview of some of the basic ideas in stimulated photon emission and wavelength selection.

3.3.1 Emission and Absorption of Electromagnetic Radiation

In an atomic system, energetic transitions between different levels will involve photon emission or absorption. The photon energy will be determined by the difference in energy between the two states i and j.

$$E_{ph} \;=\; h\nu \;=\; h\frac{c}{\lambda} \;=\; E_i - E_j \tag{3.29}$$

In atomic multi-level system, different states interact via photon-electron interaction, emitting and absorbing coherent radiation. Albert Einstein created a model with describes these systems based on the rate equations and the population distribution of the atomic levels [86]. This model uses the Einstein coefficients to calculate the photon emission and absorption probabilities as function of laser frequency, these coefficients are [70]:

1. Spontaneous decay (coefficient denoted with A).
2. Excitation (coefficient denoted with B).
3. Stimulated emission (also denoted with B).

The first process is independent of the presence of an external radiation field. The spontaneous decay represents the probability per second of spontaneous emission of a photon into an arbitrary direction. Due to its relation with the lifetime of the state, the A Einstein coefficient can also be used to calculate the natural linewidth Γ of the transition via the Heisenberg uncertainty relation.

$$\frac{dP_{ji}^{sp}}{dt} \;=\; A_{ji} \qquad\qquad \Gamma \;=\; \frac{\Delta E_{ji}}{h} \;=\; \frac{1}{2\pi\Delta t} \;=\; \frac{A_{ji}}{2\pi} \tag{3.30}$$

In the presence of a radiation field, the atom can absorb a photon, which brings it back into the higher energy state. In this conditions, the probability per second for an absorbing transition is:

$$\frac{dP_{ij}^{abs}}{dt} \;=\; B_{ij}\rho(\nu) \tag{3.31}$$

where B_{ij} is the Einstein coefficient for absorption and $\rho(\nu)$ is the spectral energy density of the radiation field. The radiation field can also induce an atom to emit a photon into a specific wavelength (stimulated emission). Due to time reversal symmetry, the coefficient for stimulated emission has to be equal to the coefficient for absorption $B_{ij} = B_{ji}$.

B_{ij} can be rewritten in terms of interaction cross section $\sigma(\nu)$ and incoming energy density I (W/m^2).

$$\sigma(\nu) = \frac{B_{ij}\rho(\nu)h\nu}{I} \tag{3.32}$$

In addition, the interaction cross section can be linked to the A Einstein coefficient from the optical Bloch equations [87]:

$$\sigma(\nu) = \frac{A_{ij}c^2}{8\pi\nu_0^2}\mathcal{L}(\nu) \tag{3.33}$$

where $\mathcal{L}(\nu)$ is the line shape as function of frequency, which typically (without consider broadening mechanism) is considered as a Lorentzian profile with the natural linewidth Γ and centered at ν_0.

$$\mathcal{L}(\nu) = \frac{1}{\pi}\frac{\Gamma/2}{(\nu-\nu_0)^2+(\Gamma/2)^2} \tag{3.34}$$

Combining Equation 3.32 and Equation 3.34, the expression for B Einstein coefficient results:

$$B_{ij}\rho(\nu) = \frac{A_{ij}Ic^2}{8\pi\nu_0^2 h\nu}\mathcal{L}(\nu) \tag{3.35}$$

Using this coefficients, the time dynamics can be calculated for a generic atomic system with N state population. For instance, for a three level atomic system, the differential equations are written as:

$$\frac{dN}{dt} = \frac{d\begin{bmatrix}N_f\\N_j\\N_i\end{bmatrix}}{dt} = A\cdot N + B_{ij}\rho(\nu)\cdot N \tag{3.36}$$

with

$$A = \begin{bmatrix} -(A_{fi}+A_{fj}) & 0 & 0 \\ A_{fj} & -A_{ji} & 0 \\ A_{fi} & A_{ji} & 0 \end{bmatrix} \quad B = \begin{bmatrix} -(B_{fi}+B_{fj}) & B_{jf} & B_{if} \\ B_{fj} & -(B_{ji}+B_{jf}) & B_{ij} \\ B_{fi} & B_{ji} & -(B_{if}+B_{ij}) \end{bmatrix} \tag{3.37}$$

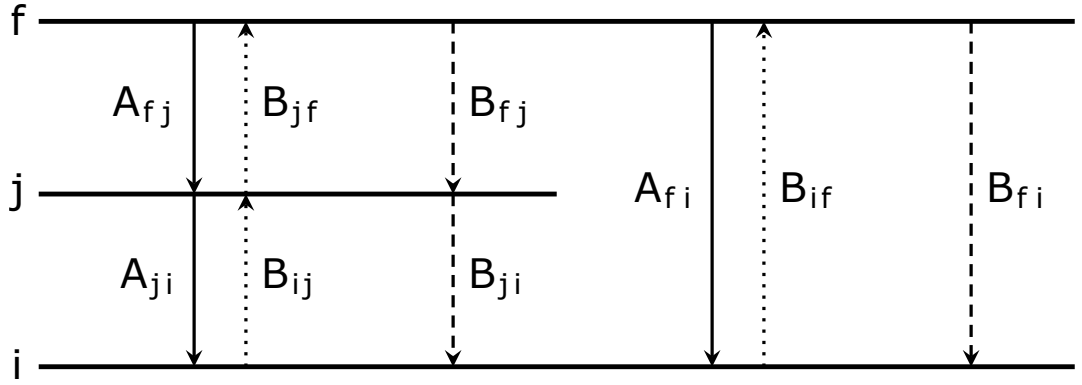

Figure 3.5: *Generic three level system with levels i, j and f. The spontaneous decay (solid), excitation (dotted) and stimulated emission (dashed) paths are indicated [88].*

3.3.2 Physical principles of Lasers

The definition of laser is given by its name which is an acronym for Light Amplification by Stimulated Emission of Radiation. Laser systems are generally composed by three components [70]:

1. The active medium where population inversion occurs.
2. The energy pump which provides the power for the population inversion.
3. The optical resonator which restricts the fluorescence emission to few cavity modes.

The objective of a laser is to favor induced emission over spontaneous emission by reflecting the light back and forth through the active medium. The medium will have a frequency-dependent absorption of the photons which will affect the

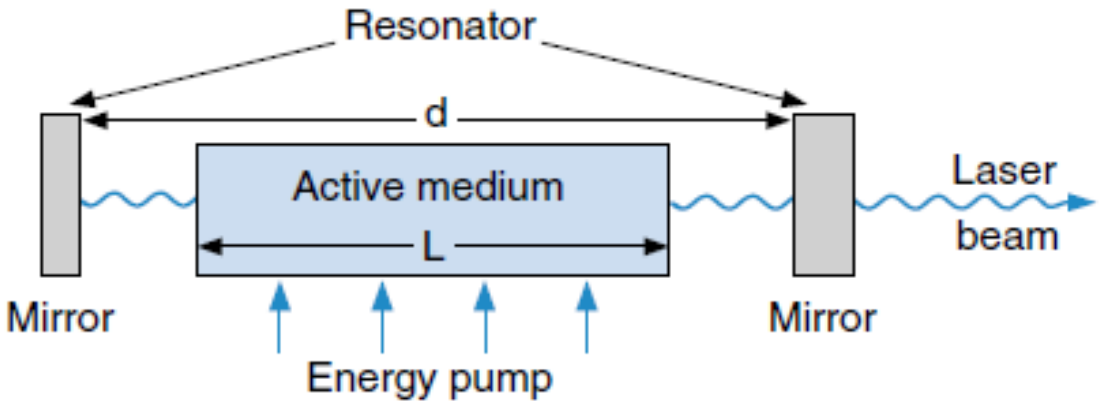

Figure 3.6: *Schematic representation of the laser principle [70].*

population N of its atomic states. The frequency-dependent absorption coefficient $\alpha(\nu)$ between two states i and k can be calculated using the following equation.

$$\alpha(\nu) \;=\; [N_k - \frac{g_k}{g_i} N_i]\sigma(\nu) \tag{3.38}$$

where $\sigma(\nu)$ is the absorption cross section of the transition $N_k \longrightarrow N_i$ and g_i and g_k are the statistical weights of the states $g = 2J + 1$.

In this conditions the population distribution $N(E)$ deviates strongly from a thermal Boltzmann distribution, achieving population inversion when $N_i > (\frac{g_i}{g_k})N_k$. In a laser this process is self-sustained when the threshold condition $2\alpha(\nu)L + \gamma < 0$ is fulfilled, being γ the loses on the active medium. The common loses are due to reflection, diffraction and absorption and scattering.

A typical active medium used in laser spectroscopy is a Ti:sapphire (Ti:sa) which is a Ti^{3+} doped Al_2O_3 sapphire crystal. This is a four-level laser medium with a maximum cross-section for absorption around 500 nm and an emission band from 670 to 1100 nm.

The frequency spectra of the induced emission is distributed over the resonances or modes of the cavity. Inside a laser cavity with length $L \gg \lambda$, The radiation field can be described as a superposition of waves with wave vectors $k = \{k_x, k_y, k_z\}$. In order to have a stationary field on the cavity, the values for the components of the k-vector are restricted to several modes dependent on the cavity length.

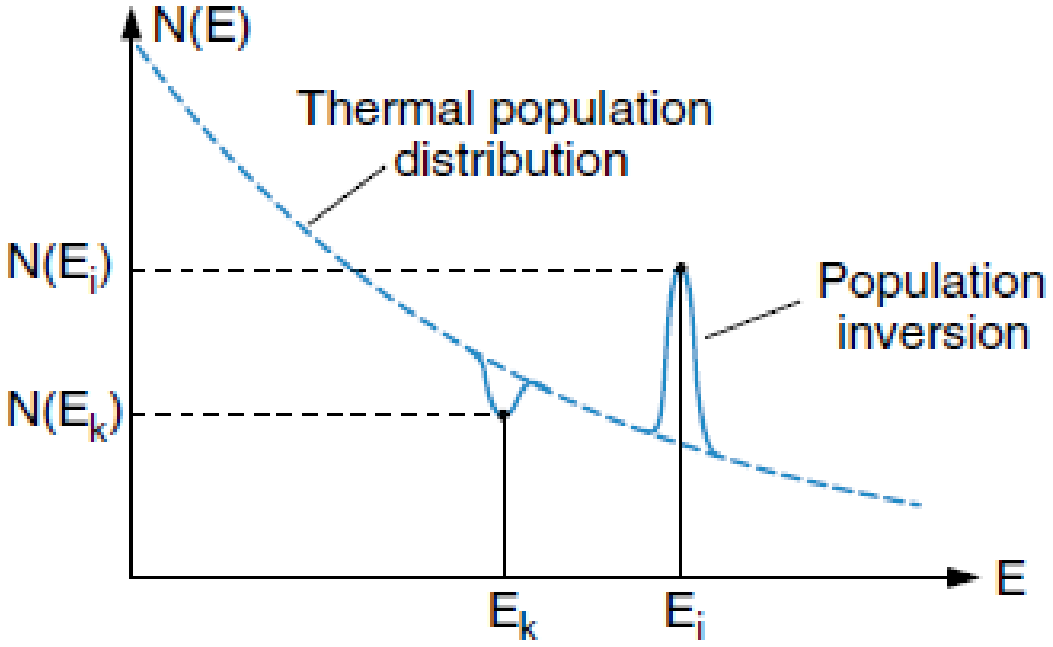

Figure 3.7: *Selective population inversion* ($N_i > N_k$) *in spite of* $E_i > E_k$*, deviating from a thermal population distribution [70].*

$$k_x = \frac{\pi}{L} n_1 \quad k_y = \frac{\pi}{L} n_2 \quad k_z = \frac{\pi}{L} n_3 \rightarrow k = |k| = \frac{\pi}{L}\sqrt{n_1^2 + n_2^2 + n_3^2} \quad (3.39)$$

where the n_i are arbitrary integers. Therefore, only the wavelengths $\lambda = 2\frac{\pi}{k}$ will compose the emission spectra, these wavelengths are called cavity or resonator modes.

3.3.3 Wavelength selection elements

For efficient excitation of atomic transitions the laser needs to operate at resonant frequency with a linewidth similar to the one from the transition. For this purpose, frequency tuning is achieved by the insertion of frequency selective optical elements into the optical resonator. This elements perform wavelength selection by the introduction of wavelength dependent losses. One example of this kind of elements is the etalon.

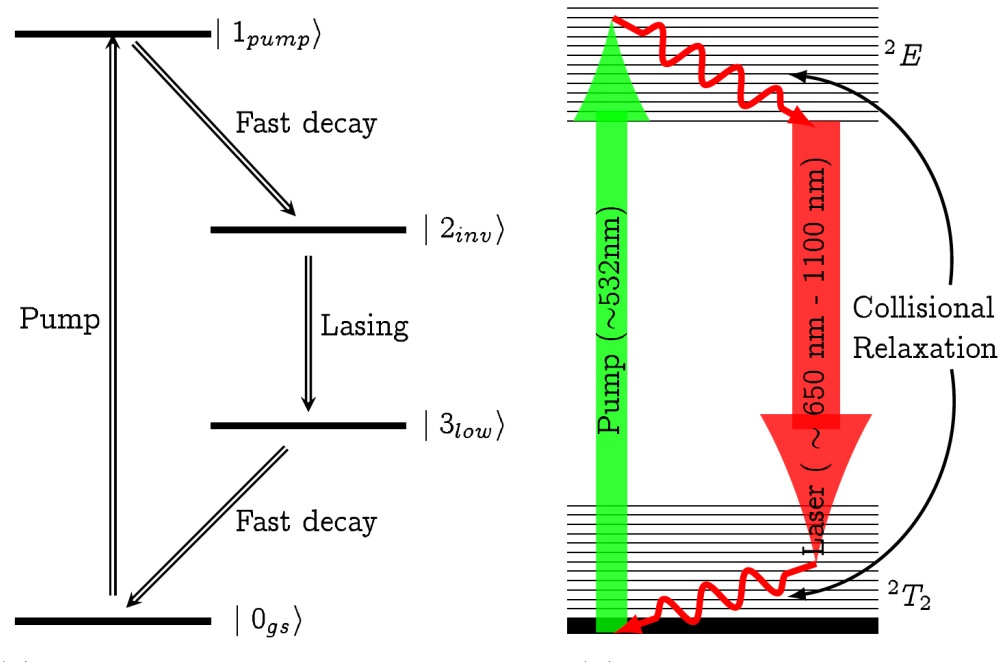

Figure 3.8: *Level structure of the Ti:sa active medium [89].*

Etalon

An etalon is a tiltable plane parallel glass plate with partially reflecting surfaces on both sides. On the etalon, a incident photon beam will split into multiple reflected and transmitted beams. The transmission T through the etalon will be dependent of the reflectivity R of both surfaces A and B.

$$T = \frac{T_A T_B}{1 + R_A R_B - 2\sqrt{R_A R_B} cos(\delta)} \tag{3.40}$$

For equal reflectivities the formula can by simplify to:

$$T = \frac{1}{1 + F sin^2(\frac{\delta}{2})} \qquad F = \frac{4R}{(1-R)^2} \tag{3.41}$$

where δ is the phase shift between two adjacent interfering partial beams.

$$\delta = 2k_2 d cos(\theta_r) \tag{3.42}$$

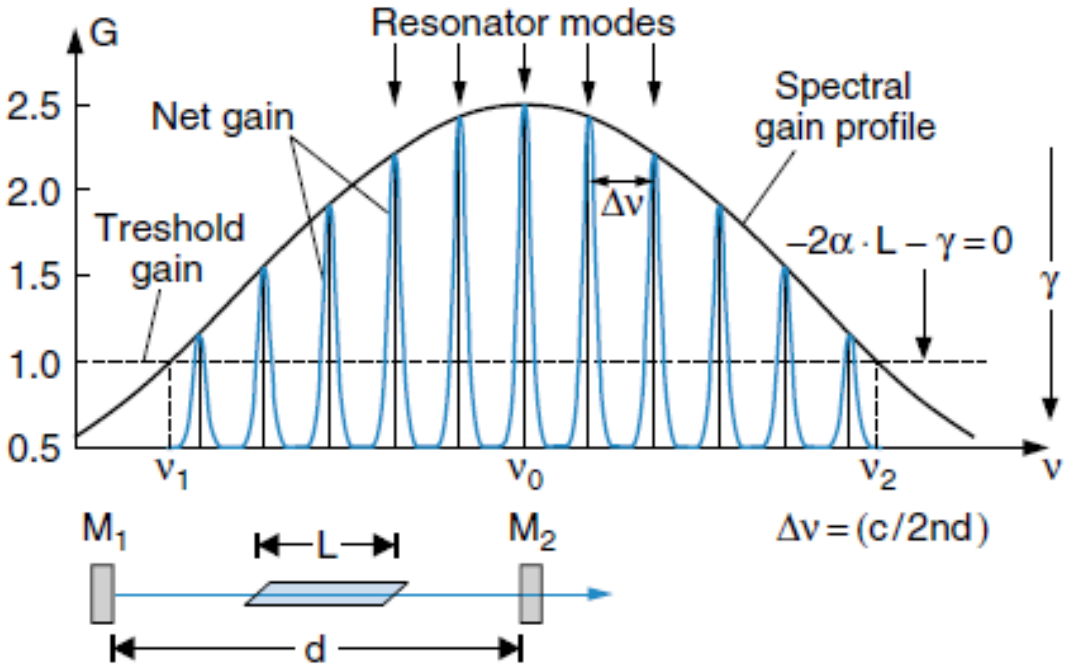

Figure 3.9: *Net gain for resonator modes within the gain profile of the active medium [70].*

being k_2 the wave vector of the light inside the etalon and θ_r the angle shown at Figure 3.10.

Equation 3.41 maximize when $\delta/2$ is a multiple of π. For a light beam with normal incidence Equation 3.41 has a maximum whenever the optical path length is a multiple of λ, leading to a transmission dependent on the laser frequency. The frequency separation between to transmission maximums is called the free spectral range (FSR) of the etalon.

$$\Delta f \;=\; FSR \;=\; \frac{c}{2nd} \tag{3.43}$$

where n is the resonator mode and d is the optical path length. The ratio between the FSR and the full width at half maximum (FWHM) of the transmission peak is directly related with the reflectivity of the surface mirrors. This ratio is also called the the Finesse $\mathcal{F}$.

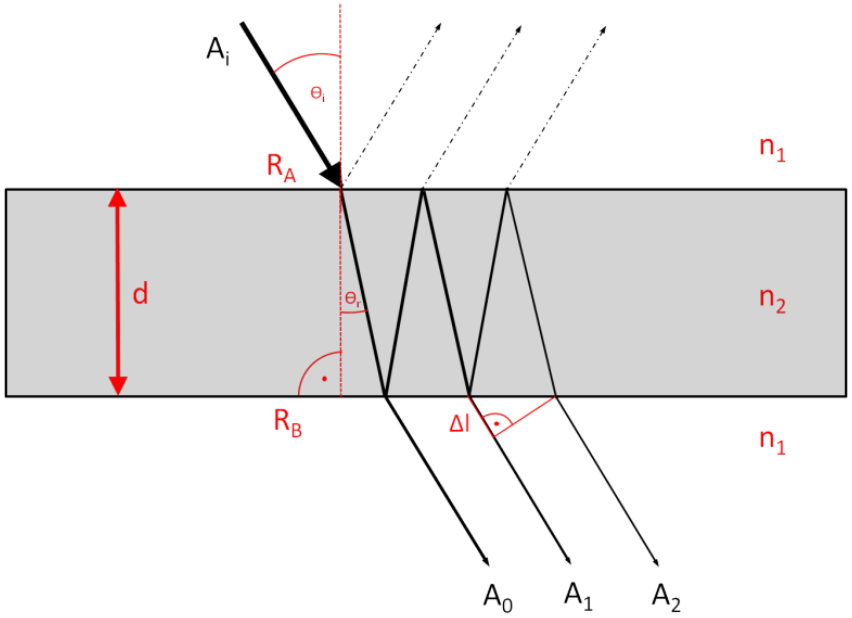

Figure 3.10: *Transmission of light through an etalon. Light enters with an angle of incidence θ_i and is partially reflected or transmitted at the surfaces with reflectivities $R_A$and R_B. Depending on the path taken the beams accumulate a phase delay δ [90].*

$$\mathcal{F} = \frac{FSR}{FWHM} = \frac{\pi}{2arcsin(\sqrt{1/F})} \approx \frac{\pi\sqrt{F}}{2} \tag{3.44}$$

Depending on the characteristics of the etalon and the resonator, the number of modes selected will be different. Figure 3.11 Finesse=50 present the best scenario where just one resonator mode is transmitted. In contrast, Figure 3.12 shows the transmission of several modes where the wavelength of the laser beam correspond to the central mode on the transmission pattern.

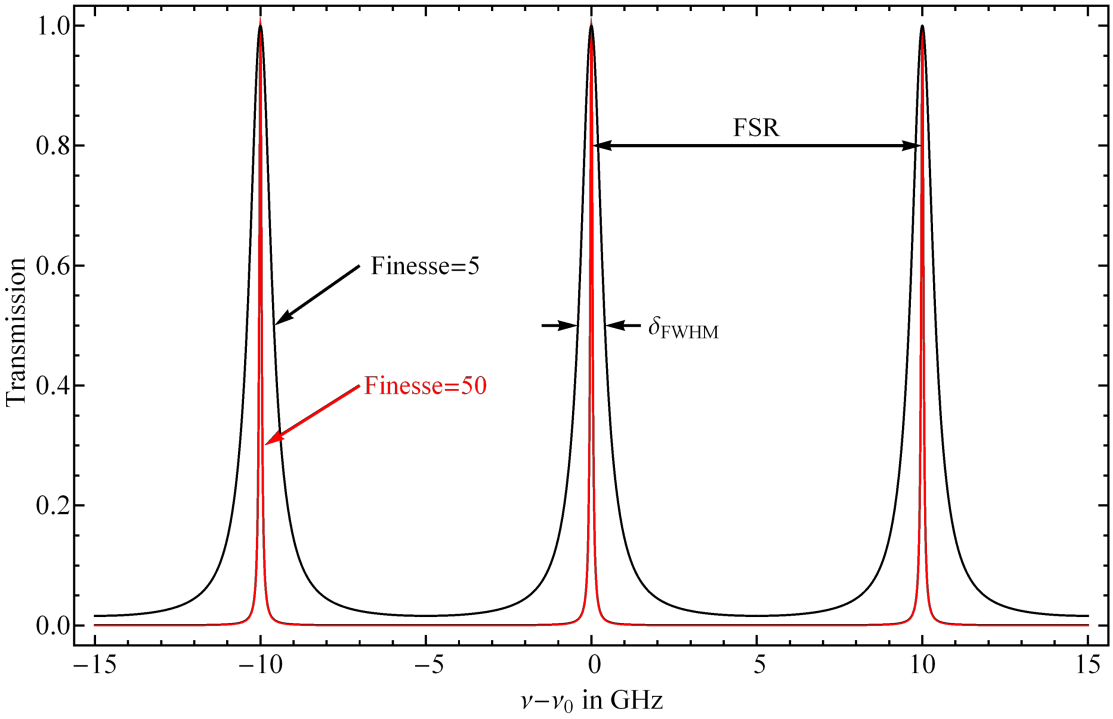

Figure 3.11: *Transmission curve of an etalon with a FSR of 10 GHz. The red curve shows the case with a finesse value of* $\mathcal{F} = 50$*, the black curve with* $\mathcal{F} = 5$ *[90].*

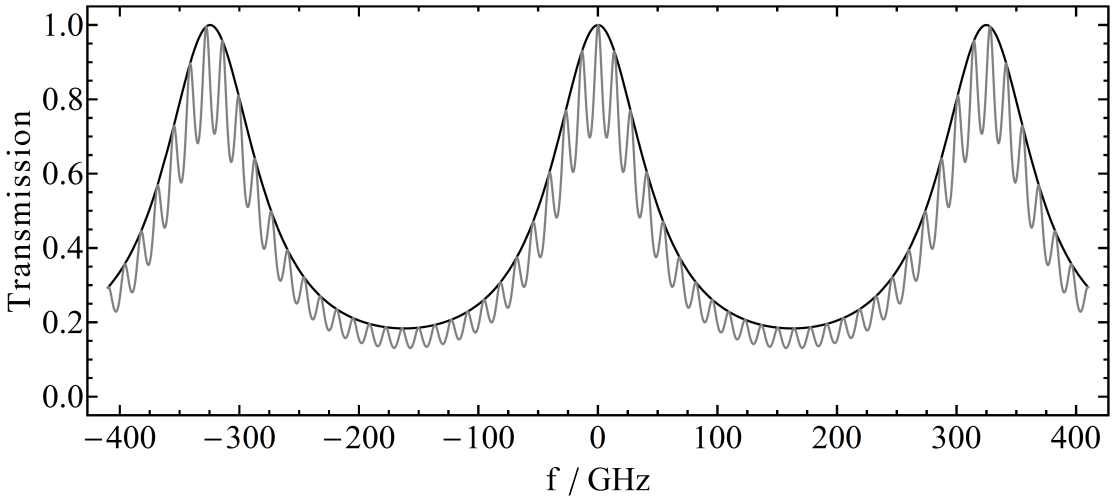

Figure 3.12: *Single-pass transmission curves of the thin (0.3 mm) etalon in black and the combination of thin and thick (6 mm) etalon in grey [90].*

3.4 Laser spectroscopy techniques

High resolution lasers can be used to resonantly excite electronic transitions in atoms and ions, and therefore, determine the transition energy. This method has proved to be a powerful tool to study the atomic nucleus leading to model independent data through the isotope shift and hyperfine structure [91, 7].

Laser spectroscopy techniques have been widely used at radioactive beam facilities to study the nuclear structure of exotic nuclei. The first review of this kind of measurements dates on 1979 [92]. Over the years, different laser spectroscopy techniques has been developed and will be presented in this section.

3.4.1 Collinear laser spectroscopy

In collinear laser spectroscopy, the ions are accelerated through a well-defined electrostatic potential, remaining the energy spread constant, resulting in a reduction of the velocity spread trough Doppler compression. As the Doppler broadening of the measured atomic transition is proportional to the velocity spread, the broadening decreases with increasing beam energy. By this method, the Doppler contribution can be minimized, achieving experimental linewidth similar to the natural linewidth of the transition.

$$\frac{d\nu_{lab}}{dE} \approx \frac{1}{\sqrt{2mc^2E}}\nu_{rest} \tag{3.45}$$

The ion beam is overlapped in collinear or anti-collinear geometry with one or several laser depending the detection technique. If only one laser is used, the excited ions or atoms will decay emitting a fluorescence photon. In contrast, several laser can be combined to resonantly ionize an atom. The first case is called fluorescence laser spectroscopy and the second is called Resonance Ionisation Spectroscopy (RIS).

Fluorescence

On fluorescence laser spectroscopy, an electron in low lying atomic state is exited to a higher state by a high resolution laser beam, followed by a fast decay by

isotropic photo-emission. After de-excitation, the fluorescent photon is detected using a photo-multiplier tube (PMT).

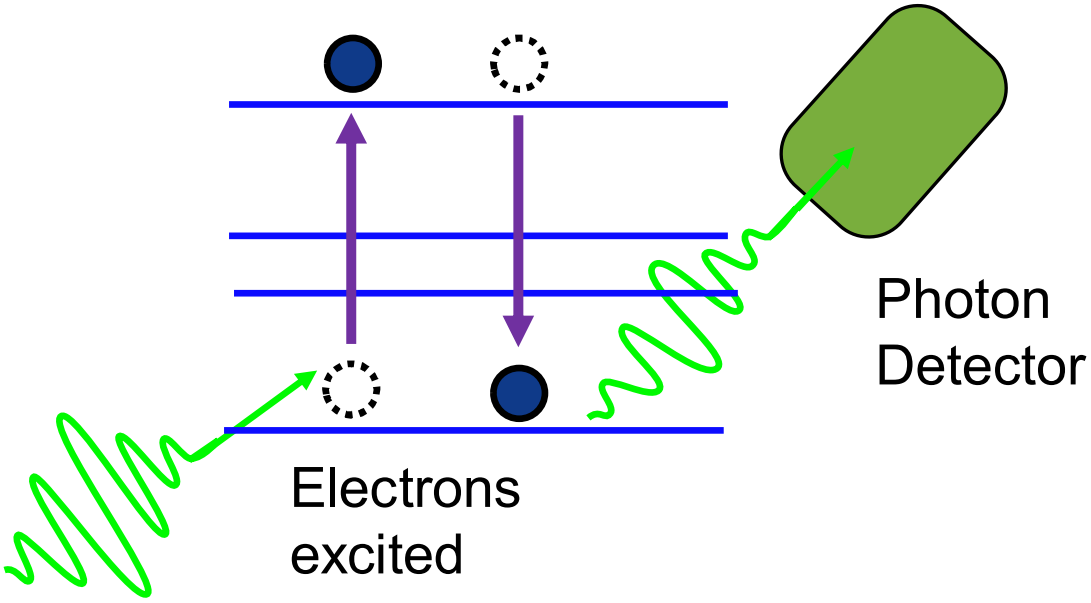

Figure 3.13: *Schematic representation of fluorescence laser spectroscopy.*

This technique requires yields of $\approx 10^4$ ions s^{-1} when bunched beams are used and there is hyperfine splitting. In case of a strong transition and I=0, spectroscopy can be performed with rates of hundreds of ions per second. The limitation is related with two factors. On one side, the detection is limited by the solid angle coverage and the low efficiency of the PMTs. On the other side, the signal-to-total ratio is hindered by the high background counting rate produced by the laser light scattered into the PMTs.

Resonance Ionisation Spectroscopy (RIS)

Resonance laser ionization consists on ionize an atom by promoting a valence electron over the ionization potential via resonant laser excitation of atomic transitions.

Generally, there are three kind of ionization schemes. Ionization can be achieved either by a non-resonant transition into the continuum, a resonant transition into an auto-ionizing state or by a transition to a Rydberg state where the ionization takes place either via collisions or electric fields.

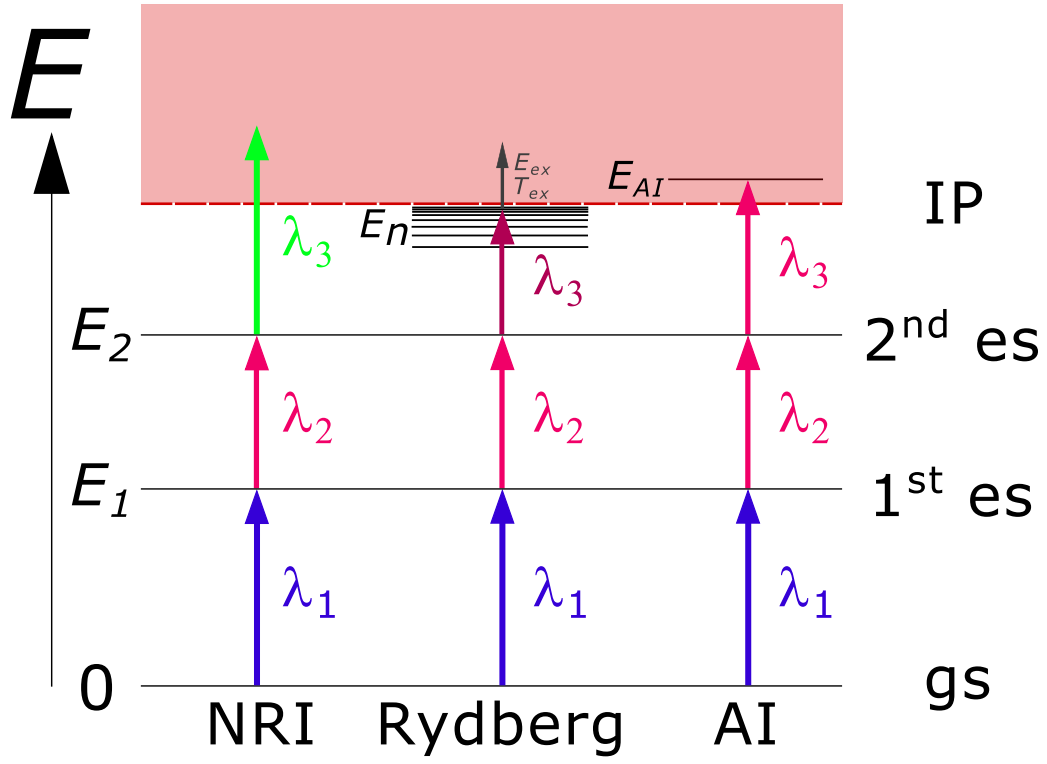

Figure 3.14: *Schematic presentation of atom ionization mechanisms using a three step excitation of the valance electron with lasers.*

The ions are separated to the atomic beam and either detected using a ion-detection technique or used to provide high purity ion beams.

Laser ionization needs high photon densities which are unavailable from typical continuous wave (CW) lasers. To achieve this level of photon densities the Q-switching technique allows to concentrate the laser power on high repetition pulses (usually 10 kHz). This technique consist on avoid population inversion keeping the quality factor (Q-factor) low by introducing loses on the resonator. At a certain time $t = t_s$, the Q-factor is suddenly switched to a maximum value starting a photon avalanche. This process is shown at Figure 3.15.

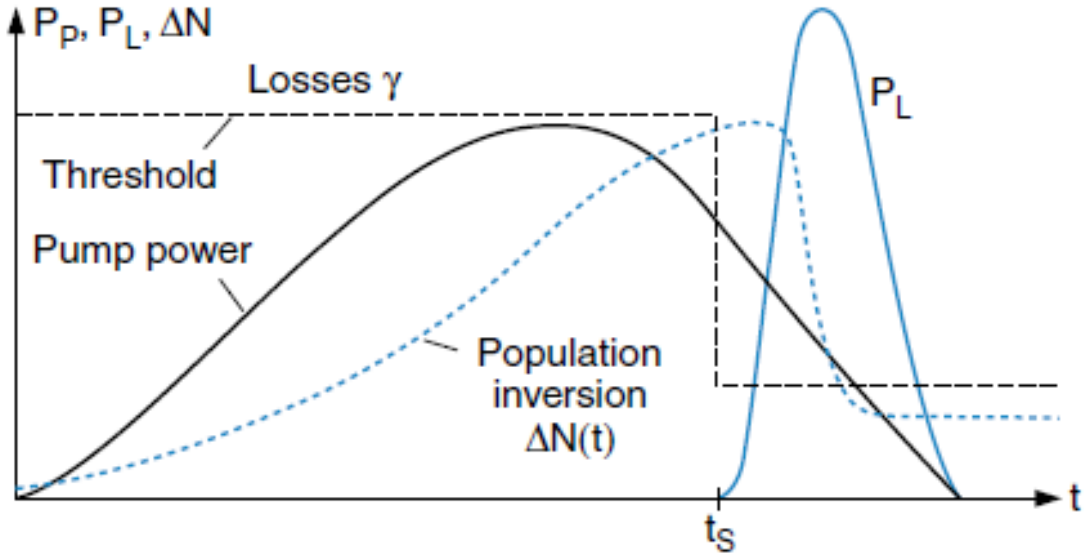

Figure 3.15: *Pump power $P_P(t)$, laser output power $P_L(t)$, and cavity losses $\gamma(t)$ for a Q-switched laser where t_s is the switch time [70].*

3.4.2 In-source laser spectroscopy

In-source laser spectroscopy consist on performing RIS directly into the ion source to extract the ions of interest. Performing laser spectroscopy at the secondary beam production source provides increased sensitivity allowing the study of more exotic cases.

Since its first application in 1992 [93], this technique has been regularly used in two types of radioactive ion beam facilities: thick-target hot-cavity facilities and thin-foil-target gas-catcher facilities. Laser ion sources have proven to be highly efficient with low background (depending on surface ion contamination), however its resolution is hindered by the environmental conditions.

The high temperature at hot-cavity facilities (≈2000 ∘C) induces a large velocity spread. This effect results on a significant Doppler broadening of the atomic spectral lines.

$$\Delta\nu_D \;=\; 7.16 \cdot 10^{-7}\sqrt{\frac{T}{M}}\nu_0 \tag{3.46}$$

where T is the temperature of the cavity in Kelvin, M is the atomic mass number

and ν_0 is the rest frequency of the atomic transition.

At gas-catcher facilities, the broadening effect are caused by the collisions of the atoms of interest with buffer gas atoms and molecules. In addition, the collision can induce a shift on the transition frequency. The new spectral line can be described by a shifted Lorentzian function [94]. The resulting pressure broadening has a similar magnitude than the Doppler broadening at hot cavity facilities [95].

3.4.3 In-gas jet laser spectroscopy

A new approach to improve the spectral resolution and selectivity of RIS at gas cell has been one of the most recent improvements on the field [94]. High-resolution laser spectroscopy in an expanding supersonic jet is possible thanks to the expansion and acceleration of the atomic beam in a cold and low density environment.

A Laval nozzle located at the exit of the gas cell is used to create an axisymmetric supersonic gas jet. The flow at the exit of the nozzle is characterized by the Mach number (M). As increasing the Mach number the velocity distribution of the gas jet becomes narrower (Figure 3.16), leading to a reduction of the Doppler broadening to $\approx$ 100 MHz [96].

3.4.4 Overview on laser spectroscopy techniques

A comparative summary of the key points of the three techniques is shown at Table 3.1. As each technique has its own strength, they complement each other in order to study the atomic nuclei. For this reason, laser spectroscopy is widely used on the accelerator facilities as is shown at Figure 3.17.

Table 3.1: *Comparison of key parameters for the laser spectroscopy techniques.*

	Collinear	**In-source**	**In-gas jet**
Resolution	$\approx$ MHz	$\approx$ few GHz	$\approx$ 100 MHz
Efficiency	10/s (RIS) or 100/s (Fluorescence)	0.01 counts/s	1 count/s

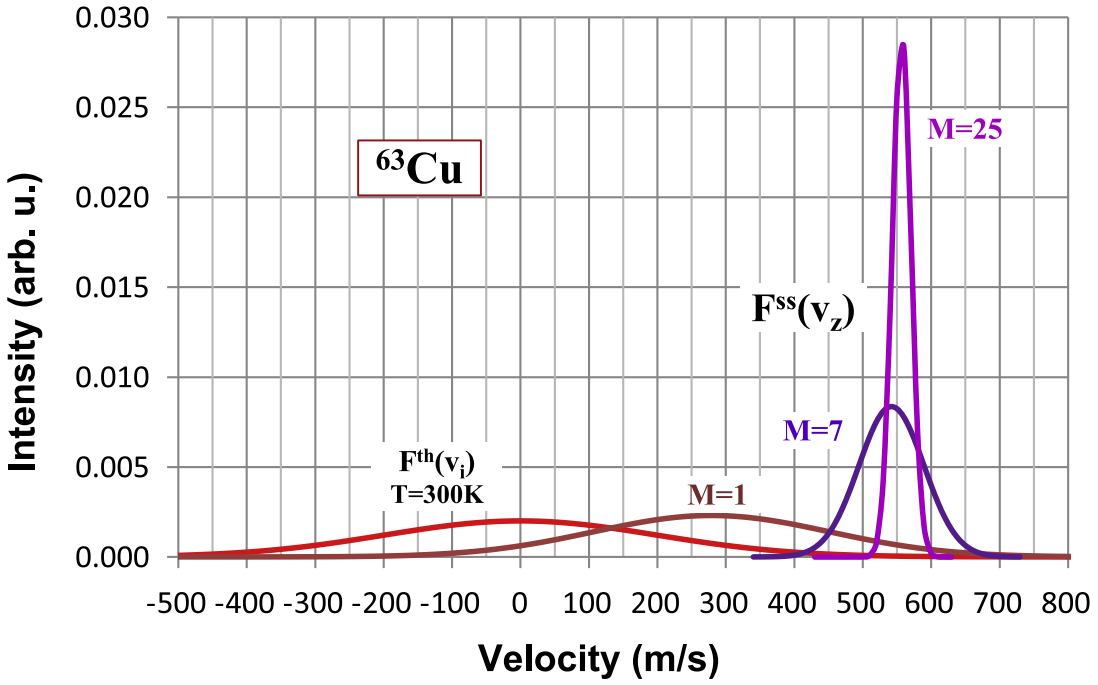

Figure 3.16: *One-dimensional velocity distribution of ^{63}Cu atoms in the gas cell ($F^{th}(\nu_i)$) and in the supersonic argon beam ($F^{ss}(\nu_z)$) for different Mach numbers and a stagnation temperature T_0=300 K [94].*

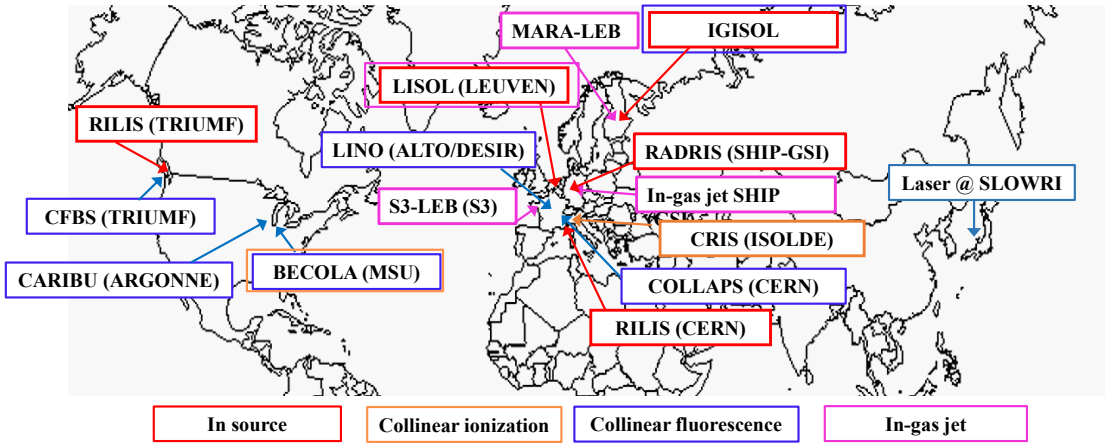

Figure 3.17: *Laser spectroscopy facilities around the world.*

Chapter 4

Experimental setup

At this chapter it is discussed the experimental setups that have been used during this PhD project.

4.1 Collinear experiment at IGISOL

The Ion Guide Isotope Separator On-Line (IGISOL) technique was implemented at the University of Jyväskylä in the early 1980s to provide radioactive ion beams of short-lived exotic nuclei for fundamental nuclear structure research and applications [97]. This technique was conceived as a novel variation to the helium-jet method [98].

The helium-jet method consisted on the thermalization of primary recoil ions from nuclear reactions in atmospheric helium. As in a stopping medium, the charge state of an ion is proportional to the speed in a stopping material [99], the recoils will remain in a charged form. Inside the helium chamber, an electric field generated by a set of electrodes will guide the ions through a very small nozzle and skimmer into a mass spectrometer [100].

The Ion Guide Isotope Separator On-Line (IGISOL) facility use an upgraded version of this method. At the IGISOL-4 facility, the projectile beam, coming from the K130 or MCC30 cyclotron, hits a thin target. The reaction product nuclei recoil out into a fast-flowing buffer gas, usually high purity helium. In the buffer gas, the recoil ions slow down and thermalize via charge exchange processes. The ions reaches a singly-charged state with a typical efficiency from 1 to 10% [101].

The He gas flow guide the ions into a radiofrequency sextupole ion beam guide (SPIG), which work using an RF frequency of ∼3-4 MHz and an RF amplitude up to 600 V [101]. The use of the SPIG not only improves the beam quality but also the transmission efficiency from the ion guide to the mass separator. A maximum transmission of 100% can be achieved up to currents of ∼100 nA (∼10^{12} ions s^1), however it descend up to 50% at ion guide currents of ∼600 nA [102]. The extracted ions are electrostatically accelerated using 30 keV potential. An overview of the evolution of the production technique at the facility over the years (up to 2013) can be found at [102].

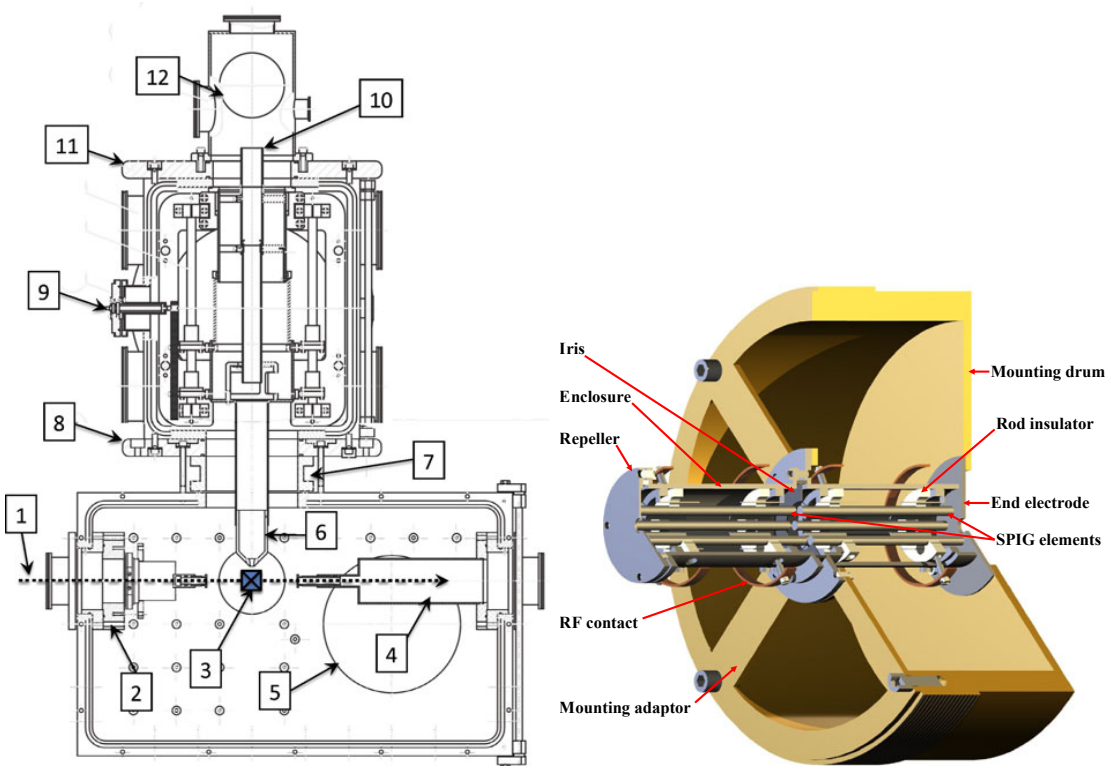

Figure 4.1: *The technical drawing of the target and the extraction chambers. 1) Cycloton beam. 2) Water-cooled beam collimator. 3) Position of the ion guide. 4) Beam enclosure, leading to the beam dump. 5) 300 mm pumping channel to the roots array. 6) Extraction electrode (SPIG - Figure on the right [102]). 7) 200 mm gate valve. 8) Insulator between target chamber and the extraction chamber. 9) Extraction electrode moving mechanism. 10) Ground electrode. 11) Insulator between extraction chamber and ground. 12) Beam diagnostics chamber [103].*

Commonly, at ISOL facilities the ions of interest are extracted from the target material through thermal diffusion by heating the target to about 2000 degrees. The key point of the IGISOL production method is its chemical insensitivity,

making it able to produce refractory elements which are highly resistant to heat. However the He gas purity plays a critical role in ion guide operations needing impurity levels below sub-parts-per-billion [104]. To achieve this purity, He gas is purified using a cold trap. The cold trap consist in a 'U' form tube which bottom is inside a dewar flask filled by liquid nitrogen. All gases composing the beam who are not He are condensed and trapped in the bottom part of the tube. The operation pressure is in a range between 100 and 300 mbar in the ion guide area, selecting the operation pressure for each reaction to maximize the production.

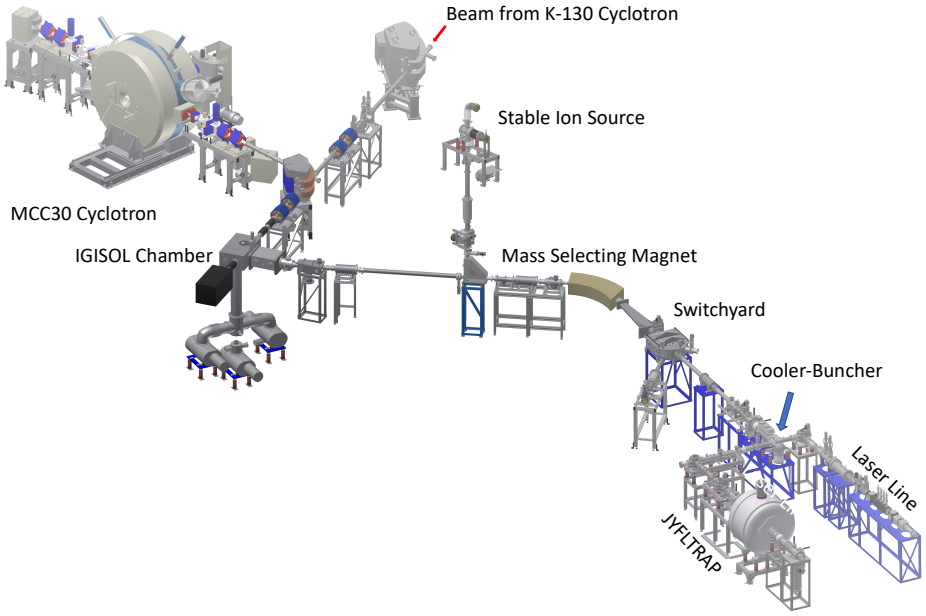

Figure 4.2: *Layout of the IGISOL-4 facility [105].*

In addition to the online production at the target chamber, there is a offline ion source station to provide stable ion beams during the measurements. The ion source station is composed by a surface ion source and a glow discharge ion source [106]. The surface ion source produce ions creating a cloud of ions by heating a mixture of potassium, rubidium and cesium. The glow discharge ion source induce high-voltage discharge sparks which ionise the helium buffer gas surrounding a cathode, causing fragmentation of the cathode material by electric discharge. After the ion creation, a skimmer electrode form an ion beam which is accelerated to 30q keV by an extractor electrode.

Both, offline and online, ion beams are mass separated using a 55 degrees dipole magnet with a mass resolving power $\frac{M}{\Delta M} \approx 500$. Once mass separated the ion beam is guided to the decay spectroscopy line, the cesium atom trap station or

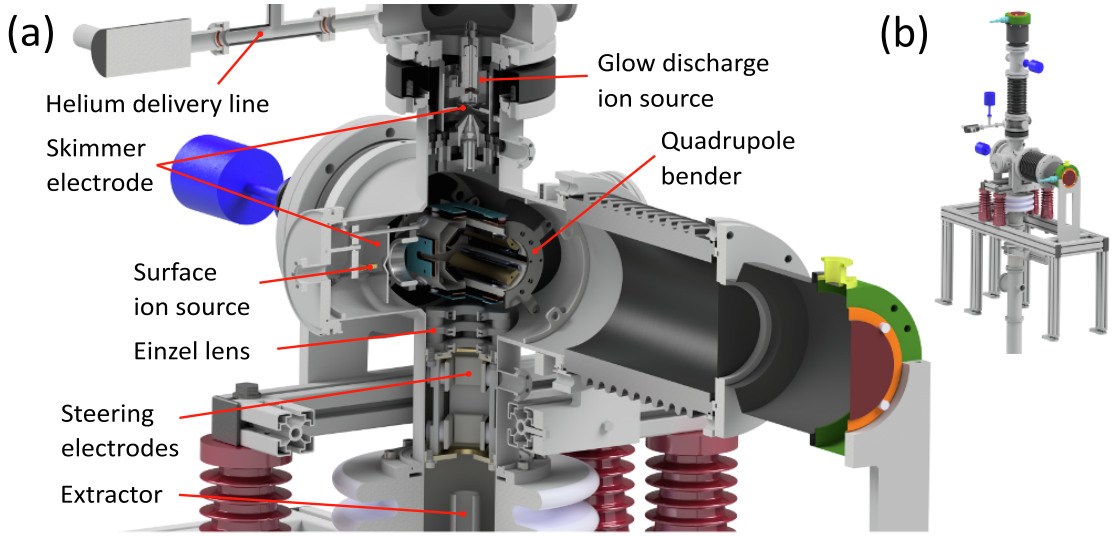

Figure 4.3: *Internal structure of the new off-line ion source station (a) and the full station (b) [106].*

to the radiofrequency quadrupole (RFQ) cooler-buncher using the electrostatic switchyard.

The ions are decelerated as they enter the cooler to ∼50 V and are focused into a quadrupole by two cylindrical electrostatic lenses. At the cooler the ions suffer repeated collisions with helium atoms (pressure ∼0.1 mbar) meanwhile are radially confined by the use of a segmented radiofrequency quadrupole to improve the emittance and energy spread below 1 eV [107]. The ions are trap at the end of the cooler by applying +20 V on the end-plate electrode creating a potential barrier to accumulate the ions. The ions are accumulated typically for a few hundred milliseconds and, then, are released during 100 μs, the time-width of the bunch is about 10 20 μs, at an energy of 800 eV. The transmission efficiency trough the cooler-buncher is 60-70% [108]. The bunched beam compared with a continuous ion beam, has background level a factor $\sim 10^4$ lower, by gating the time of flight (TOF) signal (see section 6.1).

4.1.1 Collinear laser spectroscopy beamline

From the cooler-buncher, the ions can be injected into the JYFLTRAP or into the collinear beamline via a serie of 90 degree quadrupole benders. Before entering the line, the ions are accelerated to 30 kV. At Figure 4.4 is showed schematically the

Light Collection Region including the diagnostics for beam tuning and monitoring.

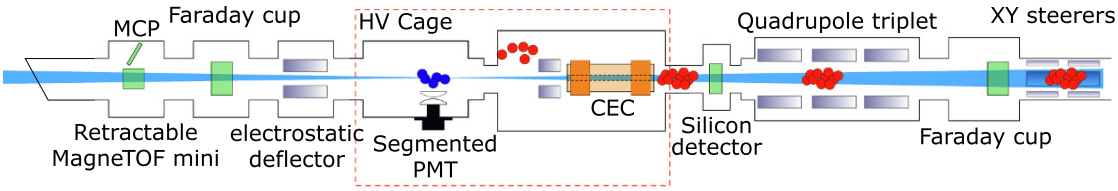

Figure 4.4: *Schematic view of the IGISOL's collinear beam line. The laser light is coming from the left and the ions (red) from the right.*

Depending on the selected atomic transition, the ions may need to be neutralized. The neutralization process takes place on the Charge-Exchange Cell (CEC) via electron-capture reactions with an alkali vapour. The CEC consist on a cylinder filled with a potassium or sodium vapour created by heating the cell applying a variable AC potential. The extremes of the cylinder are cooled using a Lauda RA-8 oil circulator to keep the neutralizing element inside the cell. The reaming ions are removed from the atomic beam by a pair of electrostatic deflector plates. The CEC was designed for the collinear beamline at the TRIGA facility in Mainz, Germany [109].

Before neutralization, a tuning voltage is applied through a x1000 TREK 609E-6 high-voltage amplifier (-4 to 4 V) to the platform supporting the charge-exchange cell and Light Collection Region (LCR). The adjustable acceleration voltage allows to scan the laser frequency across the resonances by Doppler shifting the apparent laser wavelength in the rest frame of the atoms. This shift can be calculated using the relativistic Doppler shift formula:

$$\nu_{rest} = \nu_{lab}\frac{1+\beta}{\sqrt{1-\beta^2}}, \qquad \beta = \frac{v}{c} = \sqrt{1 - \frac{m^2c^4}{(eV + mc^2)^2}} \tag{4.1}$$

where m is the atomic mass, ν_{lab} is the laser frequency and V is the combination of the cooler voltage and the tuning voltage $V = V_{cool} + V_{tun}$. A previous study on the cooled ions showed than an offset of 15.1(14) V has to be added to the cooler voltage to obtain the real beam energy [110].

The atom beam is then focused in front of the segmented Photo-Multiplier Tube (PMT) in the LCR using a quadrupole triplet and overlapped anti-collinearly with the laser beam.

The signal of the PMT is sent to an electronic chain composed by a fast timing amplifier, which amplifies the signal before the Constant-Fraction Discriminator

(CFD). The signal is then converted to a temporal signal by a Time-to-Digital Converter (TDC) with four channels with a 500 ps single-shot resolution. The TDC and the cooler-buncher are triggered by a pulse generator and a digital multimeter to ensure synchronisation. The time-signals from the PMT segments, the RFQ cooler platform, tuning voltage and the wavemeter readout are recorded by a new Python (EPICS-based) data acquisition system which was installed in 2018 [110].

Collinear spectroscopy laser system

The laser beam for collinear laser spectroscopy consist on two Sirah Matisse 2 continuous wave (cw) lasers, a dye laser and a Ti:sapphire laser. The Ti:sapphire laser have been the one used for the palladium measurement and its layout can be shown at Figure 4.5. For this cavities, the laser frequency mode is selected by scanning the birefringent filter and the thin etalon, and then the single mode is achieve by an aditional piezo-driven Fabry-Pérot interferometer (thick Etalon). The piezo is coupled via a feedback loop with an external reference cavity to ensure short-term stability. To avoid long term frequency shifts, the wavelength of the cavity can be locked using a WSU-10 wavemeter and frequency-stabilised HeNe laser using a transfer cavity.

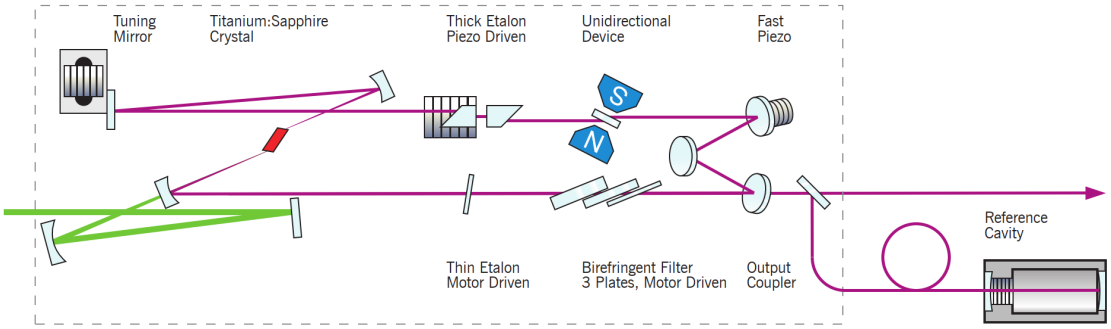

Figure 4.5: *Optical layout of the Sirah Matisse 2 cw Ti:sapphire laser [111].*

The transfer cavity allows absolute frequency stabilization, creating a master-slave relation between the HeNe laser (master) and the Matisse cw cavity (slave). Both laser are superimposed at the reference cell and then split again to achieve a separated acquisition for each laser. The stabilization is performed adjusting the reference cell length with a side-of-fringe locking method, using the intensity measured by the HeNe photodiode. This information is sent to the Matisse control software by a digital plugin. As a result, a change on the absolute frequency of

the Matisse laser will affect the frequency stability of the HeNe laser. A schematic layout of the transfer cell can be observed at Figure 4.6

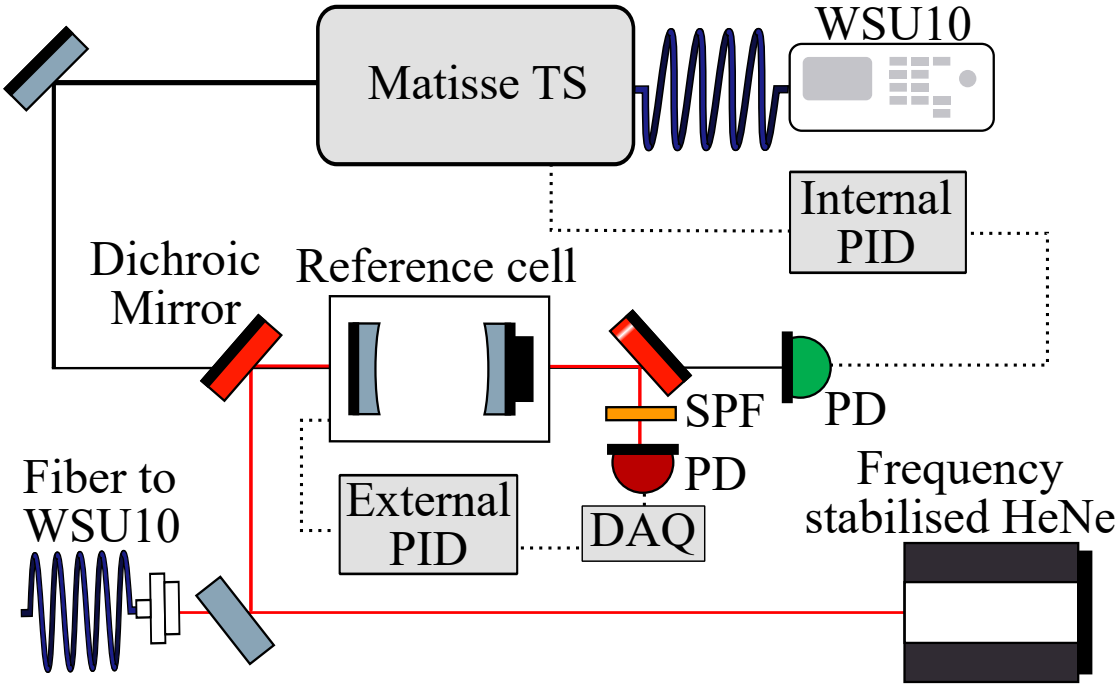

Figure 4.6: *Schematic of the transfer cavity implementation for the cw Ti:sapphire laser. PD = Photodiode, SPF = Shortpass Filter. [79].*

The cavities are pumped by a 20 W Spectra Physics Millenia eV laser. In addition, the laser system includes two WaveTrain 2 doubling units which can work separately for frequency-doubling or together for frequency-quadrupling. The second harmonic generation is achieved on a triangle shaped enhancement cavity containing a nonlinear BBO crystal with temperature stabilization.

4.2 Hot cavity laser spectroscopy setup (JYU)

To overcome the low efficiency of the ion-guide technique, an inductively heated hot cavity catcher has been constructed at the IGISOL facility. The aim of this new technique is the production of low-energy ion beams of exotic isotopes towards the N = Z line using heavy-ion fusion-evaporation reactions.

This method was initially propose to measure neutron-deficient Ag isotopes [58]. Previous work at GSI showed that silver could be released from a graphite catcher

in a time scale of ∼10 ms and with a corresponding extraction efficiency close to 50% [112]. This values of delay time and efficiency are dependent on the chemical properties and the catcher temperature. The catcher and crucible design is an adaptation from the existing electron-bombardment-based FEBIAD (Forced Electron Beam Induced Arc Discharge) and thermal ionizer concepts [112, 113].

The ion beam coming from the cyclotron impinge on a circular target foil stack mounted in the molybdenum crucible. The reaction products recoil from the target and are implanted into 100 μm thick graphite (Grade 5890PT from Le Carbone-Lorraine) catcher, with a mean grain diameter of 20 μm. The catcher is located in a cylindrical cavity (4 mm depth × 9.1 mm diameter) inside the molybdenum crucible and sealed with a tantalum window (2 μm thick). A 1.2 mm diameter exit hole on the cavity allows diffused atoms to effuse into a 60 mm long graphite transfer tube of diameter 4.3 mm. The transfer tube confine the atoms for efficient laser ionization, while the ions are extracted quickly and efficiently into the sextupole ion guide (SPIG) introduced on the last section(section 4.1).

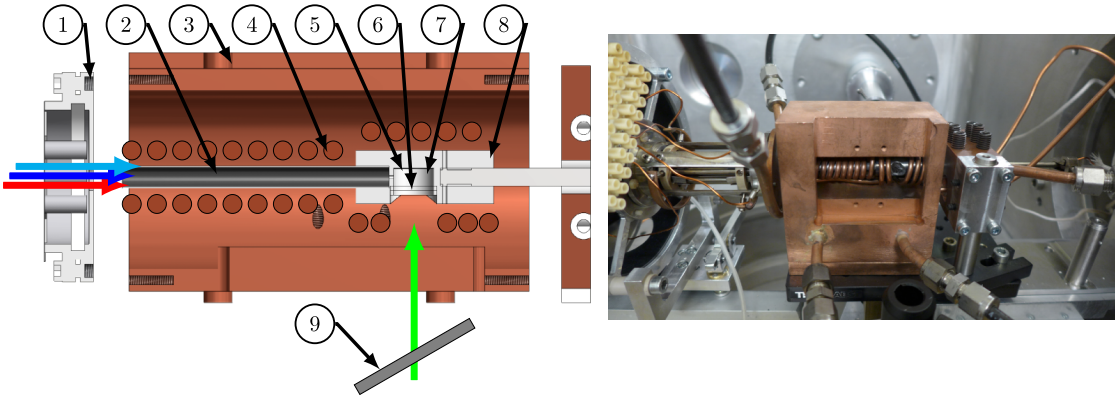

Figure 4.7: *A schematic diagram of the hot cavity catcher (left) and a photograph of the experimental set-up without the degrader (right). The green arrow indicates the primary beam or recoil products. The lasers enter the transfer tube via the SPIG from the left. Labeling as follows: 1. SPIG entrance, 2. Graphite transfer tube, 3. Water-cooled heat shield, 4. Copper coil, 5. Graphite catcher, 6. Ta window, 7. Hot cavity, 8. Mo crucible, 9. Ni degrader foil. [114]*

The catcher, crucible and target are heated by an UltraFlex SM-2/200 induction heating system (2 kW). Besides, the transfer tube is heated resistively using a Delta Elektronika SM 30–100 D DC power supply (providing ∼80 A). Due to the properties of graphite, additionally to heating the tube, the current also creates a few Volt potential gradient along the tube length [115]. Both crucible and transfer tube are covered by a water-cooled copper block.

A efficiency of 1% after the mass separator and a few tens of ms mean delay was determined in a previous measurement by implanting a ^{107}Ag beam from the K-130 cyclotron [114].

The effused ions are selectively ionized by a resonant laser ionization scheme inside the transfer tube. After this point, the path followed by the ions (shown at Fig. 4.8) is equivalent to the IGISOL beamline described at section 4.1.

In case of measuring exotic isotopes, resonant laser ionization will be combined with the JYFLTRAP double Penning trap [116], in order to achieve high purification and high counting sensitivity. However, for the stable palladium production test performed during this thesis, the ions of interest will be measured by a Faraday cup (FC) located after the dipole magnet (see section 8.1).

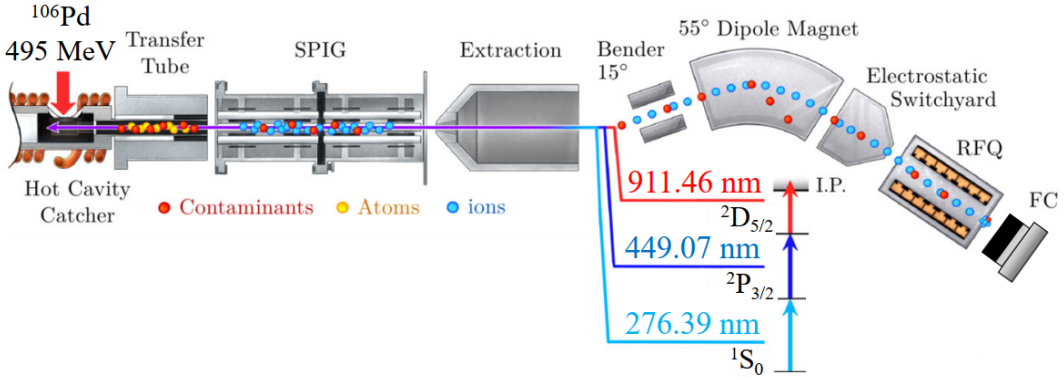

Figure 4.8: *Overview of the experimental setup used during the production test.*

4.3 GISELE laboratory (GANIL)

GISELE (Ganil Ion Source using Electron Laser Excitation) is an offline laser laboratory located inside the GANIL facility. Been initially conceptualized as a Resonant Ionization Laser Ion Source (RILIS) for SPIRAL2 [117], GISELE is used as laboratory to perform offline laser ionization and spectroscopy experiments for the elements of interest to be measured at the S3-LEB facility [118].

The layout of the GISELE laboratory is shown at Figure 4.9. The GISELE laser system provides the laser frequencies to selectively ionize the difused atoms created by resistive heating at the Atomic Beam Unit (ABU). This work is perform to

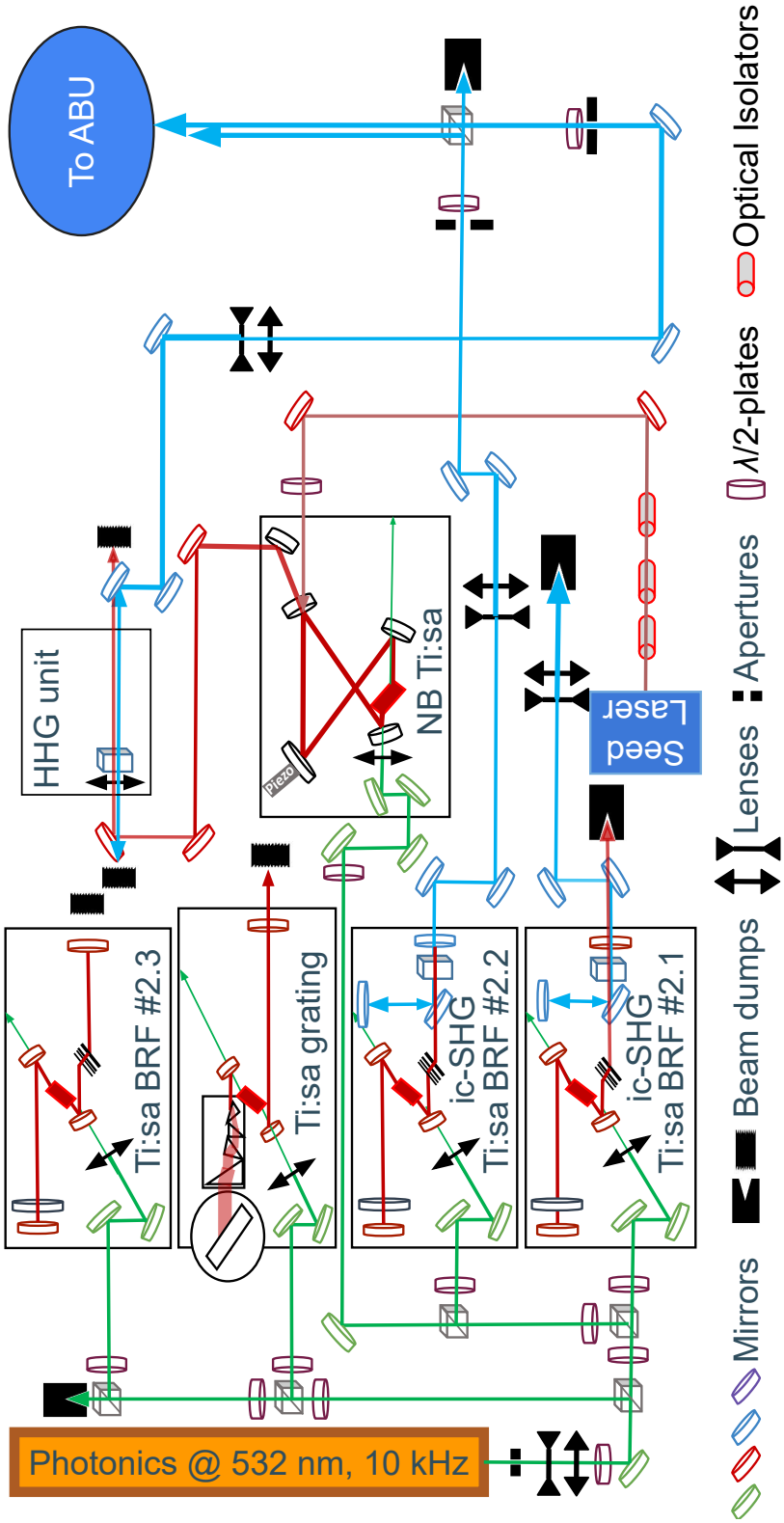

Figure 4.9: *GISELE laboratory layout. The colors represent the wavelength range(red-infrared, green, blue, ultra-violet). [118]*

develop and test resonance ionization schemes (RIS) for their future use at online experiments.

The laser system is composed by Ti:sa solid state lasers which are pumped by a Nd:YAG pump laser with a 10 kHz repetition rate. The pump beam is separated and guided into five different Ti:sa cavities by polarizing beam splitter (PBS) cubes. These cubes split the beam into its two polarities, being the p-polarized beam parallel and the s-polarized beam orthogonal to the input. Taking advantage of this fact, the power distribution into the cavities is implemented by $\lambda/2$ retardation plates located in front of each cube.

Four of the five Ti:sa cavities provides broadband laser beam, beig Z-shape geometry resonators. For three of these cavities, the wavelength selection is perform by a combination of a birefringent filter (BRF) and a solid (thin) etalon. Broadband cavities with this configuration provide laser beams with a linewidth of about 5 GHz. These cavities have the capability to produce a second harmonic generation (SHG) by placing a SHG crystal inside the laser resonator between the curve mirror SWP1 and the output coupler (OC) (see Figure 4.10). Intracavity-SHG gives some benefits for second harmonic generation as having a Gaussian beam profile, no focusing inside the crystal and increased tuning range.

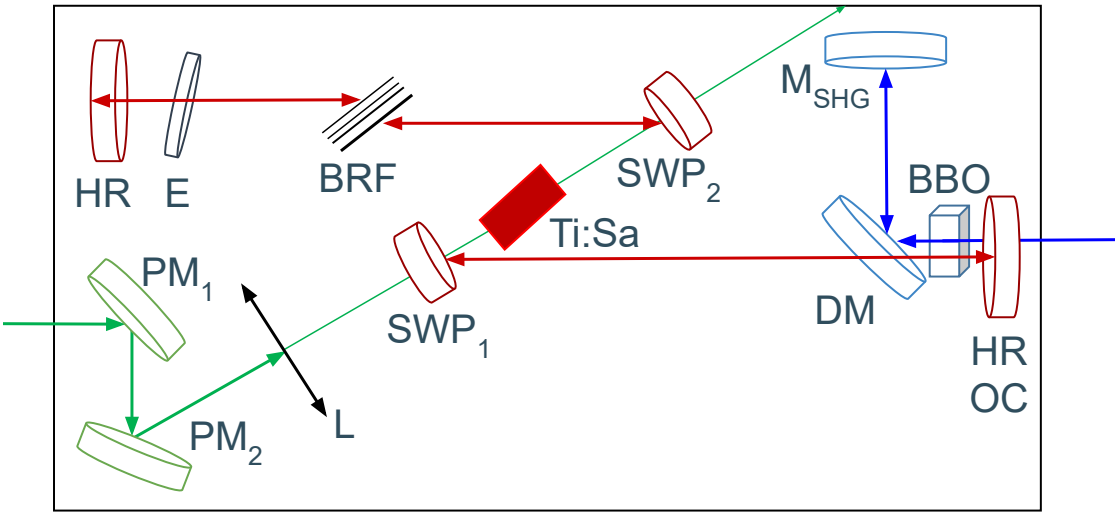

Figure 4.10: *Ti:sa laser layout with the intracavity-SHG.*

The remaining broadband cavity is a grating Ti:sa cavity. In this case, the wavelength selection is performed by a gold-coated plastic diffraction grating in the Littrow configuration operating at 1st order of diffraction fixed onto a off-the-shelf rotary stage. In order to avoid problems at the grating due to the heat, the laser

beam is expanded using a set of four prisms. Compared with BRF, grating Ti:sa cavities have the advantage of longer scanning ranges (more than 100 nm), with the drawback of providing less laser power.

The last cavity is a Injection-Locked Narrow-bandwidth (NB)/Single-mode (SM) Ti:sa. Unlike the previous cavities, the linedwidth of the laser beam provided by this cavity is not a limiting factor for resolving the hyperfine structure. With the NB cavity is possible to measure resonances with FWHM smaller than 100 MHz. The reduced linewidth is achieved by amplifying the light produced by a single-mode (SM) continuous wave (CW) seed laser in a master-slave feedback loop.

The NB Ti:sa has a bow-tie-shape geometry resonator. The pump (Nd:YAG) and the seed enter the cavity in opposite directions and are overlapped inside the ring resonator. To favor the seed and maximize the amplification, the length of the cavity is adjusted by a piezoelectric piece attached to one of the cavity mirrors, locking the resonator into a length proportional to λ_{seed}. The locking process is perform by active resonator stabilization electronics which follow any changes of the seed laser and suppress any internal and external instabilities.

The lock-in of the cavity is rule by a phase-sensitive modulation/dithering-locking technique [119]. The digital stabilization system is TEM Messtechnik, model: Laselock 3.0 with controls the voltage supplied to the Piezomechanik GmbH, model: HPSt 150/14-10/12 VS22 piezoelectric piece. Some of the seed beam escape the ring resonator being transmitted through one of curve mirror, this light is used as an input signal by an amplified photodiode (PD). The read out of the PD is a constructive interference pattern similar to those of a SFPI, being the x-axis the voltage of the piezoelectric piece. The system is locked at the point of maximum transmission of the seed pattern.

The seed beam for the NB-cavity is provided by ECDL laser diodes/gain chips (Manufacturers: Toptica/Eagleyard) with the maximum output powers between 50 and 150 mW. The control unit of the diode is a Toptica, model: Sys DC 110 which also works as a power supply.

An additional external unit is used to third harmonic generation (THG). The laser beam provided by one of the Ti:sa cavities enters the THG unit, been focused by a lens into a barium borate (BBO) nonlinear crystal for second harmonic (blue) generation. The fundamental (red) and the blue beam are separated by a dicroic mirror. The beam shape and the polarization of the blue beam are corrected by a cylindrical convex lens and a $\lambda/2$ waveplate, respectively. The polarisation is

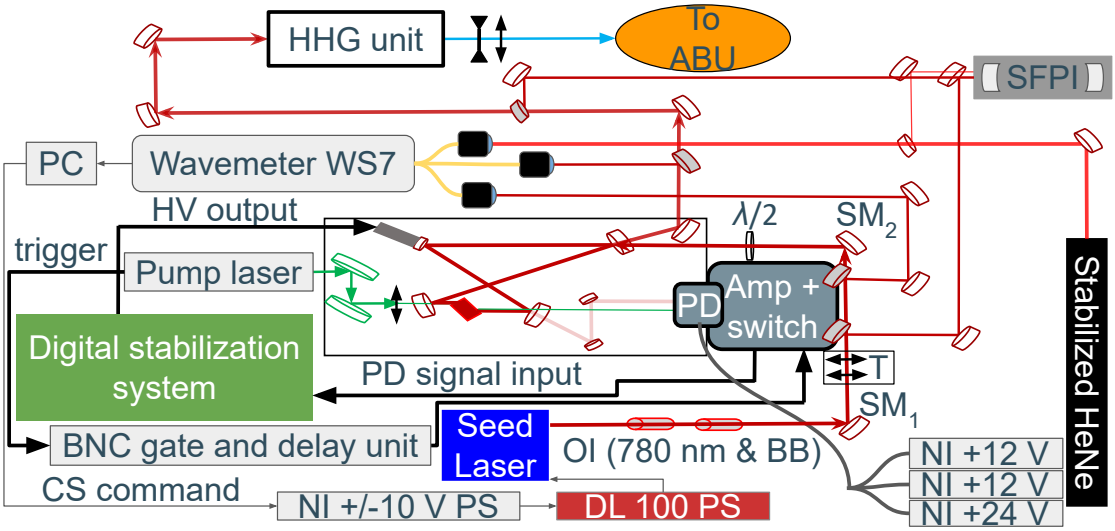

Figure 4.11: *Narrow bandwidth (NB) single mode (SM) Ti:sa laser system layout. BNC -function generator; DL 100 PS - master laser power supply; HHG unit: higher harmonic generation unit; NI ±10, 12, 24 V - National Instruments voltage supplies; OI - optical isolators; PD and Amp + switch - photo diode and its gated amplifier; SFPI - Scanning Farby-Perot interferometer; SM1,2 - seed laser mirrors; T - telescope; λ/2 - retardation wave plate. [120]*

changed as has to match with the P polarization of the fundamental beam. Both beams are again overlapped and focused into a BBO(THG) crystal. A schematic layout of the THG unit is shown at Figure 4.10.

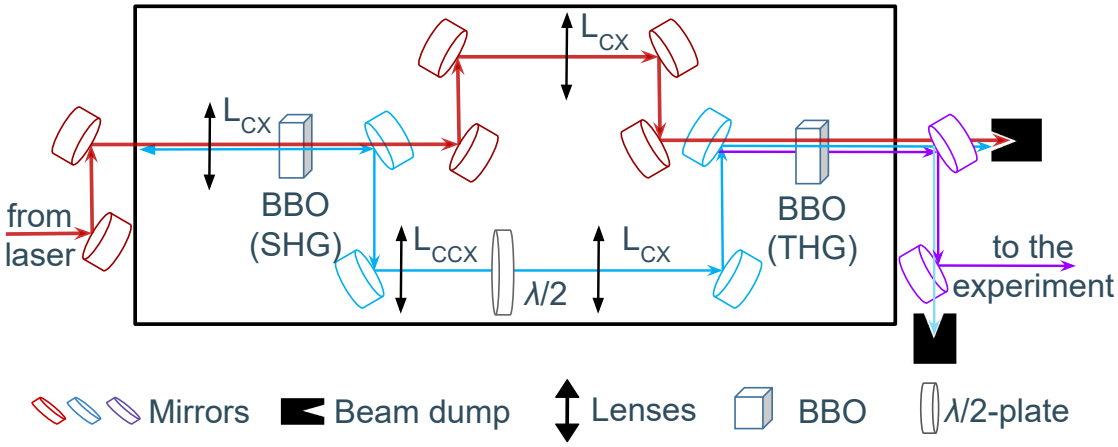

Figure 4.12: *GISELE THG unit. [120]*

Once the laser wavelengths required for the RIS are produced, the laser beams are

overlapped by PBS and guided towards an atomic beam unit (ABU).

The ABU has been developed at KU Leuven [121] and adapted at GANIL. The atoms are produced by evaporating a sample deposited on a crucible, which has a filament surrounding it. The atoms are diffused in the upward direction, while the surface ions are suppressed by two electrode pairs. The atoms are then collimated by multiple apertures until they reach the photon-atom interaction region. The atoms are selectively ionized by the laser beam in a transverse geometry and then accelerated and guided by a orthogonal electric field gradient, created by two electrodes, towards an micro-channel plate (MCP) detector located ≈50 cm located inside the time-of-fligth (TOF) tube.

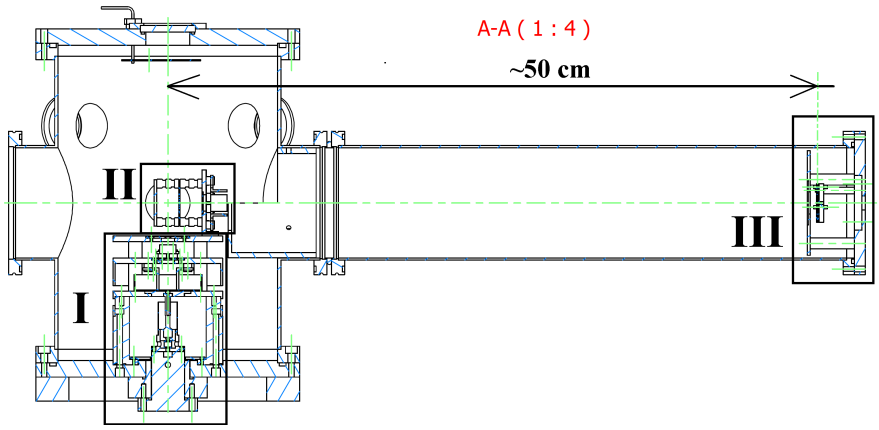

Figure 4.13: *Atomic beam unit (ABU) cross-section. (I) atom source region. (II) photon-atom interaction region. (III) TOF tube region. [121]*

The signal generated by the MCP is first sent to a fast amplifier, then to a constant-fraction discriminator (CFD) and finally to a time-to-digital converter (TDC) developed by KU Leuven. The time gate of the TDC is triggered by a TTL signal synchronized with the Q-switch trigger which rules the Nd:YAG pump laser.

Chapter 5

Development of optical elements

In laser spectroscopy, providing accurate laser frequencies is crucial to the success of the measurements. In this chapter will be presented the work performed on the development of optical elements to support laser spectroscopy.

5.1 Air-spaced etalon

As has been introduced at section 3.3.3, an etalon is a wavelength selective element used at laser cavities. Commonly, the wavelength selection is performed by tilting a solid etalon. By changing the angle of incidence, the path length inside the piece varies and therefore, the wavelength. However, this method also introduces power loses due to the extra path.

In order to avoid the power loss, the development of an air-spaced etalon was proposed. The air-space etalon is composed by two beam sampler crystals [122] facing each other and separated by a piezoelectric piece [123]. The piece is equivalent to a Fabry-Pérot Interferometer (FPI) [124], where the path length inside the piece varies using a movable mirror (Figure 5.1).

During this section, the test and development of a prototype of an air-spaced etalon will be presented. The section is divided in three parts, the preliminary test after the construction, the performance test on a Ti:sa cavity and the prove of principle test on a hot cavity laser spectroscopy measurement.

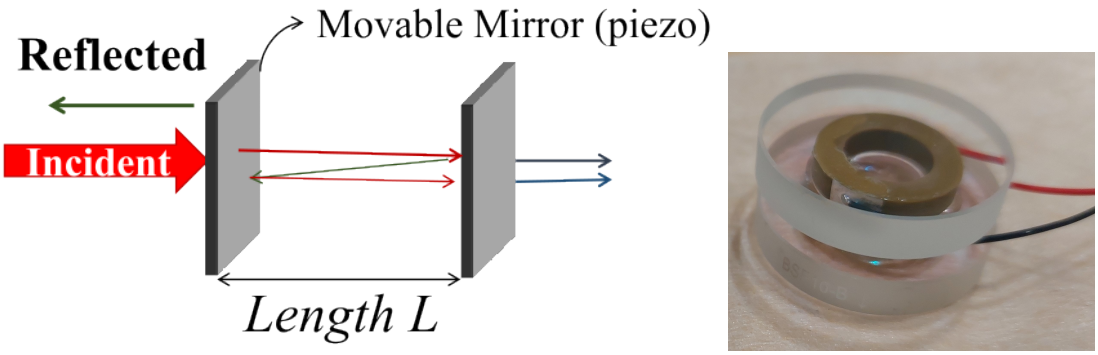

Figure 5.1: *Left) Schematic representation of the working principle of an air-spaced etalon. Right) Homemade air-spaced etalon.*

5.1.1 Preliminary tests

In order to characterize the overall features of the device, the air-spaced was studied using a Helium-Neon (Hene) laser and a photo-diode as is shown at Figure 5.2. The Hene laser was chosen because it is a continuous wave laser with a stable and well defined wavelength.

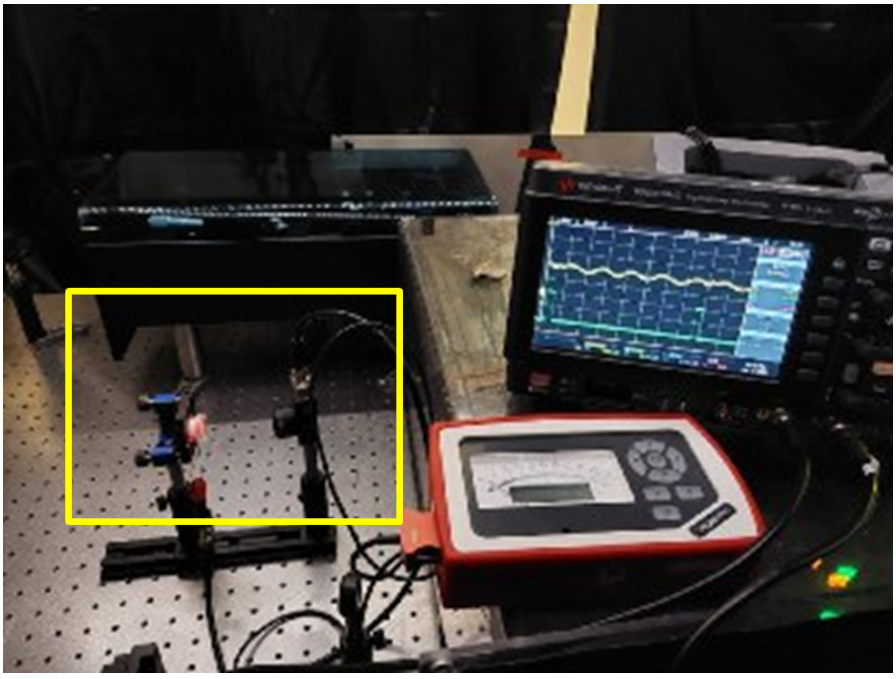

Figure 5.2: *Experimental setup used to perform the preliminary test to the air-spaced etalon.*

The Hene laser light detected by the photodiode will present a transmission pattern as function of the distance between the mirrors, i.e. the voltage applied to the piezoelectric piece (Figure 5.3 Left). The theory behind the transmission was explained at section 3.3.3. The power has been measured before and after the air-spaced etalon resulting on a transmission maximum of ≈70%.

From the transmission pattern the linearity of the voltage ramp can be studied. As can be observed at Figure 5.3 Left, the separation between the centroids of following resonances is not constant at the voltage scan due to the non-linearity of the voltage ramp. Therefore, when a large number of scans are performed with different resonance positions, the peak separation can be plotted against the voltage (Figure 5.3 Rigth). The minimal peak separation will be related with the fastest scan speed, and therefore, at the voltage range where the separation stays constant, the scan speed will be constant as well.

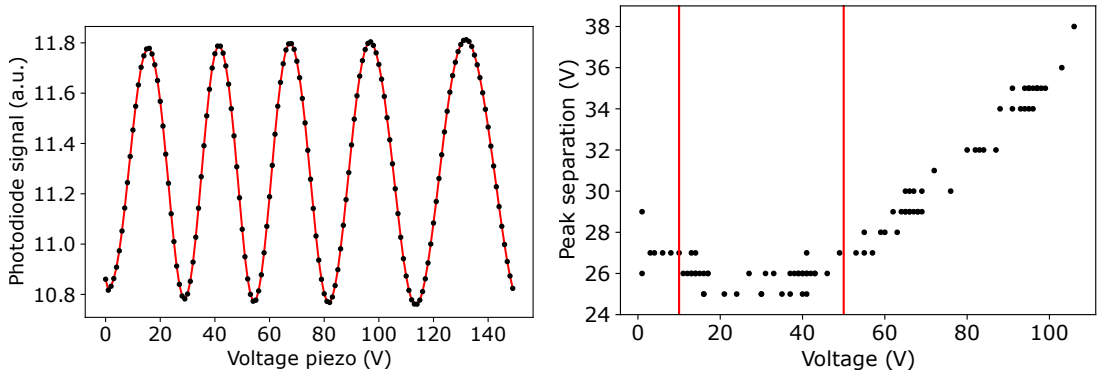

Figure 5.3: *Left) Transmission pattern of the Helium-Neon laser as function of the voltage applied to the piezoelectric piece. Right: Air-spaced etalon transmission peak separation versus voltage applied. The red lines represent the boundaries of the linear region.*

During operation, the air-spaced etalon will be used during long periods, being one of the key points the power stability. As a result, a power stability test was performed monitoring the power and temperature of the room during two 2 hours. The power has been monitored by the photodiode and the temperature by a thermocouple located adobe the air-spaced etalon mount. In addition, the voltage applied to the piezoelectric piece was fixed during that period. The power and temperature recorded at the test are plotted at Figure 5.4.

As can be observed at Figure 5.4, both pictures show a similar oscillation pattern which suggest that the instabilities of the measurement can be related with a temperature dependent power. Figure 5.5 confirms that the oscillations on power

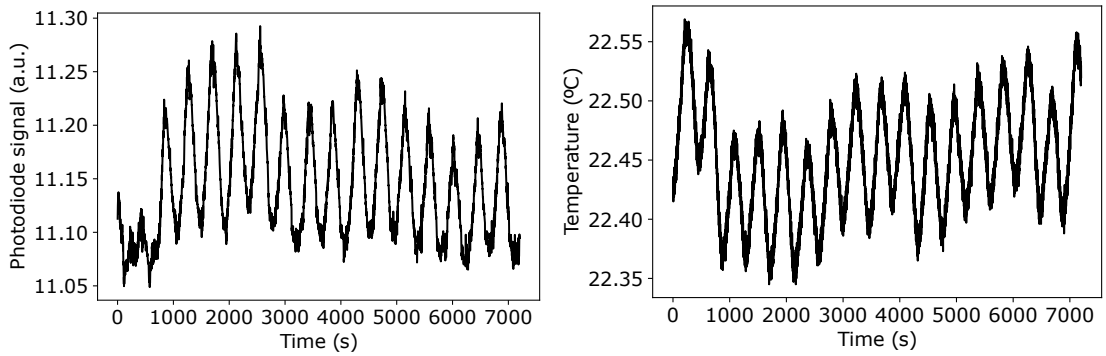

Figure 5.4: *Air-spaced etalon stability test. Left: Hene laser power measured by the photodiode versus time. Right: Thermocouple recorded temperature versus time.*

are related with the evolution of the temperature in the room, and therefore, the oscillation are probably due to the air conditioning cycle.

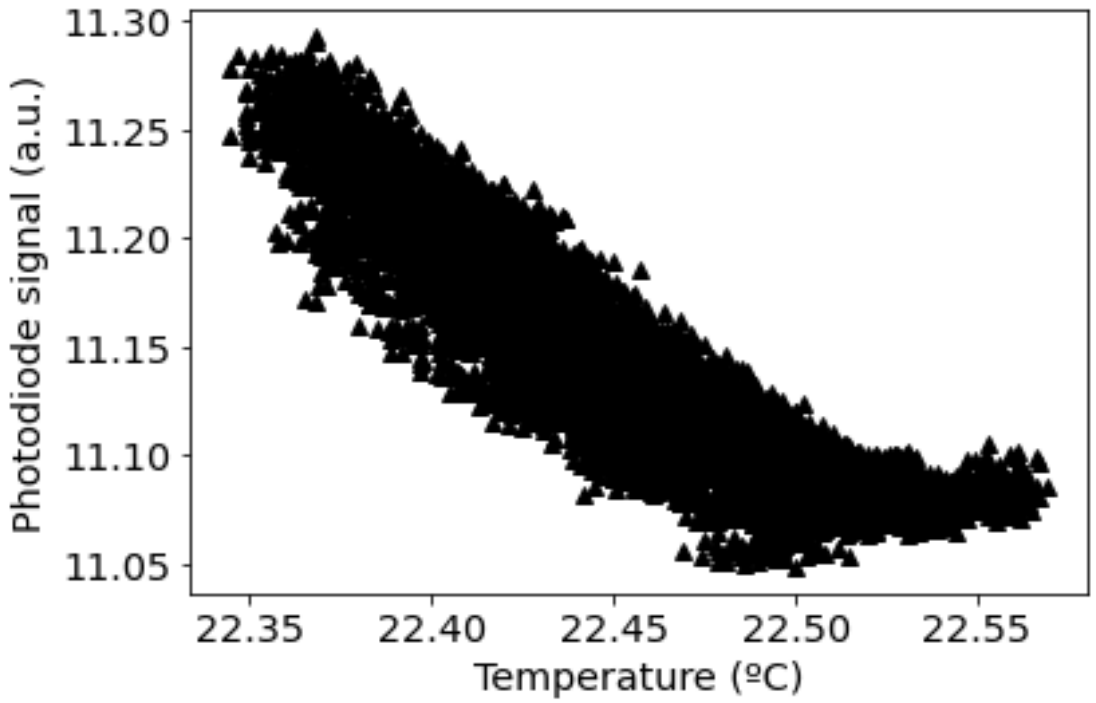

Figure 5.5: *Power during the air-spaced etalon stability test as function of the room temperature.*

5.1.2 Ti:sapphire cavity tests

The performance of the air-spaced etalon as a wavelength selective element has been studied on a Ti:sa cavity. As the purpose of the air-spaced etalon is to study if it can replace the thick solid etalon, the operation of both etalons will be compared.

The Ti:sa cavity used is presented at Figure 5.6. Consist on a Z cavity with a thin etalon and a BRF before the output coupler and the air-spaced etalon or thick solid etalon before the high reflective mirror.

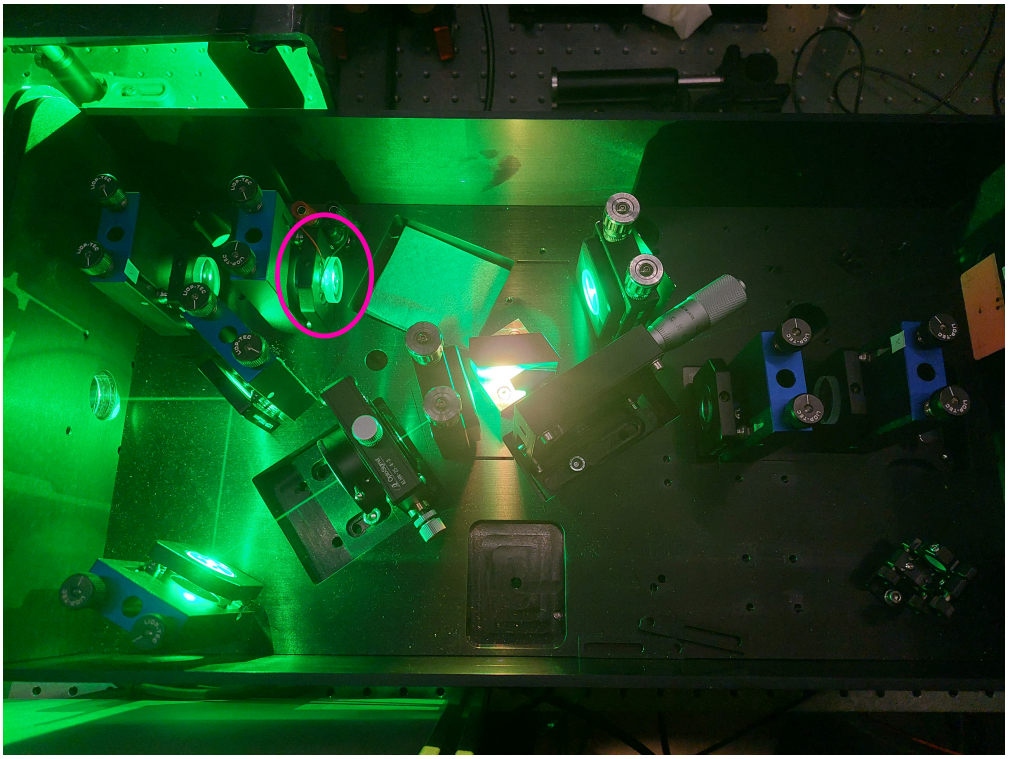

Figure 5.6: *Ti:sapphire cavity configuration for testing the air spaced etalon. The pink circle surrounds the air-spaced etalon.*

The frequency range of the air-spaced etalon and solid etalon has been studied. During this test, the thin etalon (broad wavelength selection) has not been manipulated, as a result the scan will be performed over the wavelength range selected by the thin etalon. The purpose of this test is verify the power loss of the solid etalon, and study if there is power loss on the air-spaced etalon.

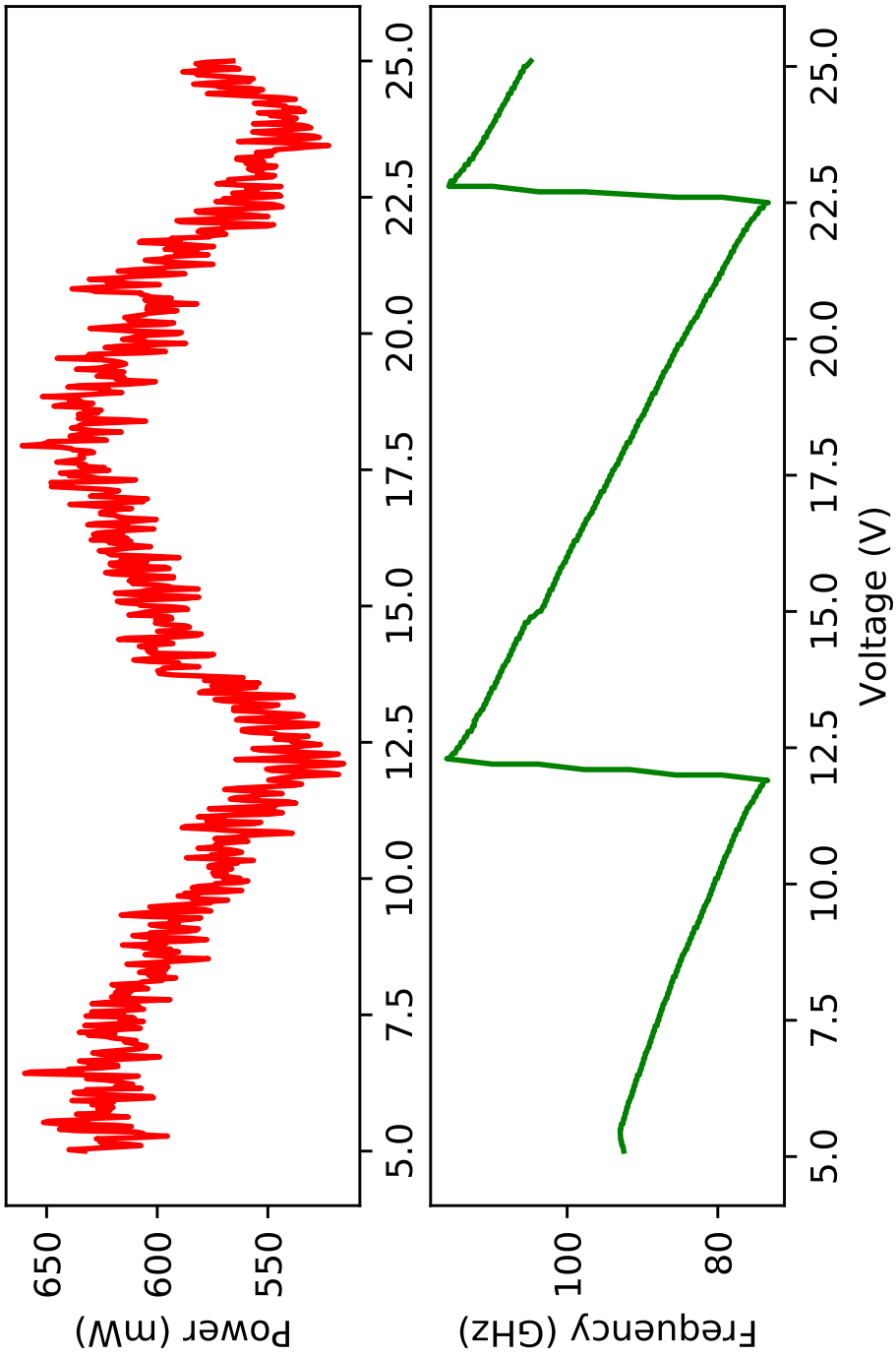

Figure 5.7: *Voltage apply to the air spaced etalon versus frequency and laser power.*

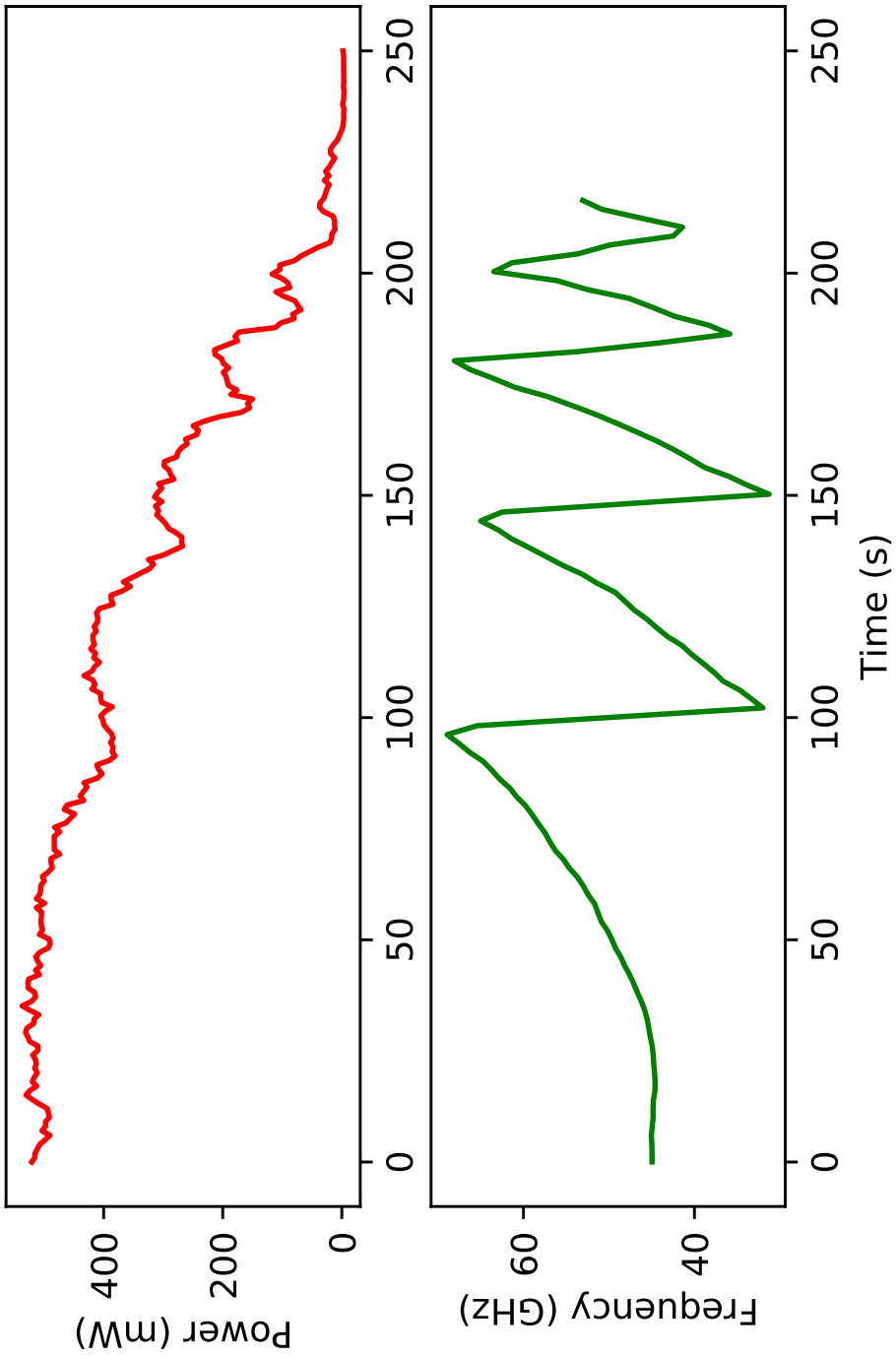

Figure 5.8: *Time (manual scan of the solid etalon angle respect the incoming beam) versus wavelength and power*

The voltage of the air-space etalon has been scanned on its linear region. Similarly, the solid etalon frequency range has been scanned changing manually the incident angle of the incoming beam using one of the mount screws. As the screws were not motorised, the scan has been performed over time. During this scans the laser power of the cavity has been monitored. The results of this measurement are shown at Figure 5.7 and Figure 5.8 for the air-spaced and solid etalon, respectively.

As can be observed at Figure 5.7 and Figure 5.8, the frequency scan is performed repeatedly over the same wavelength range, being the different modes selected by the BRF and thin etalon. The jump on wavelenth is related with a change of mode, covering each mode the same wavelength range. The frequency range covered is of 42.7 GHz for the air spaced etalon and 37.7 GHz for the solid etalon, before jumping mode.

Figure 5.8 shows how during long scans using the solid etalon the power drops as a result of the extra path. In contrast, Figure 5.7 do not show any indication of power decrease. However, as the number of modes covered by the air-spaced etalon is smaller than the number of modes covered by the solid etalon, there is not enough information to establish that there is no power loss on the air-spaced etalon.

In addition, the oscillation on the power at the air-spaced etalon scan is probably related to a most favorable power emission of the cavity on the center of the laser mode, and competition between the modes before and after jumping from one to the following mode.

In order to avoid this phenomena, the same measurement has been performed, but this time, adjusting the position of the thin etalon to avoid jumping from one laser mode to another, achieving a larger frequency range and a better performance of the cavity.

Figure 5.9 and Figure 5.10 show the results of this measurement for the air-spaced and solid etalon, respectively. The non-linearities on the frequency scan at Figure 5.9 are related to mode corrections after jumping mode due to difficulties when adjusting the thin etalon.

The full frequency scanning range has been of $\approx$100 GHz for the solid and $\approx$175 GHz for the air-spaced etalon. The limiting factor for the air-spaced etalon is the range of the piezoelectric piece, 3 μm on 150 V. In contrast, the limiting factor of the solid etalon is the power loss.

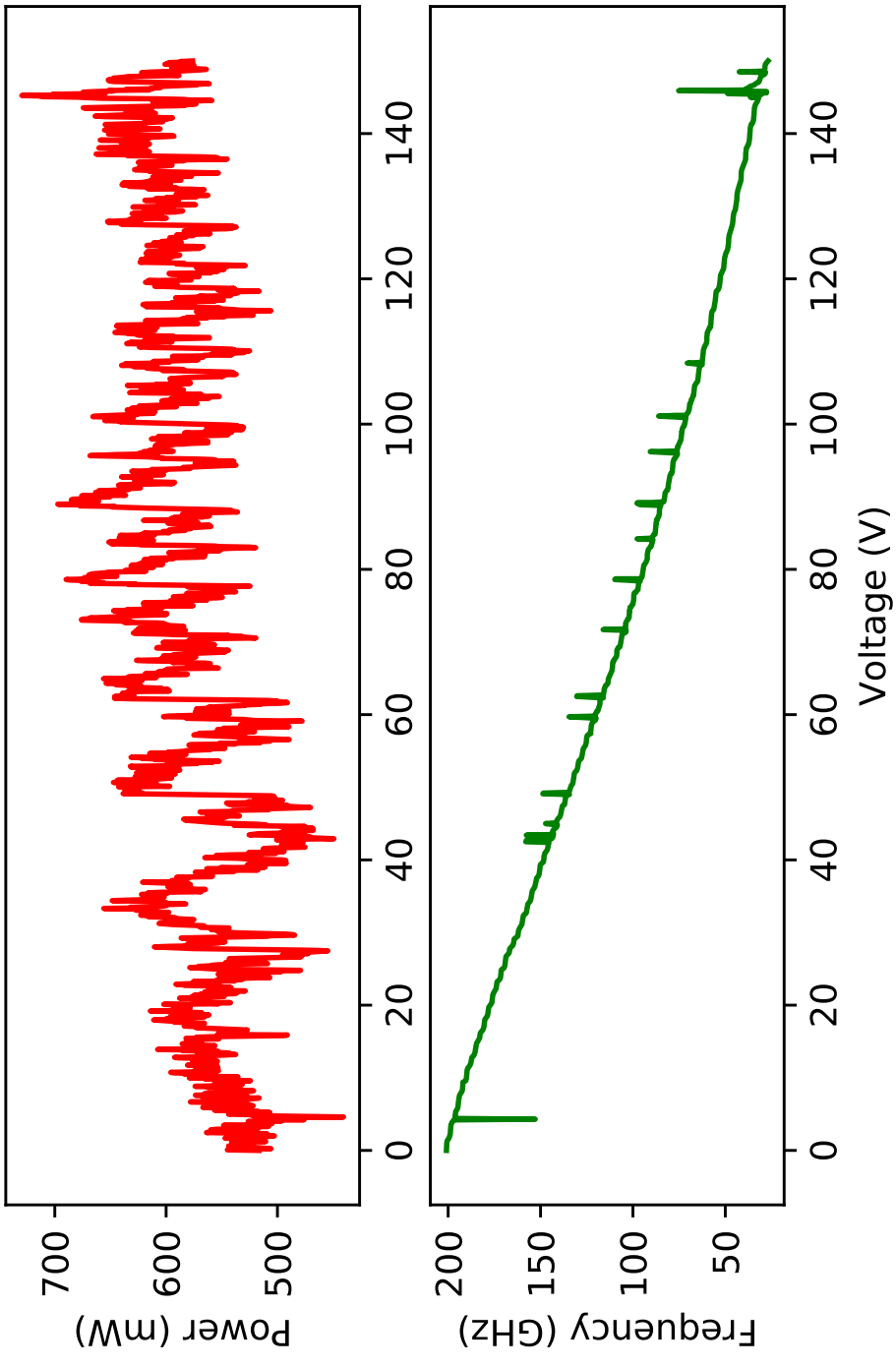

Figure 5.9: *Voltage apply to the air spaced etalon vs frequency and output power. The thin etalon has been optimized for each voltage.*

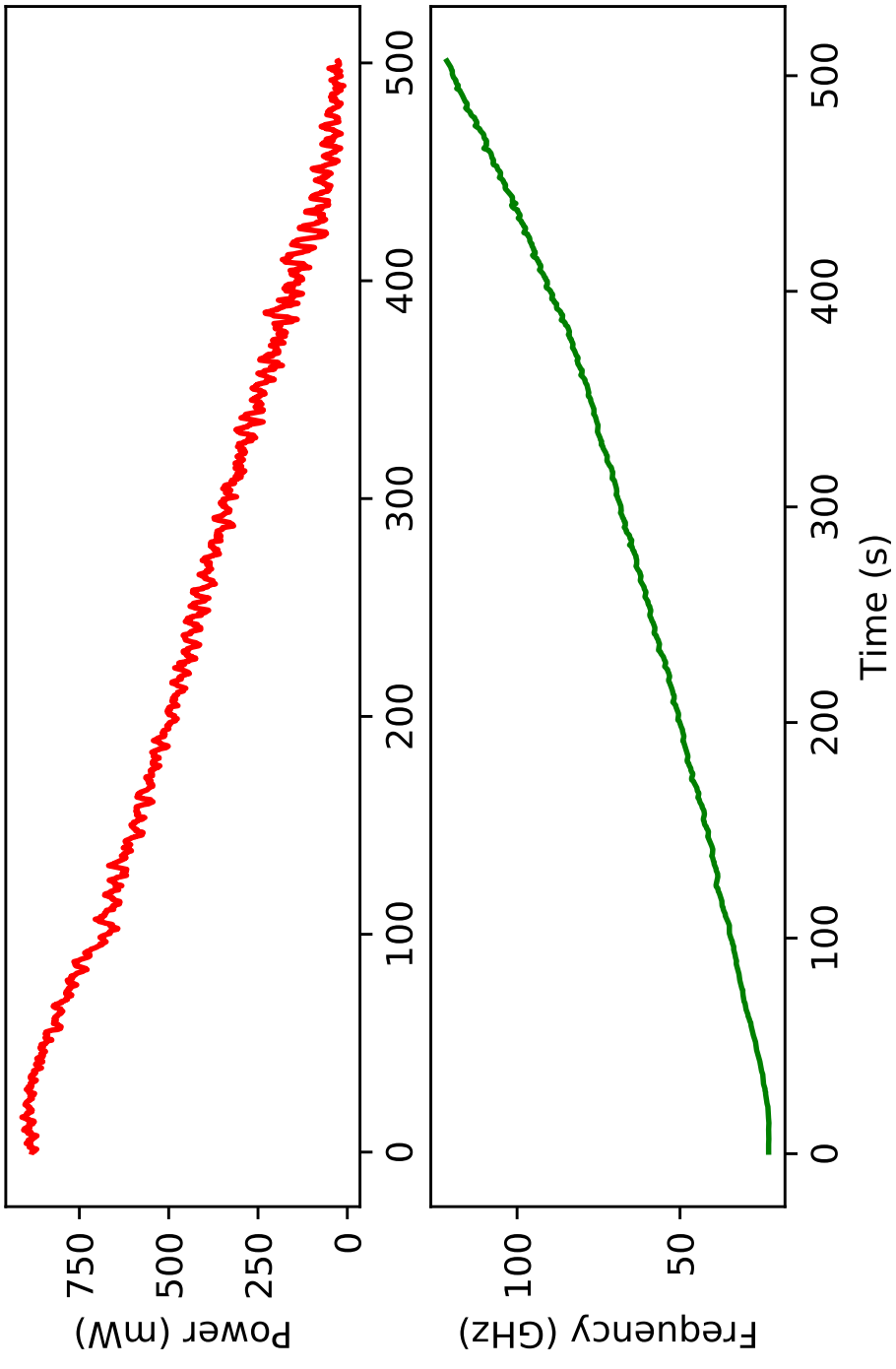

Figure 5.10: *Time (turning the solid etalon) vs wavelength and output power. The thin etalon has been optimized for each solid etalon position.*

As can be observed at Figure 5.10, the power decreases as function of the frequency for the solid etalon, while these two parameters are uncorrelated for the air-spaced etalon as is shown at Figure 5.9.

Additionally to the stability test performed at subsection 5.1.1, a new stability test has been performed to study the stability of the wavelength. The duration of this measurement have been of eight hours. The results for the solid and air-spaced etalon are shown at Figure 5.11 and Figure 5.12, respectively. During the stability measurement for the air-spaced etalon the temperature was also recorded to study its effect on the frequency, the result is presented at Figure 5.13.

The maximum deviation on frequency is ≈1 GHz for the solid etalon compared with ≈5 GHz for the air-spaced etalon. As a result, the behavior of the air-spaced etalon is much more unstable regarding frequency. From Figure 5.13 can be deduce that the instability is not related with temperature changes.

As the piezoelectric piece allows to a fast response, the wavelength can be controlled adjusting the voltage during the measurements. A simple code was written in python for this purpose and used to keep the wavelength stable within a 100 MHz range during a two hours stability measurement. This measurement is presented at Figure 5.14.

The last parameter studied during these test has been the linewidth of the laser beam provided by the cavity. This study has been performed using a home-made FPI free Spectral Range (FSR) of 3.46571(5) GHz [125] using a stabilised Hene laser as reference.

The single mode stabilised Hene laser is used to calibrate the spectra as the separation between two consecutive resonances is the FSR. The mode structure of the Ti:sa beam is therefore fitting using a Gaussian profile, being the FWHM of the Gaussian the linewidth of the laser.

The measured multi-mode paterns for the air-spaced and solid etalon are presented at Figure 5.15 (a) and (b), respectively. The linewidth of the air-spaced etalon and the solid has been og $\sim$ 1.15 GHz and $\sim$ 900 MHz, respectively.

However, it has been found that the 900 MHz linewidth of the solid etalon is uniquely at optimal conditions. Similarly as the power loss, the linewidth of the etalon is affected by the extra path. The measurement of the wavelength has been repeated reducing the output power by changing the angle of incidence. The solid etalon resulting linewidth has been ∼950 MHz and ∼1.4 GHz for half and a quarter of the total power, respectively.

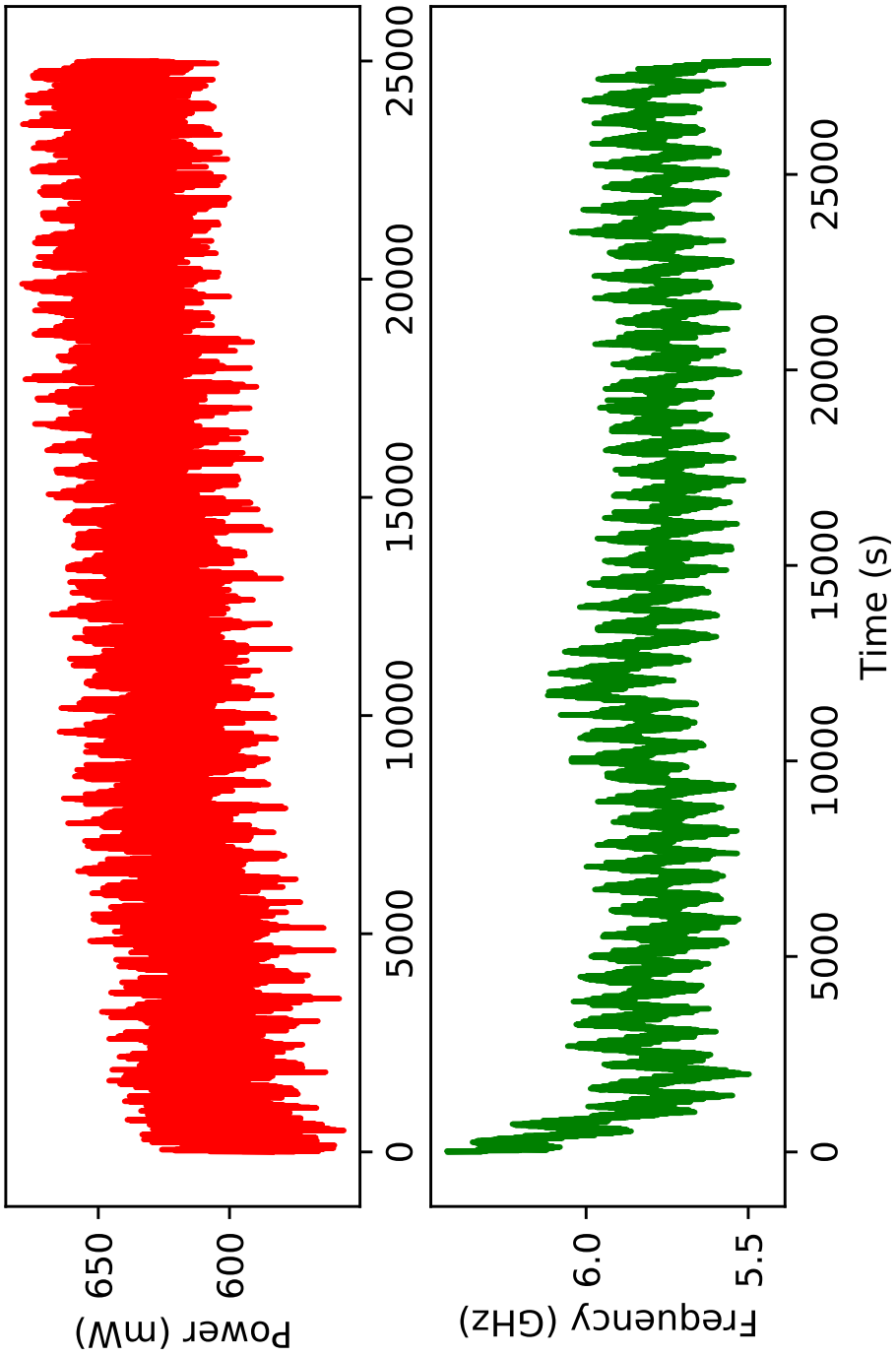

Figure 5.11: *Stability measurement of the solid etalon on a Ti:sa cavity. The graphic presents the power and wavelength variation as function of time.*

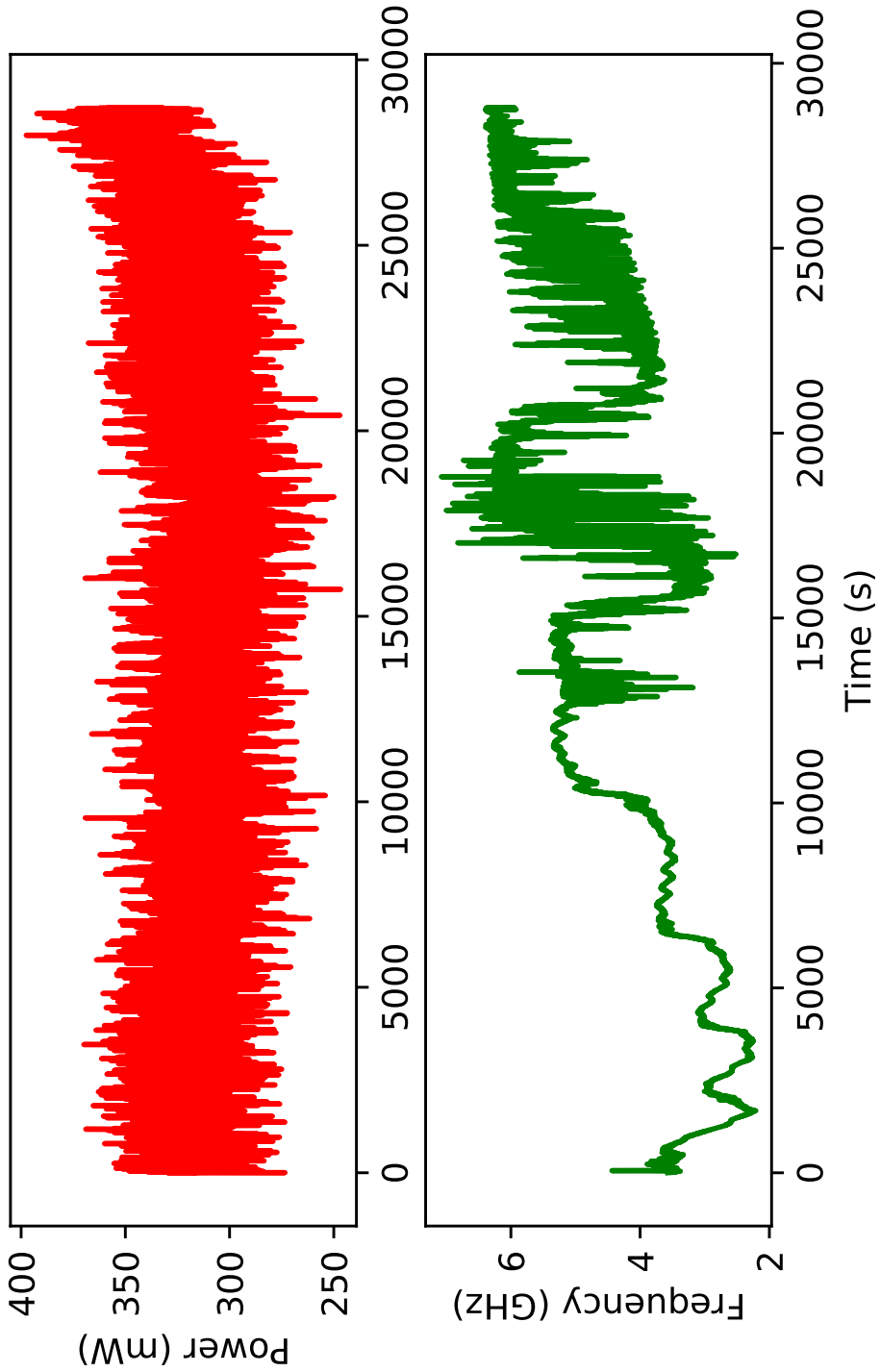

Figure 5.12: *Stability measurement of the air-spaced etalon on a Ti:sa cavity. The graphic presents the power and wavelength variation as function of time.*

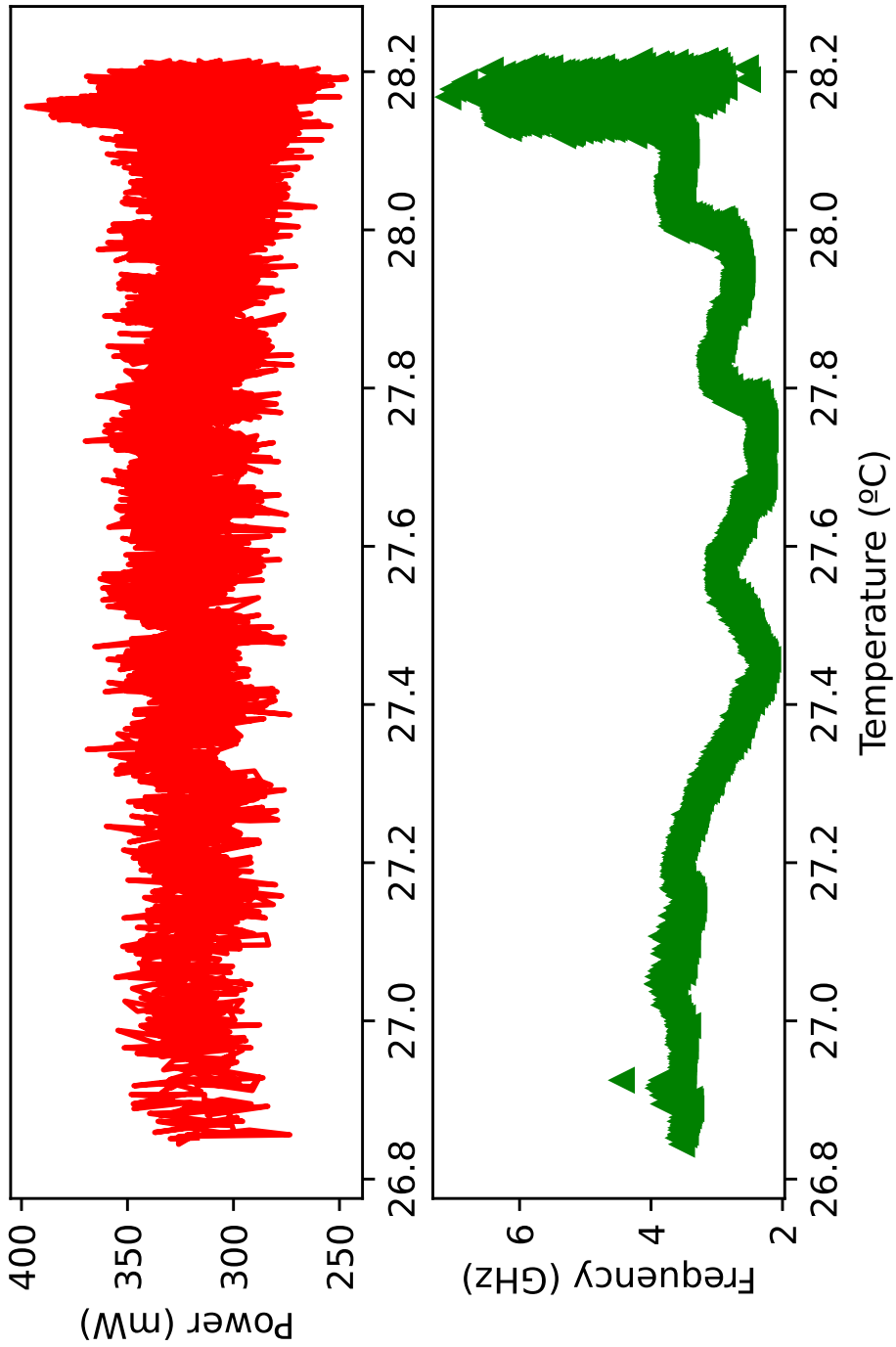

Figure 5.13: *Stability measurement respect temperature of the air-spaced etalon on a Ti:sa cavity. The graphic presents the power and wavelength variation as function of the room temperature.*

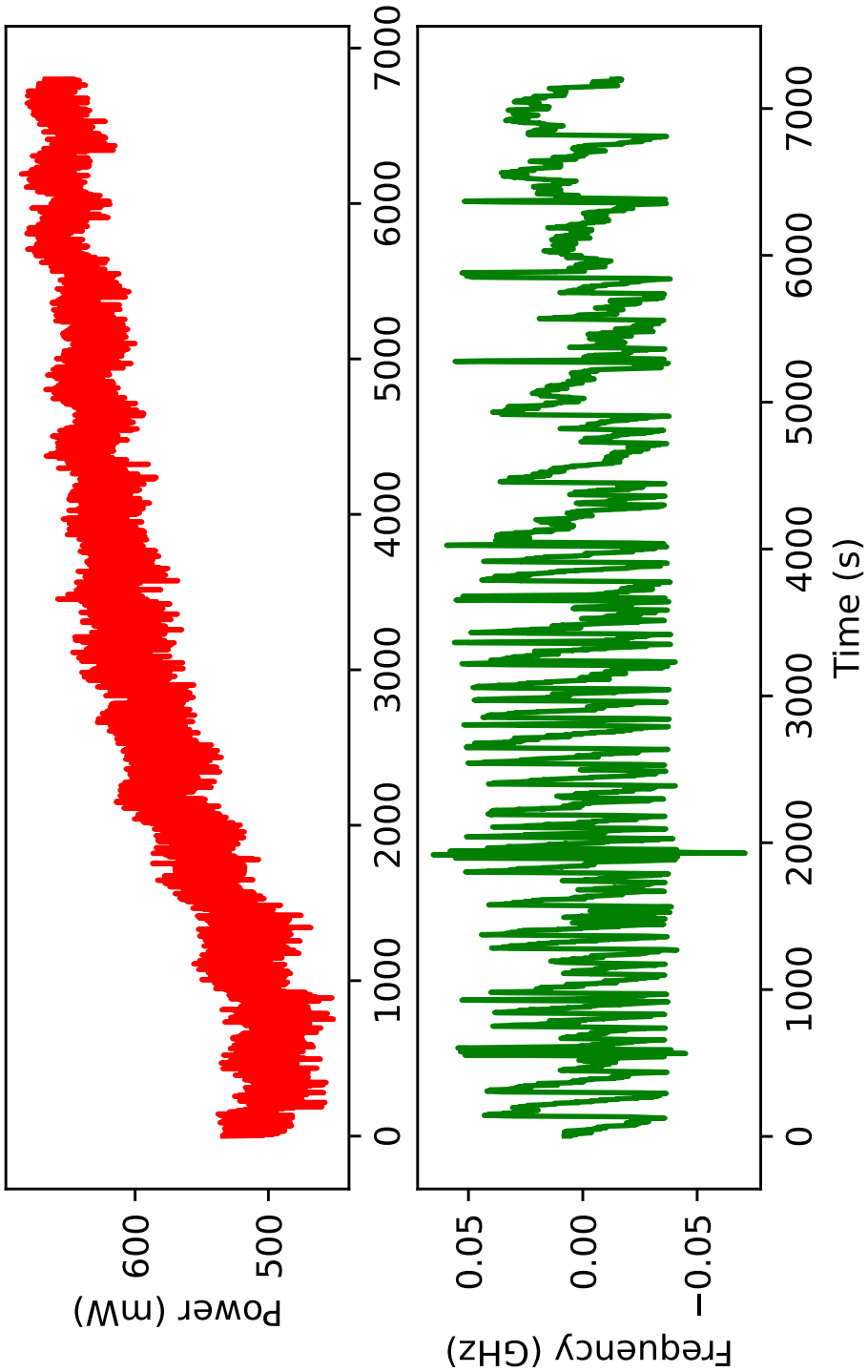

Figure 5.14: *Power and wavelength variation versus time for the air-spaced etalon with the stabilisation code.*

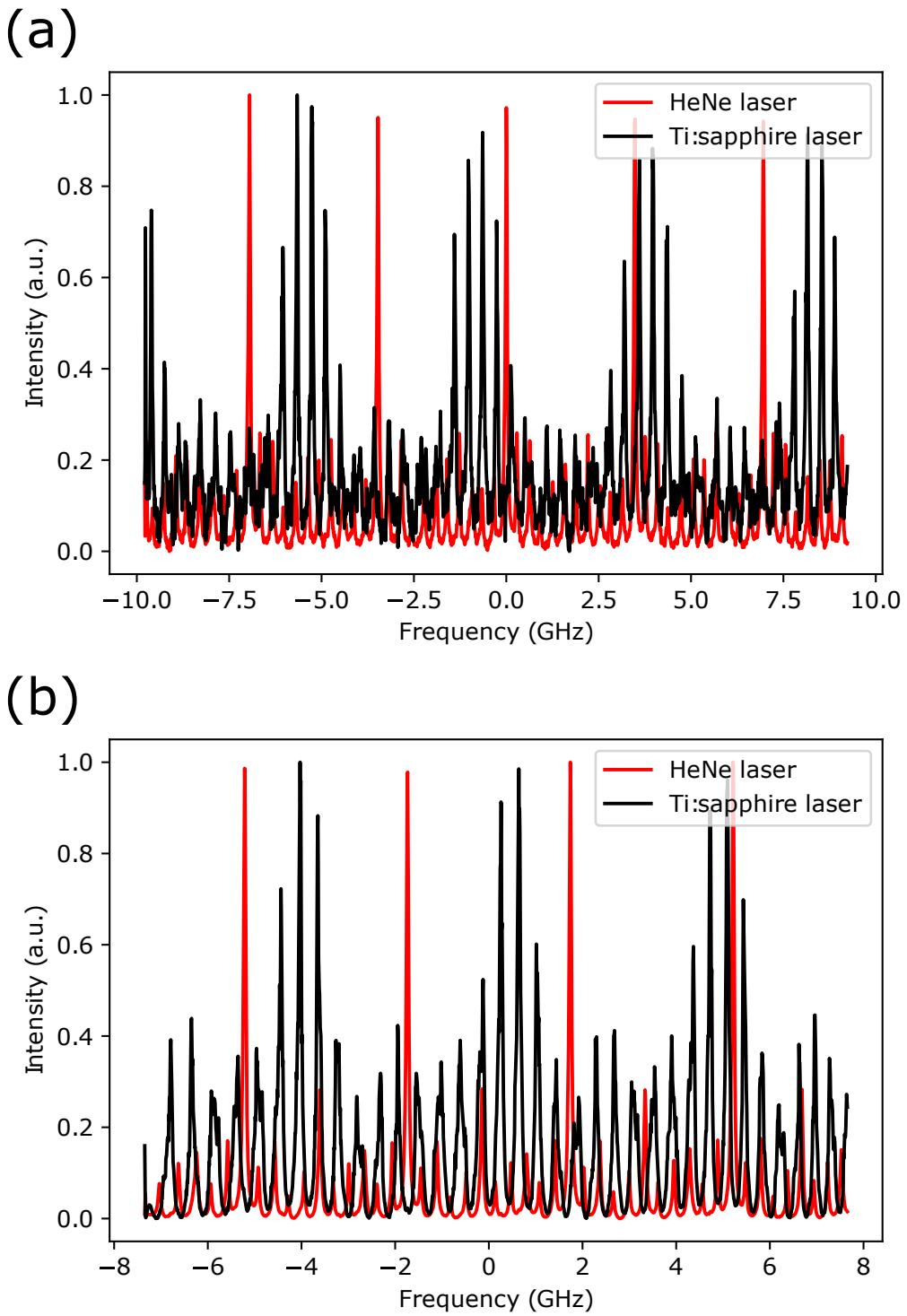

Figure 5.15: *Multi-mode structure of the dual etalon Ti:sapphire laser with an air-spaced etalon (a) and solid etalon (b). Mode patern of the Ti:sa cavity (black) and resonances of the HeNe laser (red). The x-axis is Piezo voltage scan of the Fabry-Pérot interferometer and the y-axis is the measured laser intensity of a photodiode located at after the FPI.*

5.1.3 Offline hot cavity laser spectroscopy Pd measurement

The air-spaced etalon has been used to perform a offline measurement of a sample of ^{106}Pd using the FURIOS setup [126]. The RIS scheme used to selectively ionize palladium is a three step ionization scheme developed by Mainz [127] and is presented at Figure 5.16.

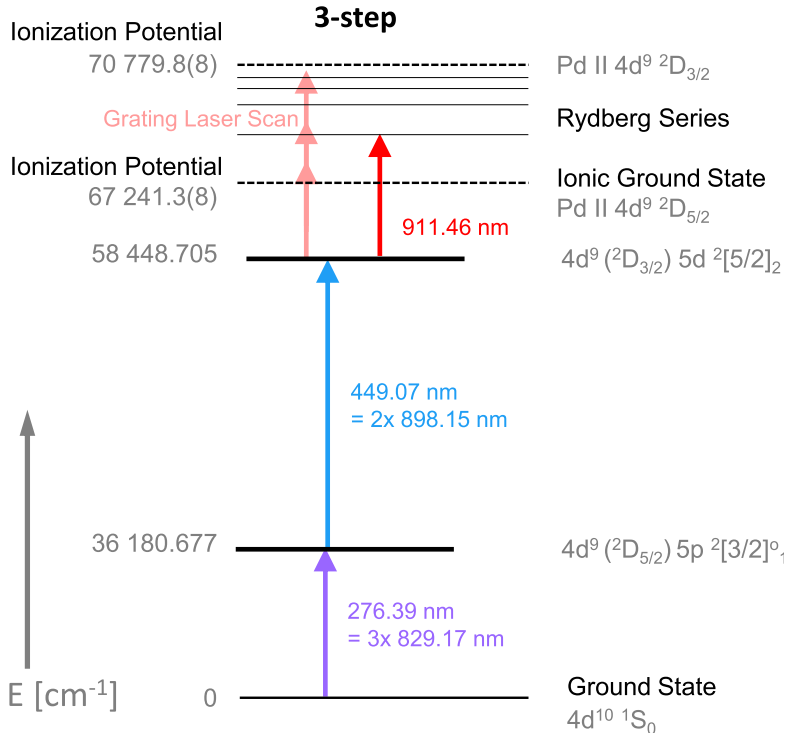

Figure 5.16: *Three step ionization scheme used during the measurement [127].*

The air spaced etalon has been placed inside the Z-cavity Ti:sapphire laser with intra-cavity second harmonic generation and extra-cavity third harmonic generation to produce the first step. The fundamental laser wavelength was center at 827.17 nm, resulting on 276.39 nm after the third harmonic generation.

The scanning range during the measurement was ≈14.5 GHz. In order to synchronize the scan steps and the data acquisition a python software was written to integrate the air-spaced etalon software into the FURIUS epics controlling system.

The frequency spectra of the ^{106}Pd offline hot cavity laser spectroscopy measure-

ment with the air-spaced etalon at saturation power are presented at Figure 5.17. The measured FWHM of the resonance is 4.46(3) GHz. Assuming that there are not broadening effects involved on the measurement, and taken into account the third harmonic generation, the fundamental linewidth of the Ti:sapphire should be ≈1.5 GHz, which is in agreement with the previous FPI measurements.

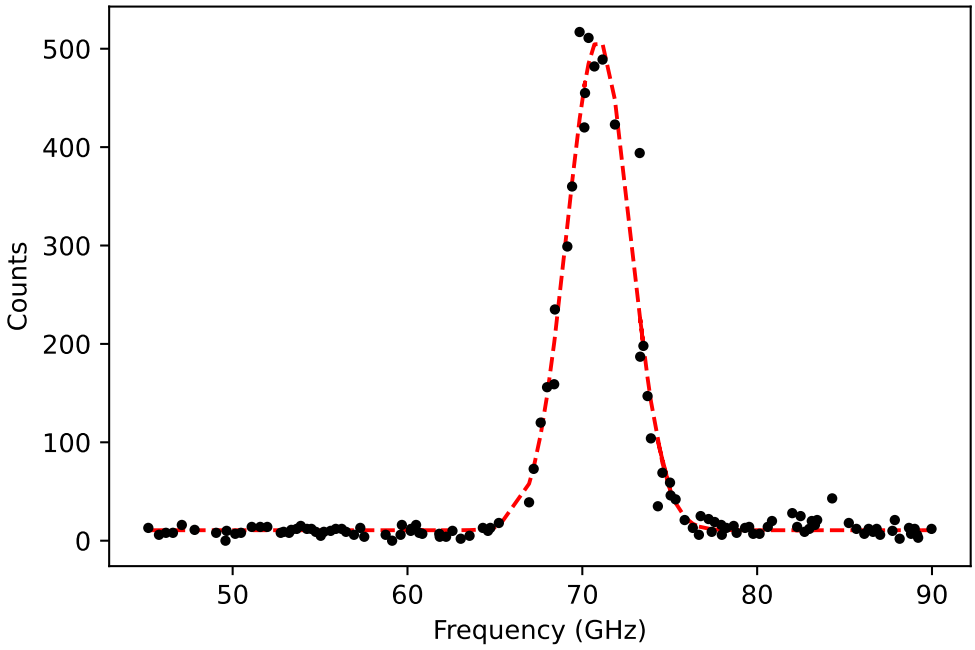

Figure 5.17: *Frequency spectra of the hot cavity measurement with the air spaced etalon. The dashed red line represent the gaussian fit of the data.*

5.2 Scanning Fabry-Pérot interferometer (sFPI)

Laser frequency determination is a basic need when performing a laser spectroscopy measurements. Uncertainties on this value will propagate to the results on the extracted observables. On offline measurements, this accuracy becomes even more important due to the high resolution expected when performing reference measurements. However, high resolution wavemeters able to perform wavelength determination with accuracy bellow 50 MHz can cost ≈42 k€.

During this section, the possibility of using a Scanning Fabry-Pérot Interferometer

(sFPI) as an alternative device for wavelength determination will be explored.

As the etalon, the FPI is composed by two highly reflecting mirrors facing each other, being one of them movable. If the mirror is constantly moving the device is called interferometer due to the interference patterns resulting from the multiple reflected beams being superimposed. The interference pattern is shown at Figure 3.11.

As was discussed at section 3.3.3, the transmission through the FPI is dependent on the wavelength of the laser and the length of the FPI, being a transmission maximum whenever the optical path length is a multiple of the wavelength. As a result, if the wavelength of the laser changes, the position of the maximum will also change.

The position of the fringes can be tracked combining Ti:sapphire (Ti:sa) and Helium–neon (Hene) lasers [128]. The Hene laser is used to calibrate on frequency the FPI spectra. The separation between two consecutive Hene fringes will be the FSR of the FPI (tipically 1 GHz). As the separation between the peaks is dependent on the laser frequency, the frequency spectra has to be calibrated to the Ti:sa laser frequency.

$$FSR_{Ti:sa} = FSR_{Hene}\frac{\nu_{Ti:sa}}{\nu_{Hene}} \tag{5.1}$$

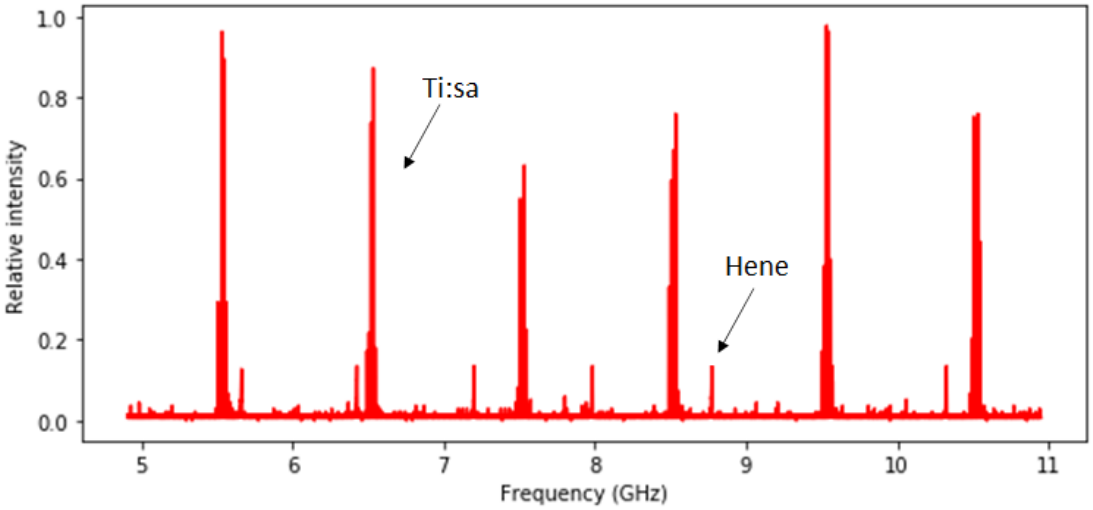

Figure 5.18: *FPI spectra calibrated to the Ti:sapphire frequency.*

Once the frequency is calibrated, the Ti:sapphire laser frequency changes can be accurately measured, as the position of the fringe will move on the same value. In addition, as the Helium:neon laser has a constant and well defined wavelength, it can be used as a reference to avoid systematic errors. Any change on the position of the fringes due to the room conditions and not due to wavelength changes will also affect the Hene fringes position.

Even if this method allow to accurately measure changes on the wavelength, it is not possible to determine the real wavelength of the laser. However, as laser spectroscopy are relative measurement it is possible to extract isotope shifts and hyperfine parameters.

In order to test this system, a sFPI has been install at the GISELE offline laboratory and has been used to measure the isotope shift between ^{116}Sn and ^{120}Sn on the 811 nm transition of the three step scheme presented at Figure 5.19.

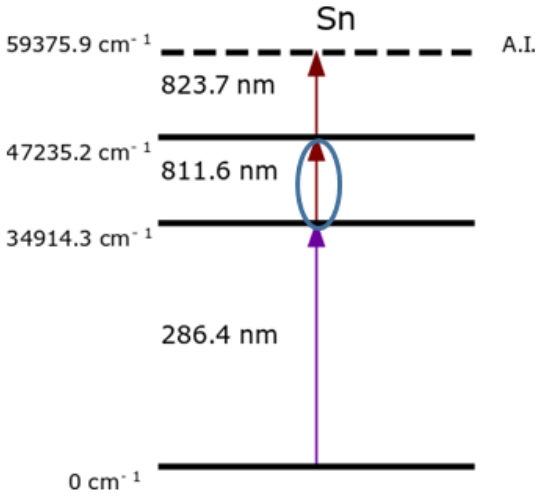

Figure 5.19: *Three step ionization scheme used to measure Sn. This scheme was used at JYFL for Thomas Kessler PhD thesis [129].*

During the measurement, the wavelength has been determined by the sFPI and the WS7 wavemeter, which has 30 MHz accuracy. The comparison between both is presented at Figure 5.20.

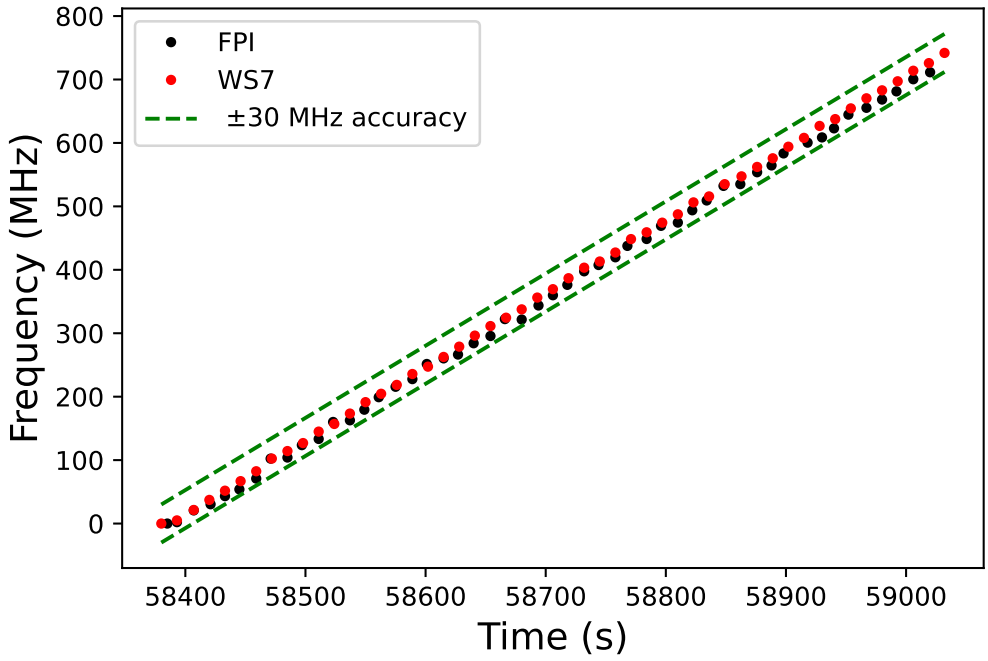

Figure 5.20: *Comparison of the wavelength measurement of the sFPI and a WS7 wavemeter with 30 MHz accuracy.*

As can be shown at Figure 5.20, the wavelength determination using the sFPI is in agreement with the WS7 wavemeter within its 30 MHz accuracy. The resulting frequency spectra are shown at Figure 5.21. The isotope shift extracted from this measurement is 183(5) MHz using the sFPI, with is in agreement with the 185(5) MHz obtained using the WS7.

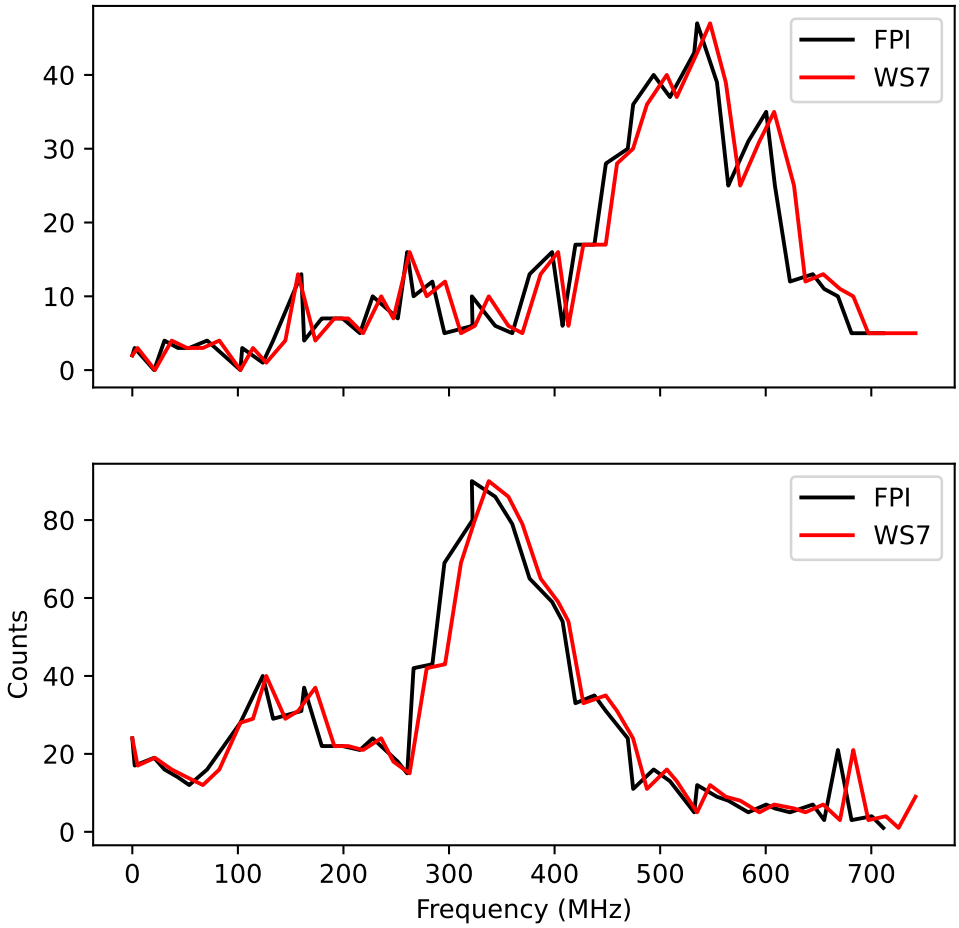

Figure 5.21: *Comparison of the frequency spectra of ^{116}Sn and ^{120}Sn, using the sFPI and a WS7 wavemeter to determine the laser frequency.*

Chapter 6

Fluorescence laser spectroscopy on Pd

At this chapter will be discussed the analysis of two collinear laser spectroscopy experiments performed at the IGISOL facility at the University of Jyväskylä (see section 4.1). The first measurement focused on the neutron rich side, measuring the palladium isotopes $^{112-116,118}$Pd. The second measurement obtained data from the neutron deficient palladium isotopes $^{98-101}$Pd.

These measurements were supported by previous offline work on stable palladium [130]. During the offline work, stable ^{102}Pd was measured using transitions starting on different atomic meta-stable states. Between those transitions, $4d^9 5s\,^3D_3$ - $4d^9 5p\,^3P_2$ was found the most suitable for the online measurements performed at this work as it was the most efficient and also sensitive to the nuclear observables.

In laser spectroscopy the observables are not extracted as an absolute value, instead, are measured as a difference between the isotope of interest and a reference isotope. In order to avoid discrepancies due to changes on the experimental conditions during the measurements, the reference isotopes are measured during the online experiment. The reference isotope should then have high production yield and the observables measured with high accuracy. ^{108}Pd has been selected as the reference for the neutron rich isotopes and ^{102}Pd for the neutron deficient.

6.1 Data analysis

A ^{108}Pd stable even-even isotope data-set is going to be used to explain the data analysis procedure. As a reminder, ^{108}Pd frequency spectra will be composed by only one resonance due to its lack of hyperfine splitting ($I = 0$).

One of the characteristics of fluorescence collinear laser spectroscopy at IGISOL, unlike other kinds of laser spectroscopy measurements included on this thesis, is that the laser wavelength remain constant during the measurement. As has been mention at subsection 4.1.1, the parameter used to scan the frequency is the scanning voltage (V_s) applied before the CEC.

In order to avoid systematic errors due to a discrepancy on the voltage, the applied voltage is measured, for each scan step, before each scan and saved on a file. This file is used during the analysis to calibrate the voltage through a linear regression as is shown at Figure 6.1.

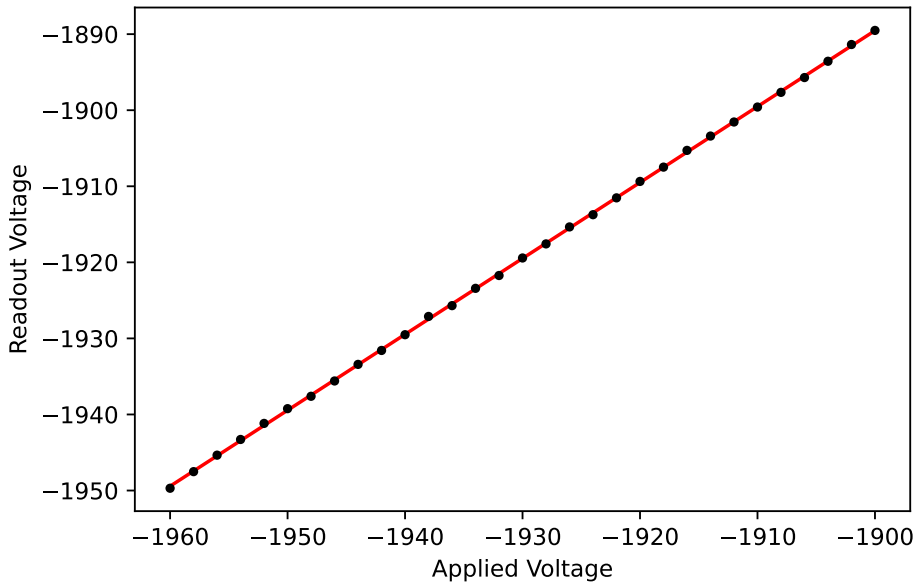

Figure 6.1: *Applied voltage versus readout voltage. Black dots are the data points and the red line is the linear regression* $V_{read} = 7.188 + 0.998 * V_{applied}$

The maximum discrepancy between the applied voltage and the readout value for this scan is 10.57 V (0.55 %). The calibration has a not negligible effect on the frequency centroid as will be shown in Table 6.1.

Table 6.1: *Comparison between peak position with and without calibration for one run of ^{108}Pd.*

	With calibration	Without calibration	Difference
Centroid position (MHz)	3006.05	3114.46	108.41

The scanning voltage is used to Doppler shifted the laser wavelength as an effect of the kinetic energy of the ion beam. The energy of the atoms at the moment of the interaction with the laser can be considered to be only related to the kinetic energy generated by the voltages after the cooler-buncher. The scanning voltage (V_s) has only a small influence to the total beam energy ($V_s \sim$ few V), being the main contribution the extraction potential of the cooler-buncher ($V_c \sim 30$ kV). In addition, it was observed in previous offline study the necessity to add an offset of 15.1(14) V to the cooler extraction voltage to obtain the real beam energy [110].

The observed laser frequency (ν) by the ions can be calculated using the Doppler effect (Equation. 6.1).

$$\nu = \nu_L(1 + \alpha + \sqrt{2\alpha + \alpha^2}) \qquad \alpha = \frac{QeV}{mc^2} \tag{6.1}$$

Being ν_L the atomic transition frequency and α the parameter which contains the information about the kinetic energy of an ion beam accelerated by an electric field. The contributors of this kinetic energy are Q, which is the charge of the ion (which in this case are single charge electrons), the total voltage $V = V_c + V_s$ and m being the mass of the ions.

Time gate

As has been introduced at section 3.4.1, when the observed laser frequency is equal to the transition frequency the atomic electron will excite and rapidly decay emitting a photon, which will be detected by a photomultiplier tube (PMT). Alongside the emitted photons, there is a background generated by scattered photons as can be shown at Figure 6.2.

Considering a 3σ criteria, a clear peak can not be observed at Figure 6.2 Right. In order to improve the signal-to-total ratio, bunched beam spectroscopy was developed at the early 2000 [108], combining laser spectroscopy with an RFQ cooler-buncher.

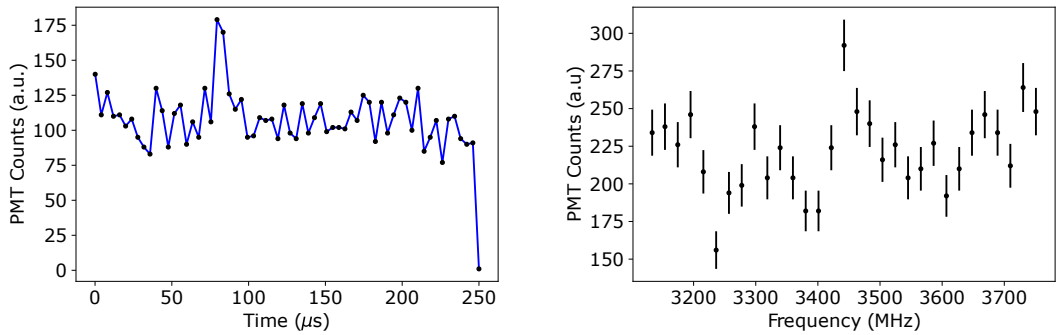

Figure 6.2: *Left: TOF versus PMT counts. Right: Frequency versus PMT counts.*

A time-of-flight (TOF) spectra between the extraction of the RFQ and the PMT can be generated during the period when the end-plate potential is open (∼250 μs) and the ions are injected into the collinear beamline. The TOF versus PMT detected photons spectra is mainly composed by a constant background generated by the scattered light. However, an increase of counts of ∼10-20 μs can be observed, related with the atomic bunch. The TOF between the extraction from the RFQ and the detection is dependent on the mass of the atoms. By restricting the frequency spectra to the atomic bunch using a TOF gate, the signal-to-total ratio can be greatly improved, as is shown at Figure. 6.3.

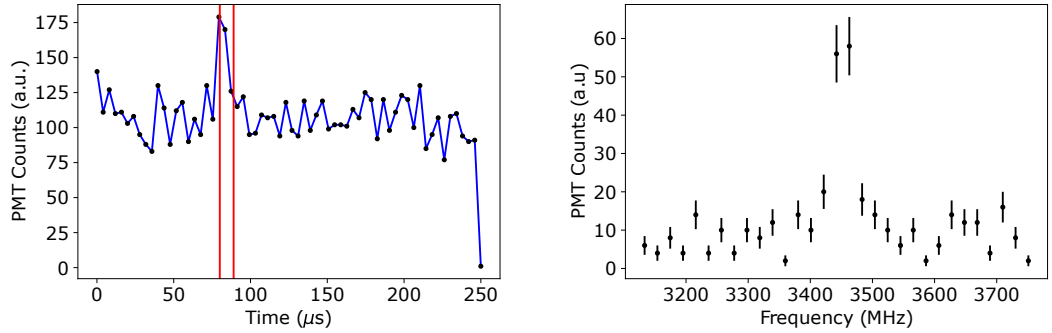

Figure 6.3: *Left: TOF versus PMT counts, the red lines represent the time gate boundaries. Right: Frequency versus PMT counts restricted to the TOF gate.*

An optimization of the signal-to-noise ratio can be performed studying the frequency distribution of different TOF selections inside the atomic bunch (Figure 6.4). Leading to a selection of a different TOF gate with improved signal-to-noise for each scan (Figure 6.5).

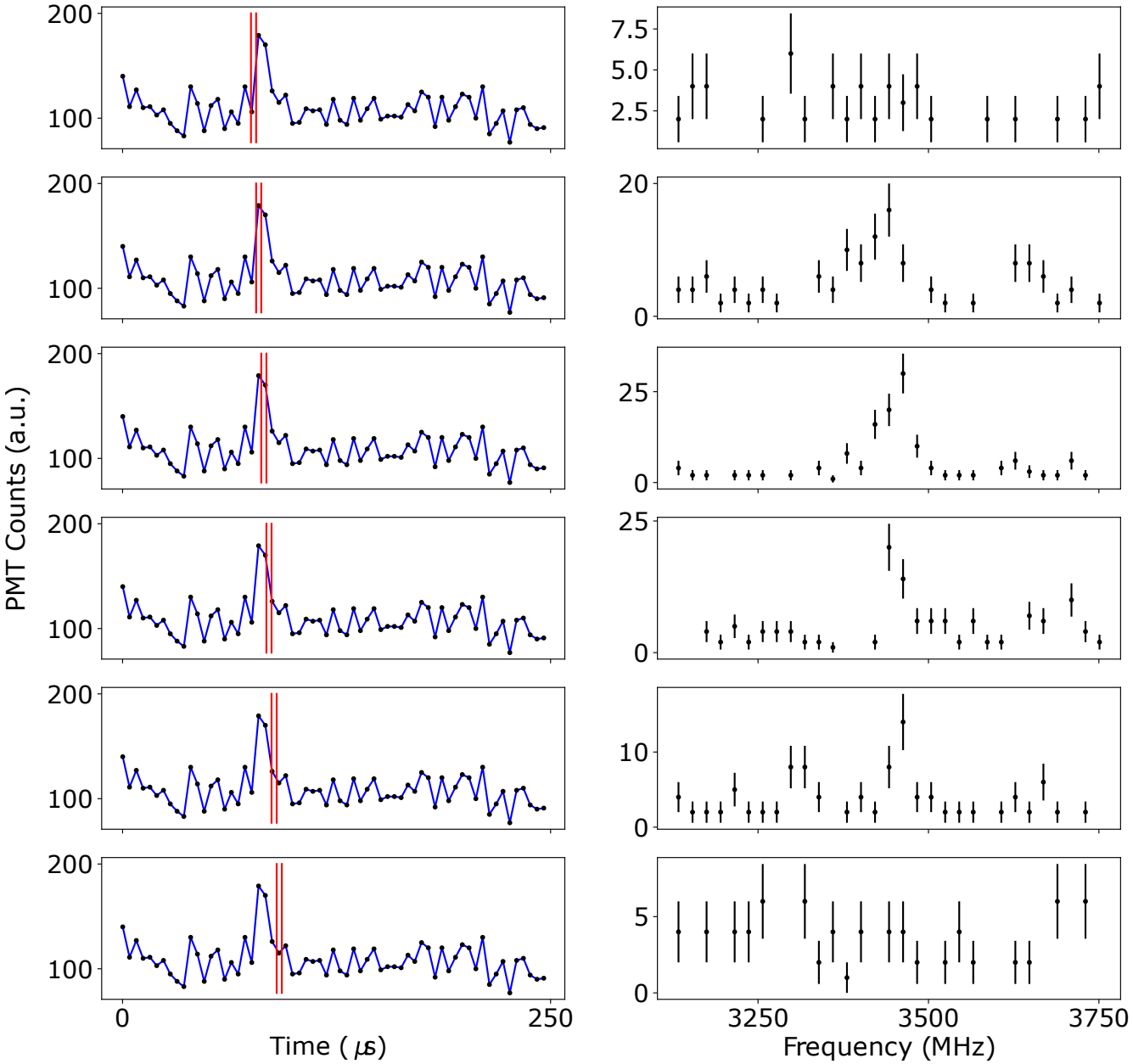

Figure 6.4: *Left: TOF versus PMT counts, the red lines represent the time gate boundaries for 6 different gates. Right: Frequency versus PMT counts restricted to the TOF gate for 6 different gates on the bunch.*

In this way, a better identification of the resonance transitions can be achieved, having an utmost important when dealing with isotopes with hyperfine splitting and/or low counting rate.

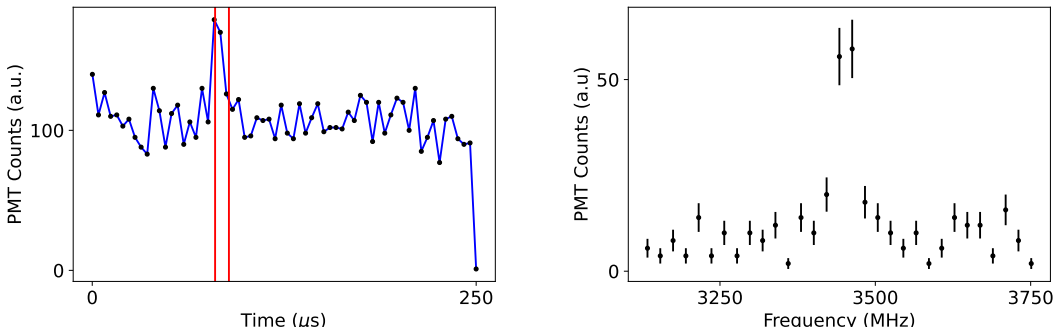

Figure 6.5: *Left: TOF versus PMT counts, the red lines represent the optimal time gate boundaries. Right: Frequency versus PMT counts restricted to the TOF gate which optimizes the signal-to-noise ratio.*

6.2 Even-A isotopes - Isotope shift analysis

Despite the even isotopes do not have hyperfine structure, the position of the resonance provides important information about the size of the nucleus. As has been shown at subsection 3.2.1, the difference in the resonance frequency between two isotopes is related with the change on the mean-square charge radii. At Figure 6.6 is shown clearly the evolution of the resonance frequency as increasing the mass.

6.2.1 Data handling and error calculation

For each scan the experimental data has been fitted using the SATLAS package [131], which is a specialised tool for analyzing low statistics data, tailored for laser spectroscopy experiments. Using this package, the resulting spectrum is fitted with a Voigt profile by a chi-square minimization fitting method. The centroid of the resonance has been calculated as the weighted mean of all individual measurements of each isotope.

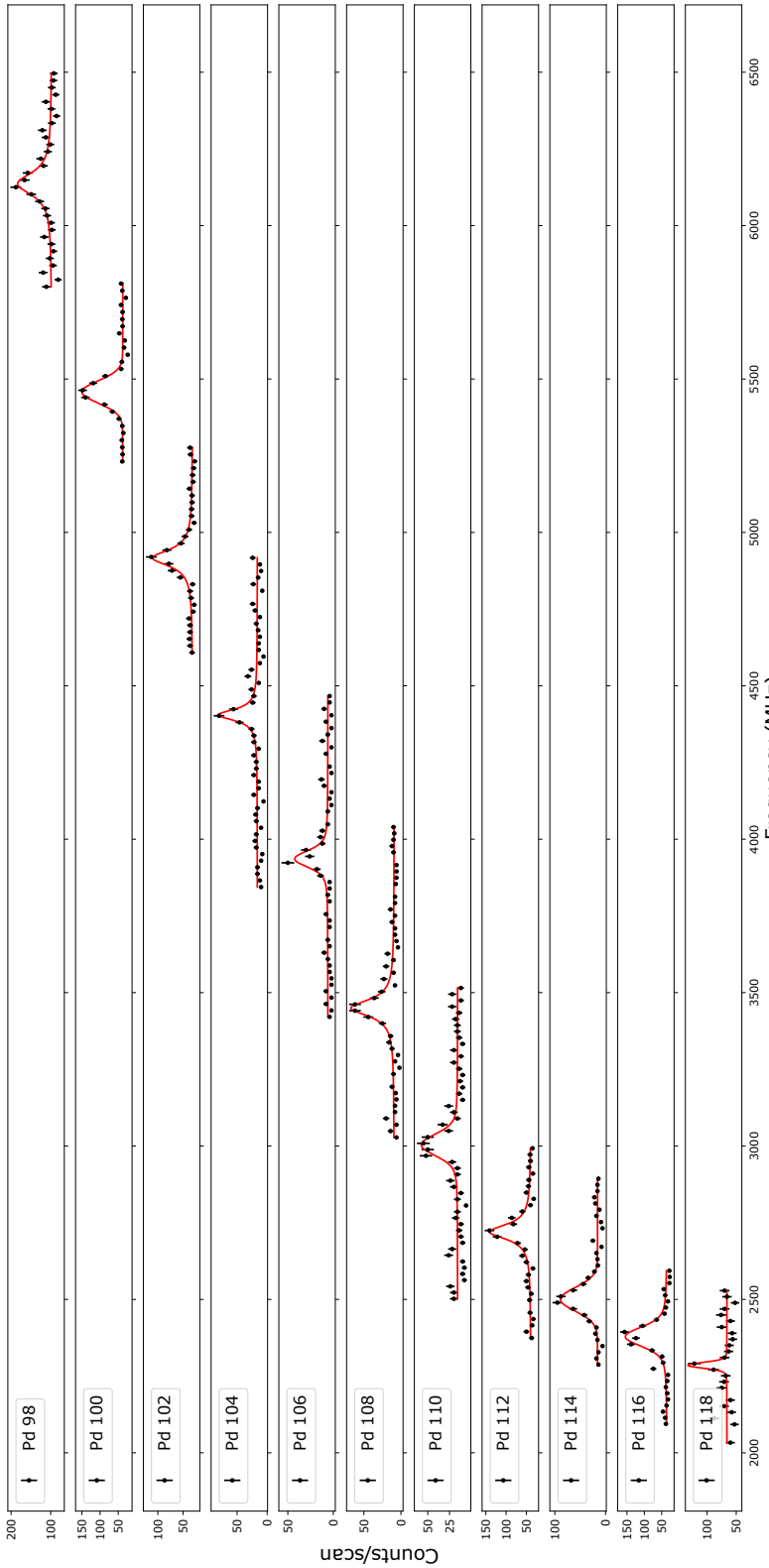

Figure 6.6: *Frequency spectra of even-A palladium isotopes.*

$$\bar{\nu} = \frac{1}{\sum_i^N \frac{1}{\sigma_i^2}} \frac{\nu_i}{\sigma_i^2} \tag{6.2}$$

being ν and σ the centroid and error of one of the N scans for one isotope, respectively. The statistical error σ is consider as the standard error of the SATLAS fit scaled with the reduced chi-square. Therefore, the error on the frequency centroid for an isotope is calculated considering a dispersion-corrected weighted mean:

$$\bar{\sigma}^2 = \frac{1}{\sum_i^N \frac{1}{\sigma_i^2}} \cdot \frac{1}{N-1} \sum_i^N \frac{(\nu_i - \bar{\nu})^2}{\sigma_i^2} \tag{6.3}$$

For some of the isotopes, the number of the scans was too low to assign reliable statistical uncertainties. For these cases, the statistical analysis has been performed using a bootstrapping algorithm [132]. This method is used when it is not possible to repeat a measurement several times. Instead, random samples of the total data simulating the action of repeating a experimental measurement many times in order to estimate the value of a parameter with a certain confidence interval. For an isotope, considering the data points taken from all the scans, the bootstrapping algorithm looks as follows:

1. Label the experimental data points from 0 to N.
2. Generate n random numbers between 0 and N.
3. Create a sample which contains the n data points whose label has been generated by the random numbers. This means the same data point can be selected several times.
4. Perform a Voigt profile fit using the sampled data points, and store the resulting fit parameters.
5. Repeat steps 2 to 4 a reasonable number of times. In this case, 5000 repetitions were performed.
6. Calculate the mean and variance of the fitting parameters using the stored values of the fit parameters.

This method actuates under the assumption that the experimental distribution obtained during the measurement is a representative of the true distribution. In

addition, in case that the experimental distribution contains outlier points which skews the distribution, these few points will get sampled infrequently. Therefore the parameter estimated from most of the bootstrap samples will not be skewed, making this method more robust than standard parameter estimation.

Besides the statistical error, there are two sources of systematic error on the extraction of the centroids. The first systematic error is on the wavemeter readout. From most of the isotopes is has been possible to measure their frequency spectra without changing the laser frequency stabilisation setpoint. However for some of the neutron rich isotopes, the difference between the setpoint and the resonance frequency was too large, resulting on a change of setpoint. As the wavelength changed, a fixed 10 MHz error has been included taken from the specification of the wavemeter according to a 3σ criteria.

The second systematic error is coming from the uncertainties on the determination of the RFQ cooler-buncher voltage and tuning voltage. Using Equation 6.4 [133] the uncertainties on the voltage can be propagated to errors on the isotope shift:

$$\Delta_{sys}(\delta\nu^{A_{ref},A}) = \nu_L\sqrt{\frac{eV_{RFQ}}{2m_{ref}c^2}}\,[\frac{1}{2}(\frac{\delta V_{LCR}}{V_{RFQ}}+\frac{\delta m}{m_{ref}})\frac{\Delta V_{RFQ}}{V_{RFQ}}+\frac{\delta V_{LCR}}{V_{RFQ}}\frac{\Delta\delta V_{LCR}}{\delta V_{LCR}} + \frac{\Delta m_{ref}+\Delta m_A}{m_{ref}}] \quad (6.4)$$

Where ν_L is the laser frequency, V_{RFQ} is the RFQ cooler voltage and δV_{LCR} is the difference in the postacceleration voltage between two isotopes on the light collection region ($\delta V_{LCR} = |V_{LCR}^{A_{ref}} - V_{LCR}^{A}|$). V_{LCR} is the voltage related to the centroid to the resonance or hyperfine structure for each isotope. From [61], $\frac{\Delta V_{RFQ}}{V_{RFQ}} = 10^{-3}$, which is the read of the RFQ bias in a 1:10000 division of a 1000 MΩ resistive stack and $\frac{\Delta\delta V_{LCR}}{\delta V_{LCR}} = 10^{-4}$, which is the absolute accuracy on determining the cooler voltage and tuning voltages. Finally, $\delta m = |m_{ref} - m_A|$ is the difference on the atomic masses of one isotope and the reference, which an uncertainty Δm.

The extracted isotope shifts are shown at Table 6.2. As the data have been shared with S. Geldhof thesis [79], the table also shows the comparison between both analysis using ^{108}Pd as reference.

Table 6.2: *Isotope shift respect to ^{108}Pd form [134] and this work. Statistical errors are shown in round brackets, systematic errors due to voltage determination in square brackets, systematic errors due to wavemeter readout in angled brackets. Δi(MHz) accounts for the difference in frequency between both results without errors.*

Isotope	**Literature (MHz) [134]**	**This thesis (MHz)**	**Δi(MHz)**
98	2675(12)[13]	2671(6)[13]	4
100	1993(4)[25]	1991(3)[7]	2
108	0.0	0.0	0.0
112	-738(13)[13]⟨10⟩	-742(8)[13]⟨10⟩	4
114	-962(13)[13]⟨10⟩	-963(8)[13]⟨10⟩	1
116	-1080(14)[12]⟨10⟩	-1083(9)[12]⟨10⟩	3
118	-1164(13)[18]⟨10⟩	-1169(18)[18]⟨10⟩	5

6.2.2 Mean-square charge radii

The differences on mean-square charge radii can be extracted from the isotope shift using the King plot technique explained at section 3.2.1.

$$\mu^{A,A'}\delta\nu_i^{A,A'} = M_i + F_i\mu^{A,A'}\Lambda^{A,A'} \tag{6.5}$$

The field (F_i) and mass (M_i) shift factors were calculated for this transition ($4d^9 5s\,^3D_3$ - $4d^9 5p\,^3P_2$) in a previous offline work [130] (F = 2.9(6) GHz/fm^2, M = 845(669) GHz amu). The correlation of -0.999 in the linear fit between the slope (atomic field shift factor) and intercept (atomic mass shift factor) of the King plot was included on the error propagation.

From the King Plot, the charge radii (nuclear parameter Λ) is extracted. The nuclear parameter includes not only the mean-square charge radii, but also the contribution of higher moments. Therefore, to extract the mean-square charge radii, the contribution of the higher radial moments has to be estimated from muonic atom and electron scattering data available for the stable isotopes by using the following equation:

$$\Lambda^{A,A'} = (\delta\langle r^2\rangle^{A,A'} + \frac{C2}{C1}\delta\langle r^4\rangle^{A,A'} + \frac{C3}{C1}\delta\langle r^6\rangle^{A,A'} \ ... \ ) \tag{6.6}$$

Where C_n are the tabulated Seltzer coefficients [46] , which for Z=46 are $C1 = 0.543 * 10^2$, $C2 = -0.309 * 10^{-1}$, $C3 = 0.1 * 10^{-3}$. The higher moments charge distribution for one isotope can be calculated using $\langle r^n \rangle = (V_n/R^{\mu}_{k\alpha})^{-n}$ being $\delta\langle r^n \rangle^{A,A'}$ the difference between two isotopes. The muonic Barrett radii $R^{\mu}_{k\alpha}$ and ratio of radial moments V_n has been measured for palladium stable isotopes and can be found at [44]. For palladium isotopes $\Lambda^{A,A'} = 0.974\delta\langle r^2 \rangle^{A,A'}$, constituting a -2.6% averaged contribution of higher radial moments on the total charge radii.

The final results on the analysis of the mean-square charge radii of even-A isotopes is shown at Table 8.2 and Table 7.3.

Table 6.3: *Resulting changes in rms charge radii for even-A neutron deficient isotopes. Statistical errors are shown in round brackets, systematic errors due to voltage determination in square brackets and errors due to atomic factors in curly brackets.*

Isotope	$\Lambda^{A,102}$ **(fm^2)**	$\delta\langle r^2 \rangle^{A,102}$ **(fm^2)**	**Nuclear radii (fm)**
98	-0.537(2)[2]{7}	-0.551(2)[2]{7}	4.4224(33)[5]{7}
100	-0.242(1)[4]{3}	-0.249(1)[4]{3}	4.4556(31)[3]{3}

Table 6.4: *Resulting changes in rms charge radii for even-A neutron rich isotopes. Statistical errors are shown in round brackets, systematic errors due to voltage determination in square brackets, systematic errors due to wavemeter readout in angled brackets and errors due to atomic factors in curly brackets.*

Isotope	$\Lambda^{A,108}$ **(fm^2)**	$\delta\langle r^2 \rangle^{A,108}$ **(fm^2)**	**Nuclear radii (fm)**
112	0.352(3)[4]{8}⟨3⟩	0.362(3)[4]{8}⟨3⟩	4.5948(30)[5]{8}⟨10⟩
114	0.474(3)[4]{11}⟨3⟩	0.487(3)[4]{11}⟨3⟩	4.6081(30)[5]{12}⟨10⟩
116	0.560(3)[4]{15}⟨3⟩	0.575(3)[4]{15}⟨3⟩	4.6174(30)[4]{15}⟨10⟩
118	0.632(6)[6]{18}⟨3⟩	0.649(6)[6]{18}⟨3⟩	4.6252(33)[7]{19}⟨10⟩

6.3 Odd-A isotopes hyperfine Splitting analysis

As has been explained at subsection 3.2.3, isotopes with nuclear spin different than zero will have hyperfine structure. The splitting between the atomic states entails a frequency spectra composed by a number of resonances equal to the number of

allow transitions between the hyperfine states. For these isotopes, in addition to the mean-square charge radii, information regarding the spin and electromagnetic moments is extracted when fitting the spectra.

At Figure 6.7 is shown the frequency spectra from the odd-A palladium isotopes measured during this work. For fitting the hyperfine spectra is necessary to assume a value for the nuclear spin.

The $5/2^+$ nuclear spin of stable ^{105}Pd has been established from a long time. It was suggested on the 50's by an optical measurement [135] and confirmed ten years later due to the decay pattern of ^{105}Ag [136]. ^{101}Pd $5/2^+$ nuclear spin was also measured by internal conversion and γ-ray studies [137].

The experimental spectrum of ^{99}Pd is composed by four resonances with a hint of a fifth one at 6600 MHz. The apparent peak at 4900 MHz can not be considered a resonance due to its incompatibility with the natural transition linewidth. A spin assigment of $5/2^+$ was assumed based on the beta decay of ^{99}Ag [138]. The hyperfine structure was successfully fitted using $I = 5/2$. In addition, a successful fit was not possible assuming 3/2 or 7/2 spin.

At the experimental spectrum of ^{113}Pd are observed three indistinct transitions. Several structures can be inferred below 2000 MHz, however, it is not possible to resolve the peaks due to the their proximity and low production yield. ^{113}Pd spin is expected to be $5/2^+$ according to β-decay of ^{113}Rh and internal conversion systematics [139]. However, in order to unambiguously establish the spin, 3/2, 5/2, 7/2 and 9/2 has been used to fit the spectra as is shown at Figure 6.8.

Assuming I=3/2, the measured spectrum is in disagreement with the observed resonance at $\sim$ 1800 MHz. When 7/2 or 9/2 spin are considered, the resulting fit present a transition at $\sim$ 1250 MHz, which is not visible in the experimental data, with this level of statistics. Besides, the quadrupole spectroscopic moment provided from those fits are unexpectedly large compared with the systematic of the region, 2.75(9) and 4.45(15) b for 7/2 and 9/2 spin, respectively. In contrast, 5/2 spin is in agreement with the experimental results, therefore, this work establish 5/2 as the spin assignment for ^{113}Pd.

The measured spectrum at mass 115 is composed by the hyperfine structure of the nuclear ground and isomeric states of ^{115}Pd. This fact hinders the fitting procedure, due to the difficulty of associate each resonance to one of the nuclear states. In addition, the low statistics at some regions of the scan range, makes not possible to resolve some of the transitions.

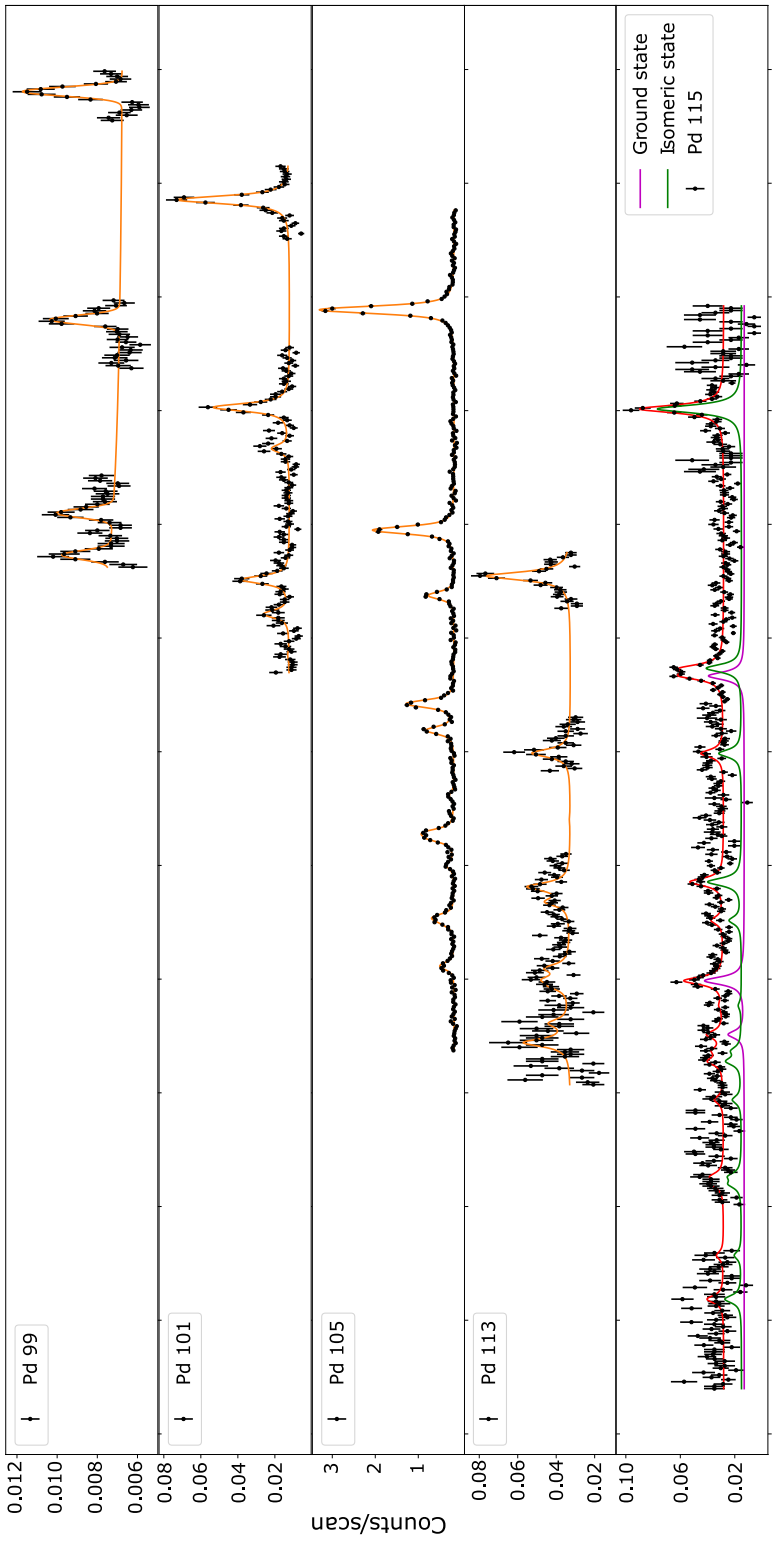

Figure 6.7: *Frequency spectra of odd-A palladium isotopes. Colored lines represent the resulting fit of each hyperfine spectra.*

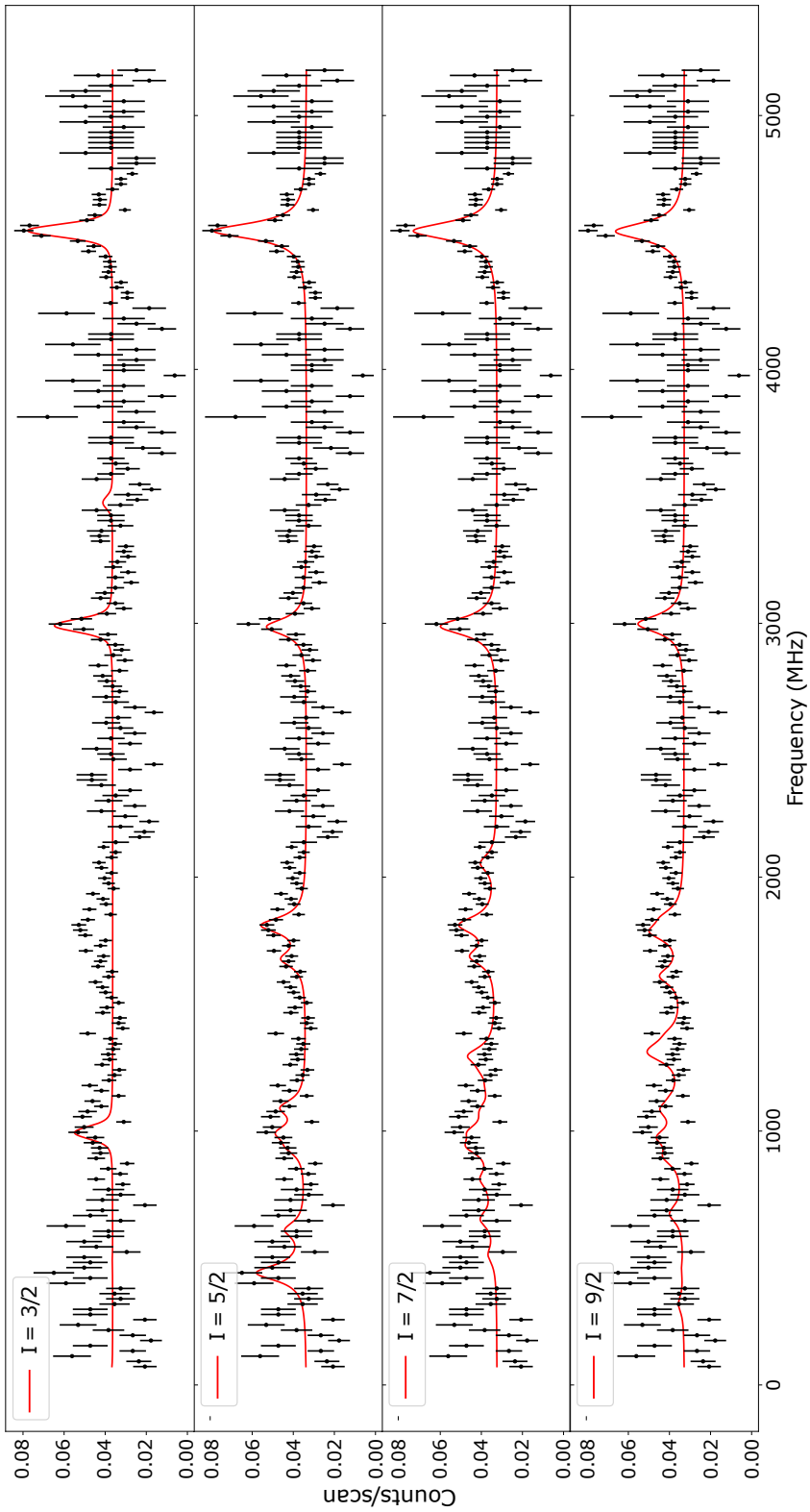

Figure 6.8: *Experimental spectra of ^{113}Pd fitted using different spin combinations.*

As was mention on subsection 2.3.1, the spin assignment on ^{115}Pd ground and isomeric states remains as an open question [68, 69]. In order to establish a spin assignment, $1/2^+$ and $3/2^+$ spins are proposed for the ground state and $7/2^-$ and $9/2^-$ spins for the isomeric state. In addition, 5/2 spin has been consider as possibility due to the systematic of odd-A palladium in the $99 \leq A \leq 113$ region. The resulting fits assuming the different spin combinations are shown at Figure 6.9 and the extracted observables are presented at Table 6.5.

Table 6.5: Magnetic (μ (nm)) and spectroscopic quadrupole (Q_s (b)) moments obtained from the fit of the resonance spectra assuming different spins (I) for the ground state (g.s.) and isomeric level (m) of ^{115}Pd.

$I^{g.s.}$	I^m	$\mu^{g.s.}$ **(nm)**	$Q_s^{g.s.}$ **(b)**	μ^m **(nm)**	Q_s^m **(b)**
$1/2^+$	$5/2^-$	-0.2967(16)	-	-0.8948(47)	-0.422(22)
$1/2^+$	$7/2^-$	-0.2957(16)	-	-0.8909(44)	0.537(26)
$1/2^+$	$9/2^-$	-0.2920(20)	-	-0.7303(36)	3.05(14)
$3/2^+$	$7/2^-$	-0.3619(25)	-0.366(18)	-0.8918(49)	0.534(25)
$3/2^+$	$9/2^-$	-0.3324(27)	-0.320(16)	-0.7281(36)	2.99(14)

The isomeric 9/2 spin assignment is unlikely due to the large quadrupole spectroscopic moment obtained when fitting the spectra ($Q_s^m \approx 3$ b). When 5/2 isomeric spin is assigned to fit the experimental data, the high likely transitions at 1500 and 3000 MHz remain unfitted. As a result, 7/2 has been concluded as the spin assignment for the isomeric state.

Concerning the nuclear ground state spin assignment, both 1/2 and 3/2 spin provide a convincing fit which results agrees with the systematics.

Until this point, the analysis has been performed without restraining the transition intensities. Due to the collinear geometry, the atoms and the photons travel through the same axis across the whole laser spectroscopy beamline. As a consequence, the interaction between both can start as soon as the ion is neutralized at the CEC. This leads to the possibility where a fraction of the atoms get exited by a photon before entering on the Light Collecting Region. For this atoms, the emitted photon is not detected and the electron may not decay into its original state post-excitation, resulting on a deviation of the experimental peak intensities from the theoretical Racah parameters.

At Figure 6.10 is presented the experimental data assuming 1/2 and 3/2 spin for the ground state and fixing the transition intensities to the theoretical Racah intensities. It is be observed a large discrepancy on the relative intensities of the

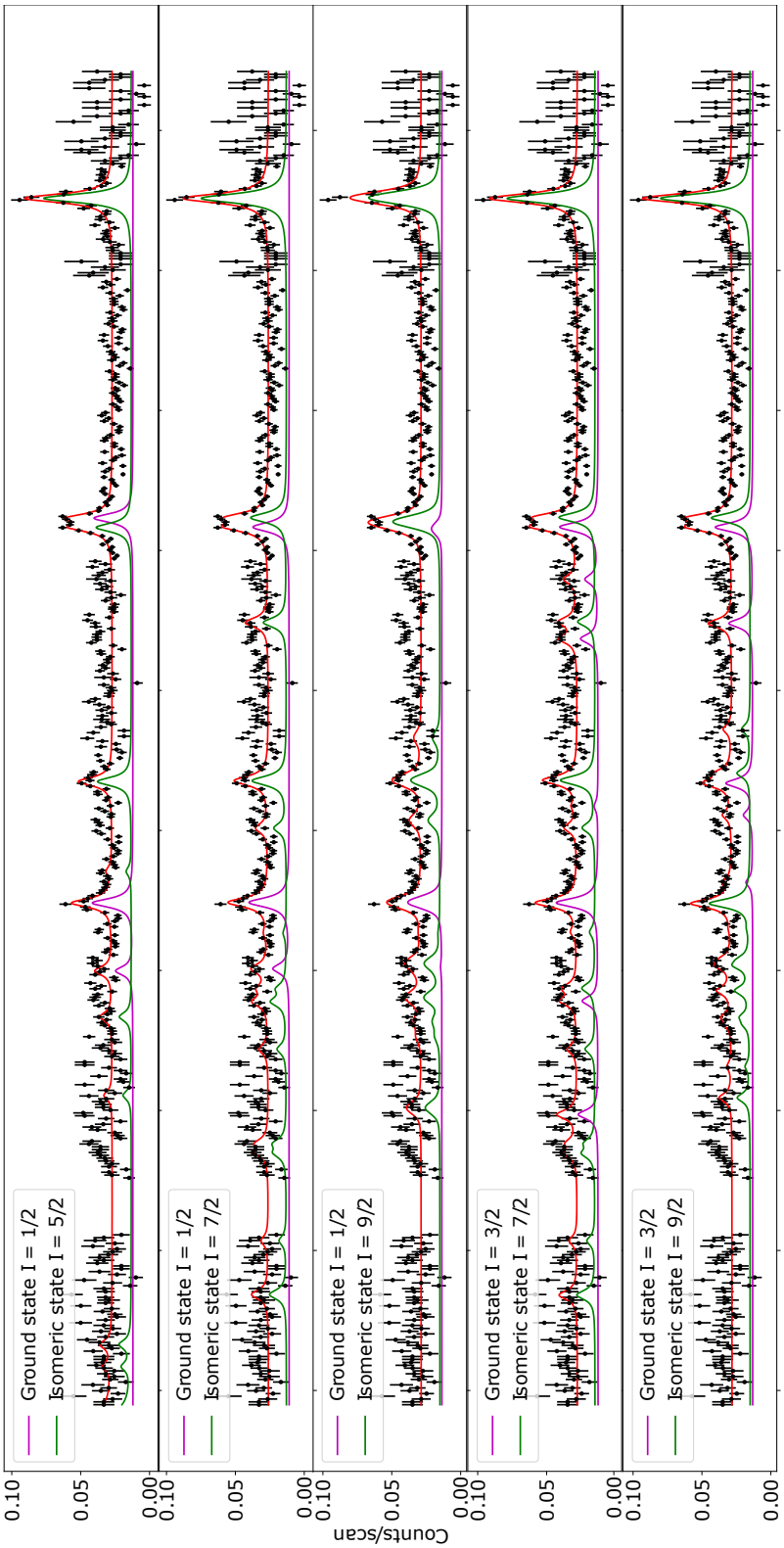

Figure 6.9: *Experimental spectra at mass 115 fitted using different spin combinations.*

1000 MHz transition when assuming spin 3/2. This effect can not be explained by the mechanism introduced on the last paragraph, as the observed resonance is more intense than the simulated transition. Moreover, the 3/2 simulated spectra shows a transition at 1600 MHz at variance with the measurement. In contrast, the theoretical intensities reproduce the experimental data when assuming 1/2 spin assignment.

Consequently, this present work concludes 7/2 and 1/2 spin assignment for the isomeric and ground state of ^{115}Pd, respectively. Which are in agreement with the tentative literature values [69] and respect the measured E3 multipolarity [67].

Using the centroid of the fit, the mean-square charge radii has been extracted using the same procedure as on the even-A isotopes explained on the previous section. The results are shown at Table 6.6 and Table 6.7.

Table 6.6: *Resulting changes in rms charge radii for odd-A neutron deficient isotopes. Statistical errors are shown in round brackets, systematic errors due to voltage determination in square brackets, systematic errors due to wavemeter readout in angled brackets and errors due to atomic factors in curly brackets.*

Isotope	$\Lambda^{A,102}$ **(fm^2)**	$\delta\langle r^2\rangle^{A,102}$ **(fm^2)**	**Nuclear radii (fm)**
99	-0.422(4)[2]{5}	-0.433(4)[2]{5}	4.4354(35)[2]{6}
101	-0.148(1)[1]{2}	-0.152(1)[1]{2}	4.4662(32)[1]{2}

Table 6.7: *Resulting changes in rms charge radii for odd-A neutron rich isotopes. Statistical errors are shown in round brackets, systematic errors due to voltage determination in square brackets, systematic errors due to wavemeter readout in angled brackets and errors due to atomic factors in curly brackets.*

Isotope	$\Lambda^{A,108}$ **(fm^2)**	$\delta\langle r^2\rangle^{A,108}$ **(fm^2)**	**Nuclear radii (fm)**
113	0.435(2)[9]{9}⟨3⟩	0.447(2)[9]{9}⟨3⟩	4.6038(29)[9]{10}⟨10⟩
115	0.493(2)[6]{13}⟨3⟩	0.506(2)[6]{13}⟨3⟩	4.6101(29)[7]{14}⟨10⟩
115m	0.633(2)[6]{13}⟨3⟩	0.650(2)[6]{13}⟨3⟩	4.6252(29)[7]{14}⟨10⟩

Aside from the centroid, the hyperfine parameters A and B (see section 3.2) has been extracted when fitting the spectra for the odd-A isotopes. A common method to extract the information about the nuclear electromagnetic moments from the hyperfine parameters is using a previously measured moment from an stable isotope, in this case ^{105}Pd. In this way it is not necessary to have information about the atomic parameters as they cancel out when making the ratio. For an isotope

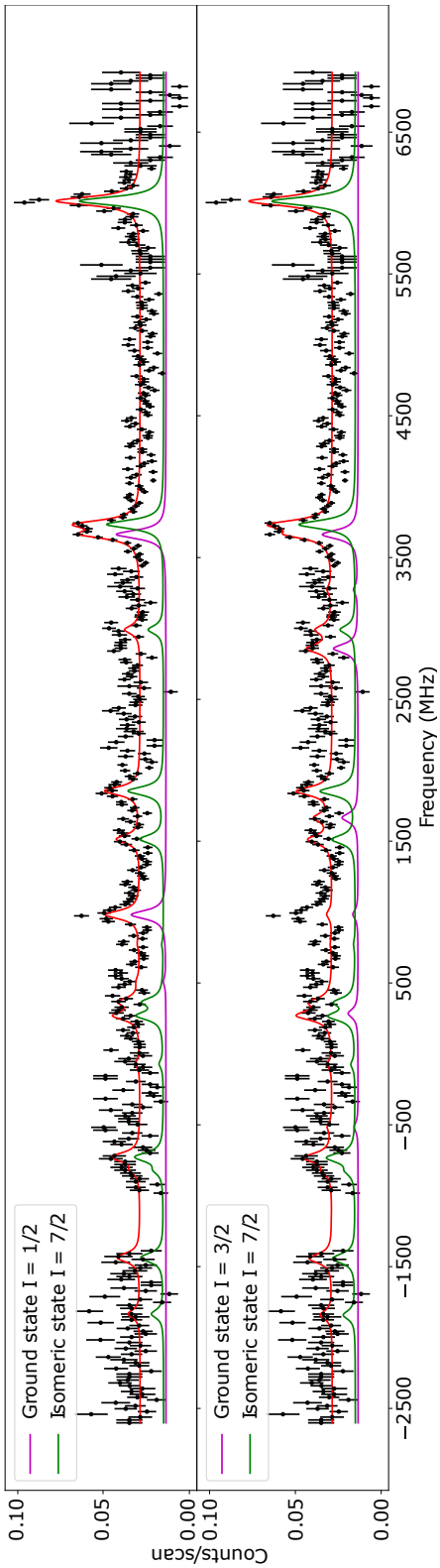

Figure 6.10: *Experimental spectra at mass 115 fitted using different spin combinations for the nuclear ground state and fixing the ratios to the theoretical Racah intensities.*

with mass number A', the magnetic and quadrupole spectroscopic moments can be calculated using the following equation.The extracted electromagnetic moments are shown at Table 6.8.

$$\frac{\mu^{A'}}{\mu^{ref}} = \frac{I^{A'}A^{A'}}{I^{ref}A^{ref}} \qquad \frac{B^{A'}}{B^{ref}} = \frac{Q_s^{A'}}{Q_s^{ref}} \tag{6.7}$$

Table 6.8: Spin (I), magnetic (μ (nm)) and spectroscopic quadrupole (Q_s (b)) moments extracted in this work. The errors on the electromagnetic moments are the statistical errors arising from the fitting procedure.

A	**I**	μ **(nm)**	Q_s **(b)**
99	$5/2^+$	-0.7546(68)	-0.14(3)
101	$5/2^+$	-0.6581(32)	-0.002(1)
113	$5/2^+$	-0.4797(27)	0.358(18)
115	$1/2^+$	-0.2957(16)	-
115^m	$7/2^-$	-0.8909(44)	0.537(26)

The interpretation and discussion of the results of the analysis will be performed on the following chapter (chapter 7).

6.4 Scattered photons background study

The introduction of bunched beam spectroscopy at the early 2000, entailed background reductions of $\sim 10^4$, by restricting the photons of interest between a time window. However, it also allows to generate frequency spectra outside the bunch. These gates can be used to study possible systematics on the background of scattered photons.

The procedure consists on sampling the TOF spectra outside the bunch, using temporal gates with equal size as the one inside the bunch. A frequency spectra is generated from each sample and divided on two groups depending on whether the gate is located before or after the arrival of the ions. The background subtracted spectra is constructed by removing half of the count rate of one spectra of each group to the experimental data spectrum. The best background subtracted spectra is manually selected between the combinations of samples which fulfill the

conditions of not having negative count rate and the counts on the main resonance being adobe a minimum. The application of the method can be shown at Figure 6.11.

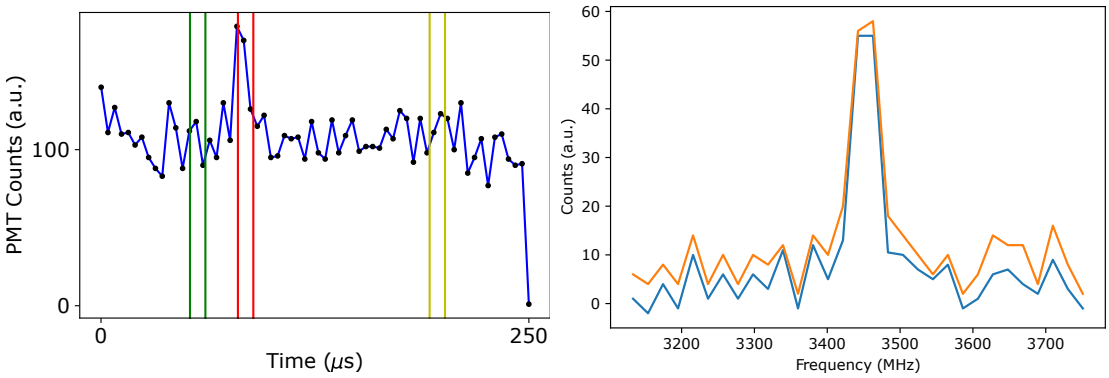

Figure 6.11: *Left: TOF spectra, the red lines indicate the bunch gate boundaries and the green and yellow lines indicate the selected background regions. Right: Experimental frequency spectra before(orange) and after(blue) background subtraction.*

At Figure 6.12, a reduction of the FWHM has been observed. However, the resulting FWHM after the application of the method is smaller than the natural linewidth of the transition.

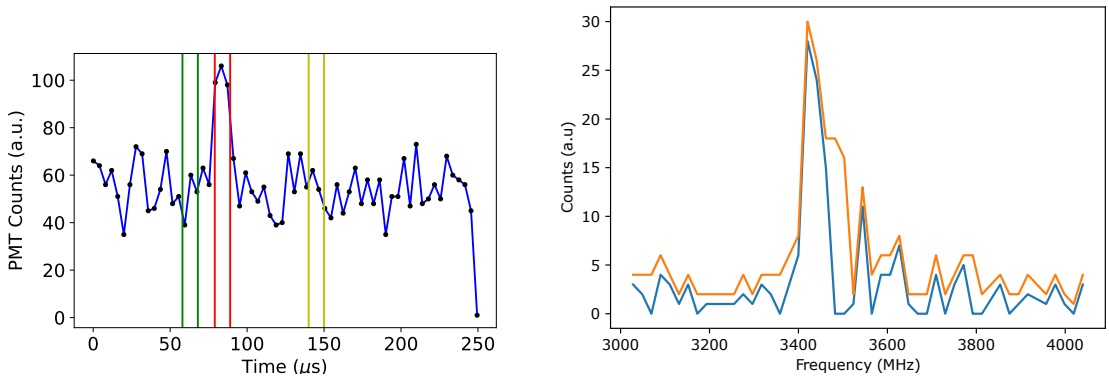

Figure 6.12: *Left: TOF spectra, the red lines indicate the bunch gate boundaries and the green and yellow lines indicate the selected background regions. Right: Experimental frequency spectra before(orange) and after(blue) background subtraction.*

This method has been applied to scans performed at mass 115. At Figure 6.13 can be observed how the signal versus background is increased for the smaller resonances on that frequency range, improving the identification. The combination

of gates have been selected looking for the most convincing spectra, therefore this method is unreliable to verify the presence of small resonances.

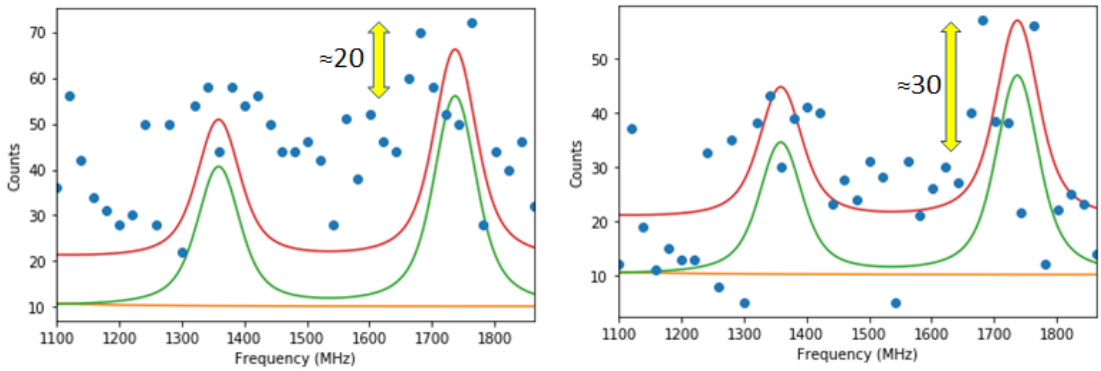

Figure 6.13: *Effect of background subtraction in the frequency range 1100-1900 MHz in the ^{115}Pd frequency spectra. Left) Spectrum without background subtraction, Right) Spectrum with background subtraction.*

A detailed analysis using SATLAS has proved than these effects result on an alteration on the distribution of the experimental data. This alteration hinders the fitting procedure leading to an increase on the reduced chi-square, as can be shown at Table 6.9.

Table 6.9: *Analysis of the background effect on ^{108}Pd.*

	Normal analysis		**Background analysis**	
	Reduced χ^2	FWHM (MHz)	Reduced χ^2	FWHM (MHz)
Figure 6.12	1.18	98(23)	2.1	43(6)

By this work has been verify the background homogeneity. The scattered photons are randomly distributed across the frequency spectra and do not induce any effect on the analysis.

Chapter 7

Interpretation & Discussion

In this chapter the results will be discussed. The discussion is going to be divided in two parts. The first section focus on the systematics, comparing palladium with the even-Z elements on the region between zirconium (Z=40) and tin (Z=50). The second section contains a study of the evolution of deformation on the palladium isotopic chain using state-of-art theoretical calculations.

7.1 Systematic on the region

The measurement of observables across an isotopic chain can provide an insight of the evolution of nuclear structure. In addition, comparing these results with neighbour elements contribute to a global understanding of a region of the nuclear chart.

The magnetic dipole moment has a dependence on the spin of the nucleus, in order to simplify the comparisons, the g-facto have been used. At Figure 7.1, the g-factor of palladium isotopes is plotted together with the g-factor of the even-Z isotopes on the region (Mo, Ru and Cd).

At the proximity of the N=50 shell gap, the g-factor of isotopes with spin 5/2 agrees well with the quenched single particle $d_{5/2}$ g-factor, however, as increasing the neutron number the g-factor deviates from this value. This trend can be interpreted as a higher collective behavior when approaching the mid shell.

The coherent behavior of the g-factor for different nuclei with 5/2 spin contrast

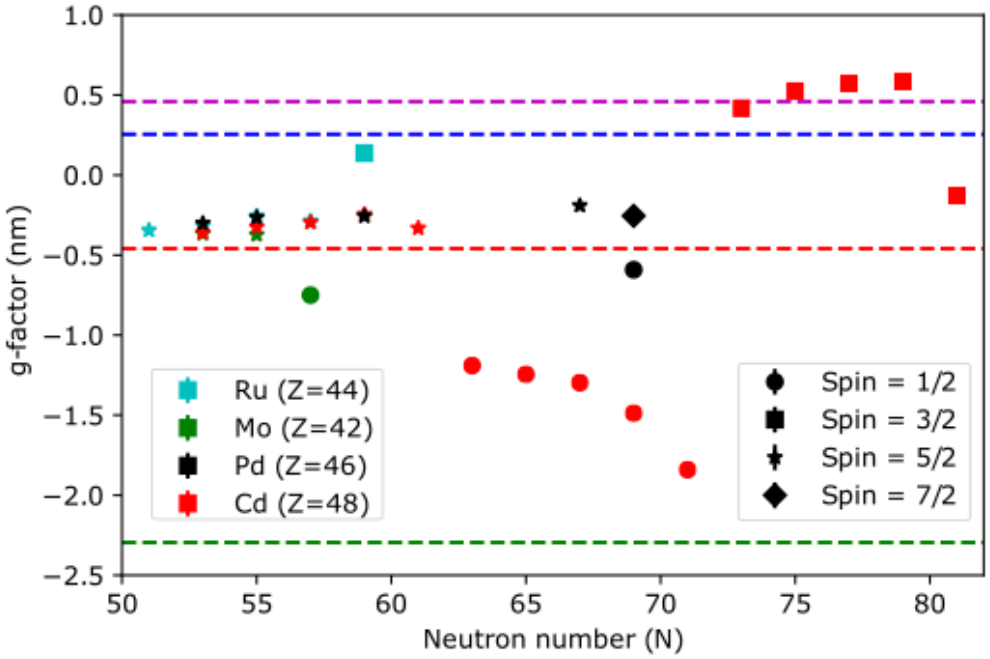

Figure 7.1: *G-factor of the even-Z isotopes on the region* $40 < Z < 50$ *plotted against neutron number. The color of the marker indicates the element: green Mo(Z=42), blue Ru(Z=44), black Pd(Z=46) and red Cd(Z=48). The shape of the marker indicates the nuclear spin of the isotope: circle I=1/2, square I=3/2, star I=5/2 and diamond I=7/2. The dashed line represent the 0.6-quenched Schmidt values: the magenta line for I=3/2, the blue line for I=7/2, the red line for I=5/2 and the green line for I=1/2. Ru and Mo data taken from [140] and Cd from [141].*

with the scattered values for spin 1/2. The measured g-factor for I=1/2 has a discrepancy with the quenched single particle for all isotopic chains. Cd isotopes show a trend with seems to approach this value when adding neutrons, however, Ru(N=57) and palladium(N=69) present a much more collective behavior.

The same analysis has been performed with the quadrupole electric moment. Assuming axial symmetry, the quadrupole electric moment has been calculate using equation Equation 2.22.

In Figure 7.2, the quadrupole electric moment is plotted against the proton number. The flat shape of the isotonic lines suggest that there is no significant effect on the deformation with increasing Z.

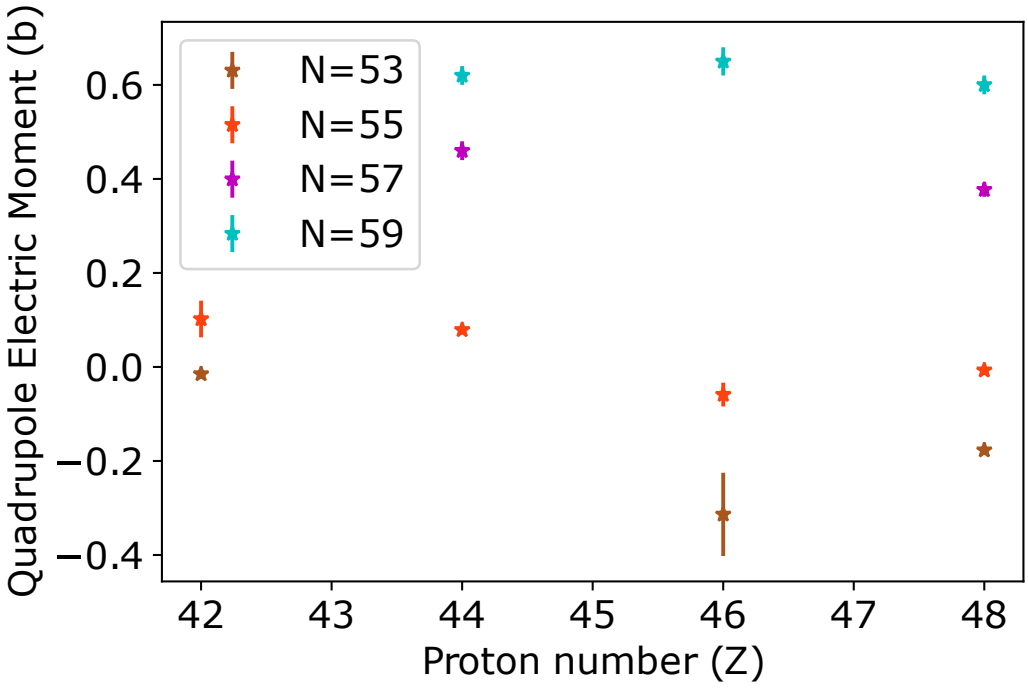

Figure 7.2: *Quadrupole electric moment of the even-Z isotopes on the region* $40 < Z < 50$ *plotted against proton number. The color of the marker indicates the isotonic lines: brown =53, orange N=55, magenta N=57 and blue N=59. Ru and Mo data taken from [140] and Cd from [141].*

At Figure 7.3, the quadrupole electric moment is plotted against the neutron number. Systematics of the region show a linear trend, probably due to the addition of neutron pairs to the $d_{5/2}$ shell plus an odd neutron up to N=59. The small increase between the ^{105}Pd and the ^{113}Pd and between ^{107}Cd and the ^{109}Cd could be due to that the neutron occupation of the $d_{5/2}$ shell is already at maximum [141].

In order to perform a more exhaustive discussion, theoretical calculations are needed. At the following section, state of art energy density functionals will be used to study the nuclear structure of palladium isotopes focusing on deformation.

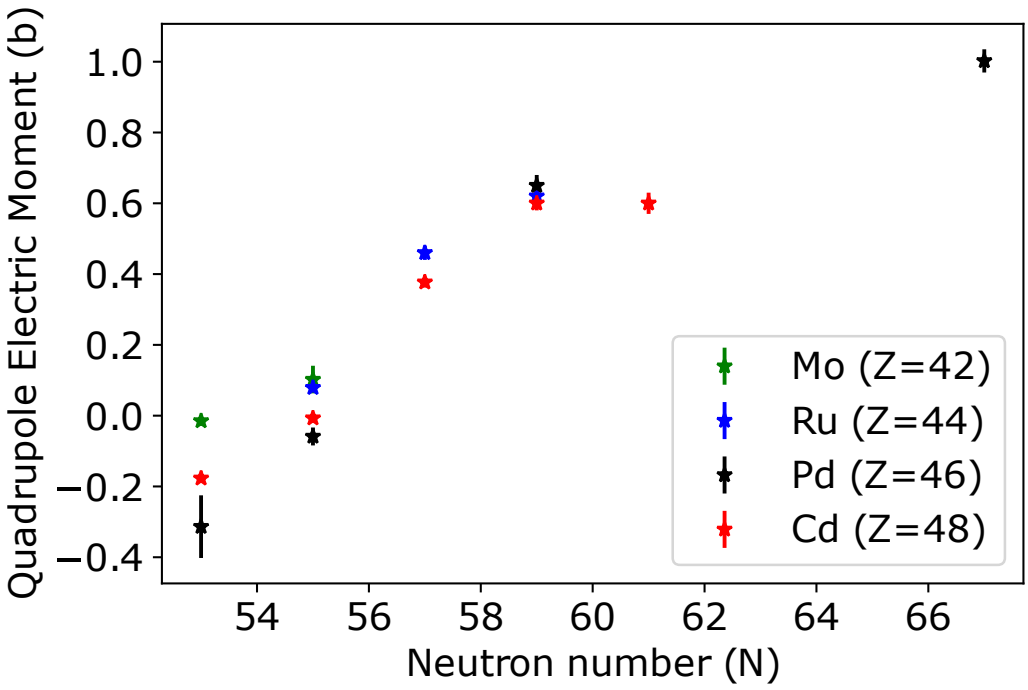

Figure 7.3: *Quadrupole electric moment of the even-Z isotopes on the region* $40 < Z < 50$ *plotted against neutron number. The color of the marker indicates the element: green Mo(Z=42), blue Ru(Z=44), black Pd(Z=46) and red Cd(Z=48). Ru and Mo data taken from [140] and Cd from [141].*

7.2 Evolution of deformation on Pd isotopes

To shed light on the evolution of the measured observables, the results have been compared with different theoretical calculations. The spectroscopic properties have been computed with different versions of energy density functional (EDF) that has been introduced at chapter 2: Gogny D1S [36], Fayans Fy(std) [24] and Fy(Δr,HFB) [26]. The purpose is study the nuclear structure of palladium isotopes from an axial and triaxial point of view.

The most direct way of study the deformation is through the quadrupole spectroscopic moment. Assuming axial symmetry the β_2 elongation parameter can be deduced, giving a hint on the character of the deformation. In addition, theoretical calculations of the β_2 parameter on an axially symmetric context have been performed in order to understand these results. The experimental values and theoretical calculations are presented on Figure 7.4.

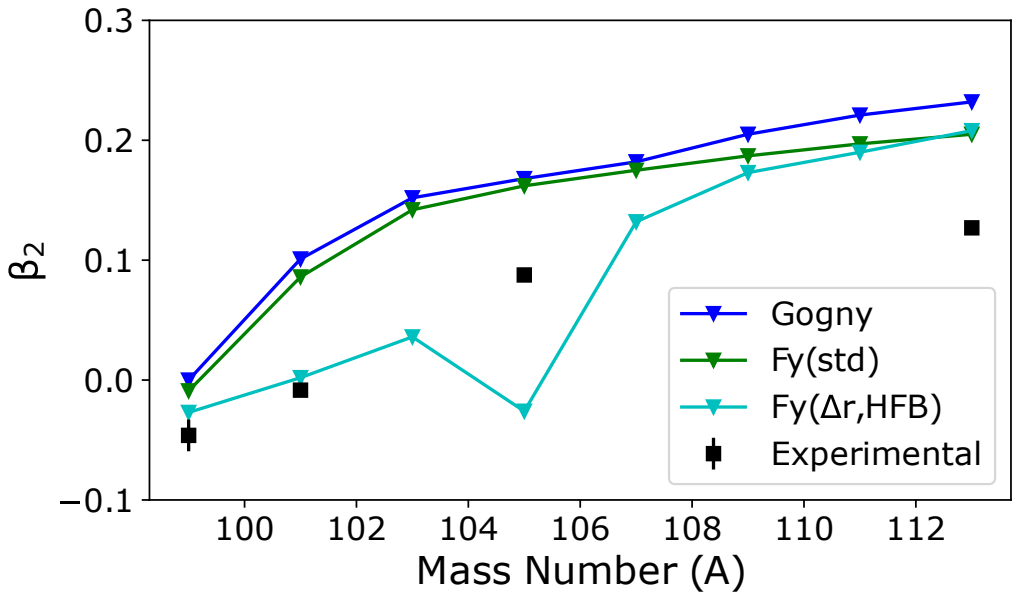

Figure 7.4: *Comparison of experimental β_2 elongation parameter and theoretical Gogny D1S, Fayans Fy(std) and Fy(Δr,HFB) calculations assuming axial symmetry.*

Table 7.1: *Experimental and theoretical β_2 elongation parameter assuming axial symmetry for Pd nuclei.*

Isotope	**Experimental**	**Fy(std) (fm^2)**	**Fy(Δr,HFB) (fm^2)**	**Gogny (fm^2)**
99	-0.046(13)	-0.009	-0.027	0.000
101	-0.008(3)	0.086	0.002	0.101
105	0.087(4)	0.162	-0.026	0.168
113	0.127(4)	0.205	0.208	0.232

^{99}Pd and ^{101}Pd isotopes have 53 and 55 neutrons, respectively, being just few neutrons away of the N=50 shell closure where is expected spherical shape. The β_2 parameter resulting from the theoretical calculations is in agreement with the experimental value of ^{99}Pd, however, Fayans Fy(std) and Gogny D1S deviates from the experimental trend for ^{101}Pd. Fy(Δr,HFB) does a better work, being able to reproduce the negative character of the deformation parameter for ^{99}Pd and the small deformation of ^{101}Pd.

The evolution between these isotopes can be understood plotting the binding energy versus deformation as is shown at Figure 7.5. At the figure it can be appre-

ciate the transition from prolate deformation at ^{102}Pd to the spherical shape at the semimagical ^{96}Pd. This transition character leads to a diffusion of the binding energy which might be an indication of soft nuclei and can entail a slightly negative β_2 parameter.

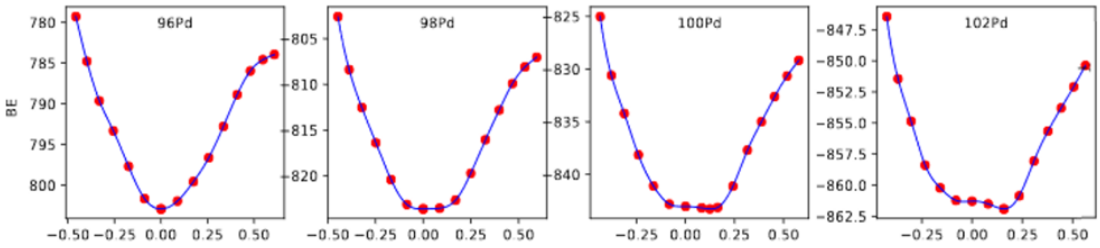

Figure 7.5: *Fayans calculation of binding energy versus deformation for* ^{96,98,100,102}*Pd.*

On the neutron rich side, none of the theoretical calculations are able to reproduce the deformation, being overestimated. One possible explanation for this disagreement can be the axial symmetry assumption. This explanation is supported by the flattering of the binding energy present at Figure 7.5 which indicates that probably an axial description is not sufficient for explaining the deformation on the Pd chain.

Previous studies suggested that palladium isotopes in the neutron rich region might exhibit fingerprints of triaxiality [142, 143]. In this context,the Potential Energy Surface (PES) have been calculated using the triaxial beyond mean field SCCM method (Figure 7.6).

As can be observed at Figure 7.6, ^{96}Pd at the neutron shell closure present a well defined spherical shape. The minimum position evolves with increasing the neutron number, indicating first prolate deformation and becoming more diffuse as approaching the mid-shell. The PES strongly indicate triaxial shape for isotopes starting at ^{108}Pd and might explain the discrepancy presented at Figure 7.5 for ^{113}Pd.

In order to have a more complete picture, the evolution of deformation can be studied through the root mean square (rms) charge radii. In addition, the rms charge radii can provide a more direct comparison between the results obtained at this thesis and the theoretical calculations.

At Table 7.2 and Table 7.3, the measured changes in rms charge radii can be found together with the theoretical calculations for neutron rich and deficient palladium isotopes.

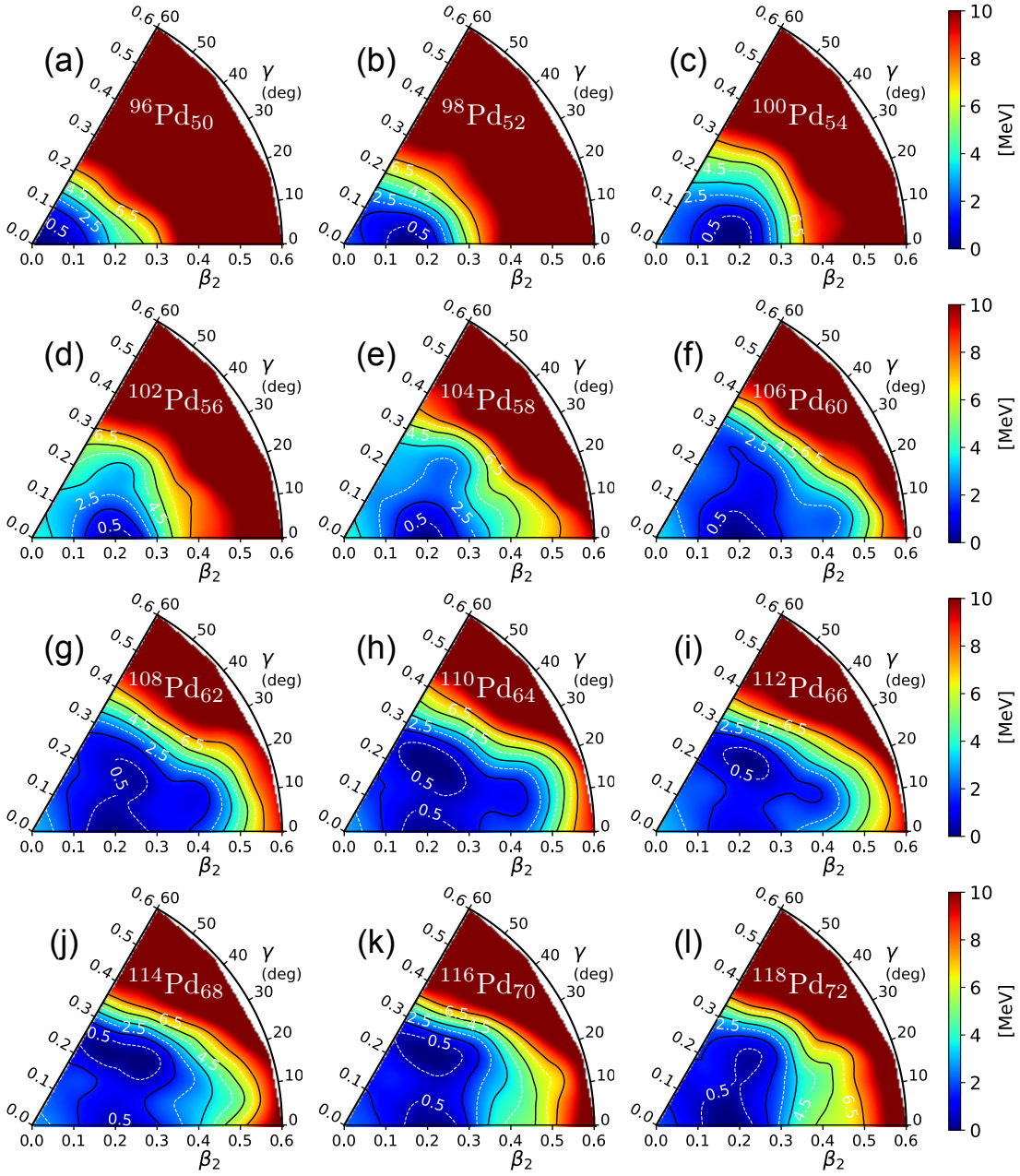

Figure 7.6: *Potential Energy Surface (PES) of even-even palladium isotopes calculated using the SCCM method.*

Figure 7.7 shows the difference on rms charge radii respect ^{108}Pd ($\Lambda^{A,108}$). It is observed a smooth trend when increasing the neutron number, indicating that there are no sudden changes on deformation. This general trend is followed by all the theoretical calculations.

Table 7.2: *Difference in rms charge radii respect ^{102}Pd obtained at this work and state of art nuclear calculations using Fayans EDF and Gogny force.*

Isotope	$\Lambda^{A,102}$ **(fm^2)**	**Fy(std) (fm^2)**	**Fy(Δr,HFB) (fm^2)**	**Gogny (fm^2)**	**SCCM (fm^2)**
98	-0.537(2)[2]{7}	-0.514	-0.602	-0.576	-0.452
99	-0.422(4)[2]{5}	-0.461	-0.532	-0.514	-
100	-0.242(1)[4]{3}	-0.240	-0.311	-0.240	-0.188
101	-0.148(1)[1]{2}	-0.249	-0.240	-0.267	-

Table 7.3: *Difference in rms charge radii respect ^{108}Pd obtained at this work and state of art nuclear calculations using Fayans EDF and Gogny force.*

Isotope	$\Lambda^{A,108}$ **(fm^2)**	**Fy(std) (fm^2)**	**Fy(Δr,HFB) (fm^2)**	**Gogny (fm^2)**	**SCCM (fm^2)**
112	0.352(3)[4]{8}⟨3⟩	0.318	0.393	0.327	0.366
113	0.435(2)[9]{9}⟨3⟩	0.464	0.546	0.399	-
114	0.474(3)[4]{11}⟨3⟩	0.464	0.559	0.454	0.521
115	0.493(2)[6]{13}⟨3⟩	0.491	0.546	0.399	-
116	0.560(3)[4]{15}⟨3⟩	0.564	0.688	0.537	0.621
118	0.632(6)[6]{18}⟨3⟩	0.601	0.790	0.591	0.684

The triaxial SCCM calculations are able to reproduce the evolution of the rms charge radii, having general a good agreement. In contrast, axial Gogny calculations present a good agreement on the neutron deficient and neutron rich sides, as is shown in Table 7.2 and Table 7.3. However, the overall agreement is missed, as is not able to perform a good reproduction of the changes of rms charge for the stable isotopes. According to the Figure 7.6, at this mass region starts the transition to triaxiality.

An exhaustive interpretation on the systematics of nuclear charge radii using Fayans EDF can be found at [134]. This article provided the first analysis on mean square charge radii of well deformed nuclei using Fayans functionals. The charge radii of Pd isotoppes was study using UNEDF2 Skyrme EDF model [144], Fy(std) and Fy(Δr,HFB). The work concluded that Fy(Δr,HFB) does a better reproduction thanks to the strong coupling in the pairing, which increases the absolute charge radii.

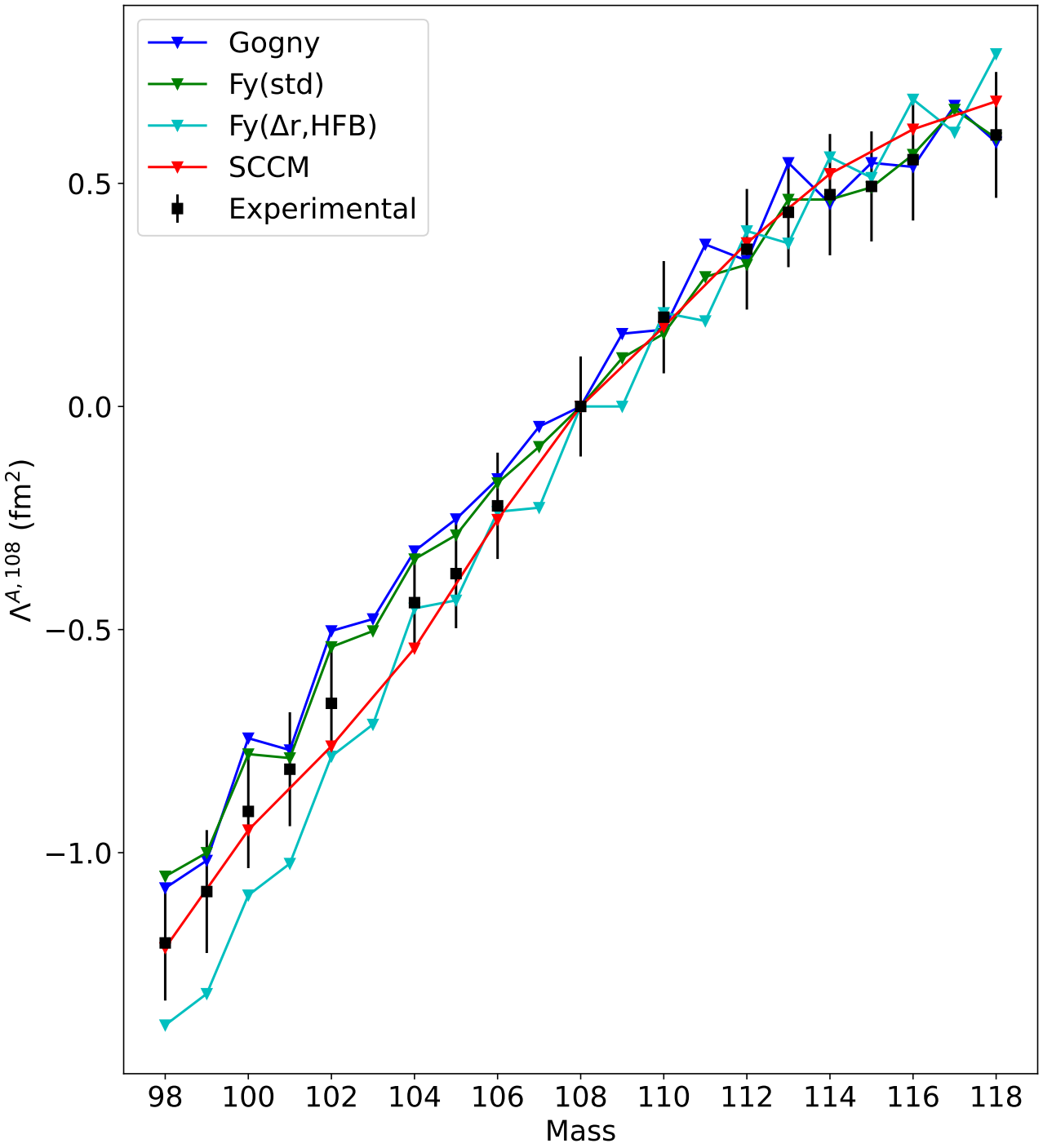

Figure 7.7: *Difference on rms charge radii respect* ^{108}*Pd plotted against mass number A.*

The data discussed at [134] is the same data which is presented at this thesis, as the analysis has been performed in parallel. This work contributes with a better insight on the OES staggering thanks to the addition of the odd-A isotopes ^{113,115}Pd.

In order to study small-scale effects as the odd–even staggering (OES), the three-point odd-even charge radii staggering formula (Equation 7.1) is used [145]. The resulting OES is plotted at Figure 7.8.

$$\Delta_r^{(3)} = \frac{1}{2}(R_{A+1} + R_{A-1} - 2R_A) \tag{7.1}$$

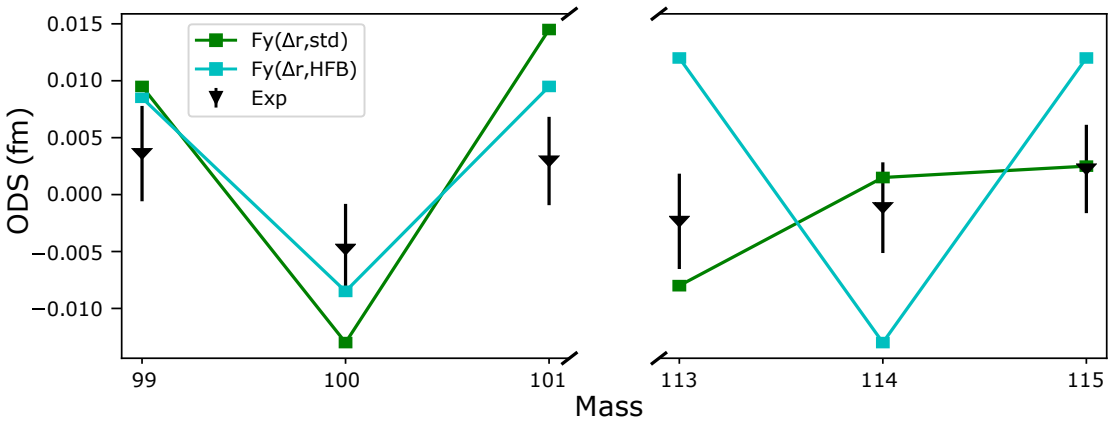

Figure 7.8: *Comparison of experimental and theoretical three-point odd-even staggering on the charge radii.*

At Figure 7.8 is shown the different pattern of odd-even staggering present at each mass region. At the light region, classic OES is observed, the even-A isotopes have a smaller radius relative to the odd-A nuclei. In contrast, the OES flattens on the neutron rich region. The origin and character of the flattering still unclear, in the future, the measurement of the intermediate cases might provide a better understanding on the evolution of the OES.

The normal OES exhibited by the neutron deficient isotopes is well reproduced by both Fayans fuctionals, being Fy(Δr,HFB) closer to the actual strength. Nevertheless, Fy(Δr,HFB) is not able to reproduce the flattening on the neutron rich side, as it keeps presenting the same pattern. Fy(std) calculations show a better agreement, being able to reproduce the flattened between ^{114}Pd and ^{115}Pd.

As has been mention and was discussed at [134], Fy(Δr,HFB) does a better reproduction of the absolute charge radii on the palladium isotopic chain than Fy(std)

which underestimates the absolute charge radii. The reason are the strong pairing correlations which modify the mean field at the nuclear surface, increasing the charge radii and enhancing the OES.

Even if the pairing is the dominant contributor to the odd-even staggering, is not clear the influence of other mechanisms [53]. Therefore, the different behavior between the different Fayans functional on the neutron rich side can be explained as the influence of other effects at Fy(std) which are overwhelmed by the strong pairing correlations at Fy(Δr,HFB).

Chapter 8

Perspectives

This chapter contains the preparation for future measurements of Pd isotopes towards the proton drip line.

The most neutron deficient nuclei measured during this thesis has been ^{98}Pd which is just two neutrons away of the $N = 50$ shell closure. As has been presented at section 2.3, palladium can play a role on the study of the strength of the kink at N=50.

The future measurements on neutron deficient palladium have been pursued from two different approaches.

The first approach uses a method created by Mikael Reponen at the IGISOL facility tailored to measure ^{94}Ag [114]. This method combines efficient in-source RIS in a hot-cavity catcher with sensitive ion detection via the phase-imaging ion-cyclotron resonance (PI-ICR) Penning trap mass spectrometry technique [146]. This system has proved to be really efficient for measuring at this region, being able to perform resonance ionization spectroscopy with on-resonance signal rates as low as $\sim$0.005 ions per second for ^{96}Ag. A test for Pd production through the hot-cavity catcher will be presented on this chapter.

The disadvantage of this approach are the limitations concerning the resolution. As has been discussed on section 3.4, in-source laser spectroscopy techniques have finite resolution due to the Doppler broadening generated by the high temperatures.

The second approach account for in-gas jet laser spectroscopy at the future S^3-

LEB facility. Improved resolution can be achieved with this state of art technique thanks to the low pressure and temperature environment achieved at supersonic jets. In addition, according to the predicted production yields, beams provided by the S3 Super-Spectrometrer will have enough counting rates to measure palladium isotopes beyond the N=Z line.

In order to be able to perform efficient ionization at the S^3-LEB facility, offline testing and development of RIS schemes have been performed at the GISELE laboratory (see section 4.3). In this context, resonance ionization spectroscopy of stable palladium isotopes will be presented on this chapter.

8.1 Palladium In-source production test

The inductively heated hot cavity catcher was constructed at IGISOL for the production of low-energy ion beams on the N=Z region, targeted to improve the production efficiency of ^{94}Ag [114]. Subsequent to its success on silver [58], this approach has been studied for the production of palladium isotopes.

With this aim, a palladium production test has been performed using the setup presented at section 4.2. A 495 MeV $^{106}Pd^{+18}$ stable beam, produced by the K130 cyclotron, was implanted on the hot catcher. The diffused atoms are laser ionized by a three step resonance ionization scheme, and extracted through the SPIG. Finally, the ions of interest are mass separated from the contaminants by the dipole magnet and detected by a Faraday cup (see Figure 8.1).

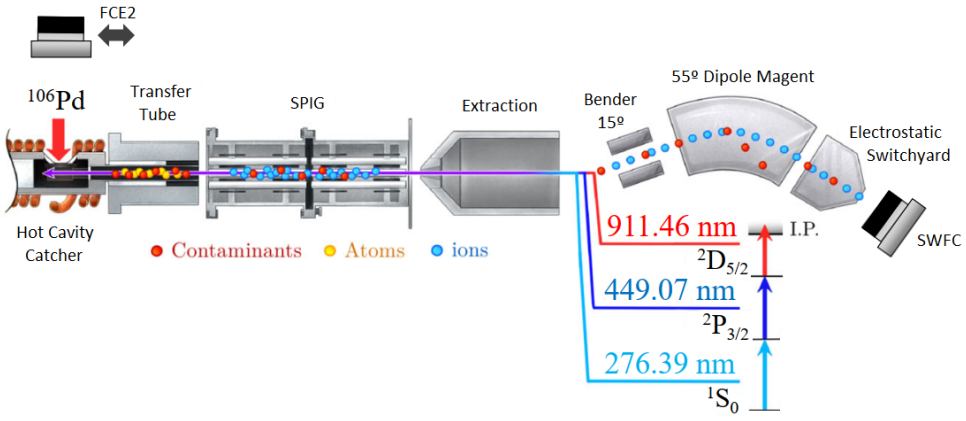

Figure 8.1: *Overview of the experimental setup used during the production test.*

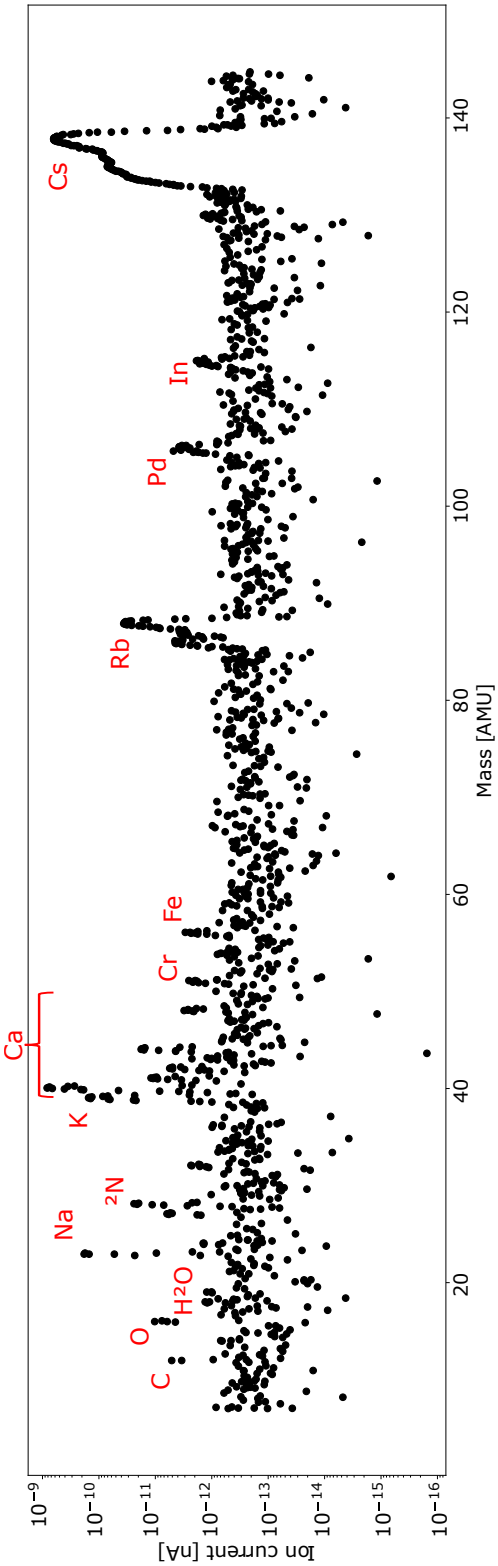

Figure 8.2: *Dipole magnet mass scan.*

In order to study the diffusion of Pd isotopes from the catcher, the dipole magnet was used to scan across a wide range of mass. The scan is shown at Figure 8.2. As expected, the main contaminants are the alkali metals (Na, K, Rb, Cs), in addition, there is a no negligible amount of contamination of diatomic nitrogen and Ca. Figure 8.3 shows a scan of the magnetic field corresponding to the mass region of interest. It can be observed on that only one mass is produced, corresponding with ^{106}Pd. Therefore, there is not contamination from other nuclei on this mass region.

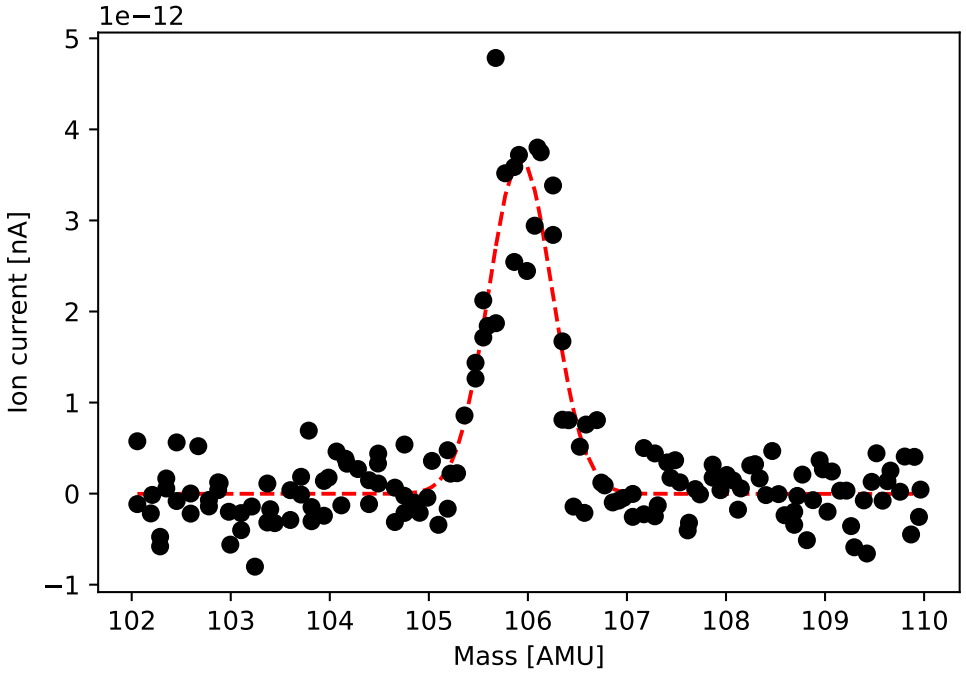

Figure 8.3: *Dipole magnet mass scan on the palladium mass region.*

The dipole magnetic field has been used to select the ^{106}Pd ions of interest, measuring a production of 0.022 pA on the Faraday cup (SWFC). 31 pA of $^{106}Pd^{+18}$ delivered by the cyclotron have been measured by another Faraday cup (FCE2) located just before the target chamber. Taking into account a 90% efficiency of the FCE2 [147] and the +18 charge state, the total efficiency has been estimated to be $\sim 1.4\%$. This efficiency is comparable to the efficiency for silver ($\sim 1\%$ after mass separator [58]).

Aside the efficiency, the limiting factors for measuring exotic isotopes are the diffusion and implantation times for palladium on the catcher, as the half life is

decreasing when approaching the proton drip line. To study the effect of both contributions, the FCE2 was used to block the cyclotron beam. The cyclotron beam was stopped using the Faraday cup to measure the Pd diffusion, and removed to estimate the implantation time on the catcher. Due to the insertion time of the FCE2 of about 100 ms, is not possible to accurately measure times under or close to that value.

Several measurements of the implantation and diffusion times were performed, being one of them presented at Figure 8.4. From the time profile, a implantation time $\sim$ 100 ms and a diffusion time $\sim$ 200 ms were estimated. With the measured efficiency and the predicted rates, the most exotic nuclei which will be possible to access is ^{92}Pd ($t_{1/2} = 1$ s).

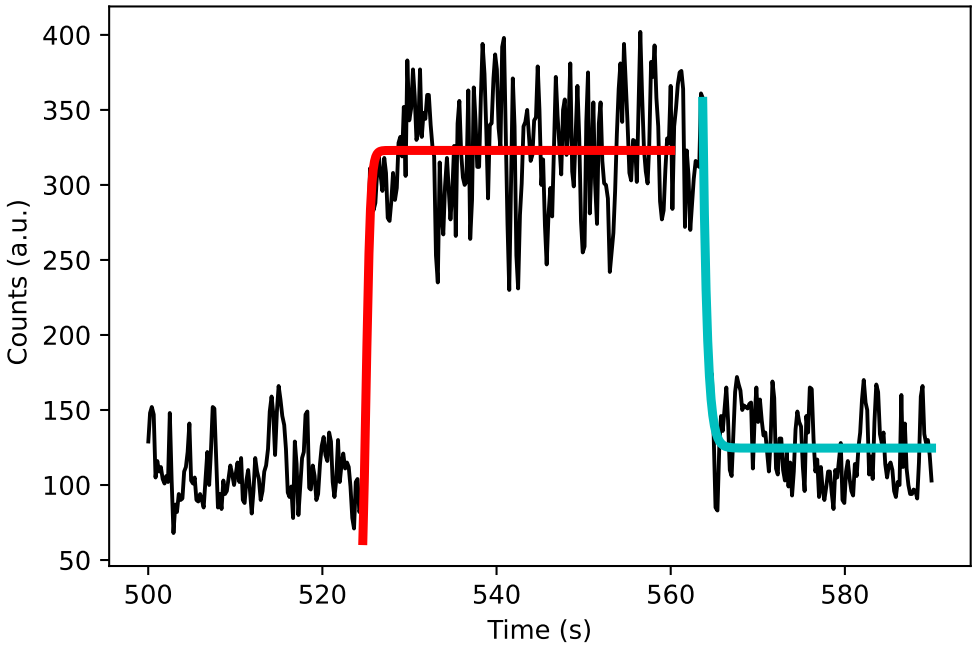

Figure 8.4: *Timing profile of laser-ionized ^{106}Pd atoms. A fit of the implantation time ($\sim$ 100 ms) is presented in red, and on the diffusion ($\sim$ 200 ms) in cian.*

The three step ionization scheme used to selectively ionize palladium was developed by Mainz [127]. In order to maximize the efficiency on the laser ionization with optimal resolution, a saturation measurement was performed for each step, and are presented at Figure 8.5. The saturation powers (P_{sat}) have been found fitting the curves with the following equation:

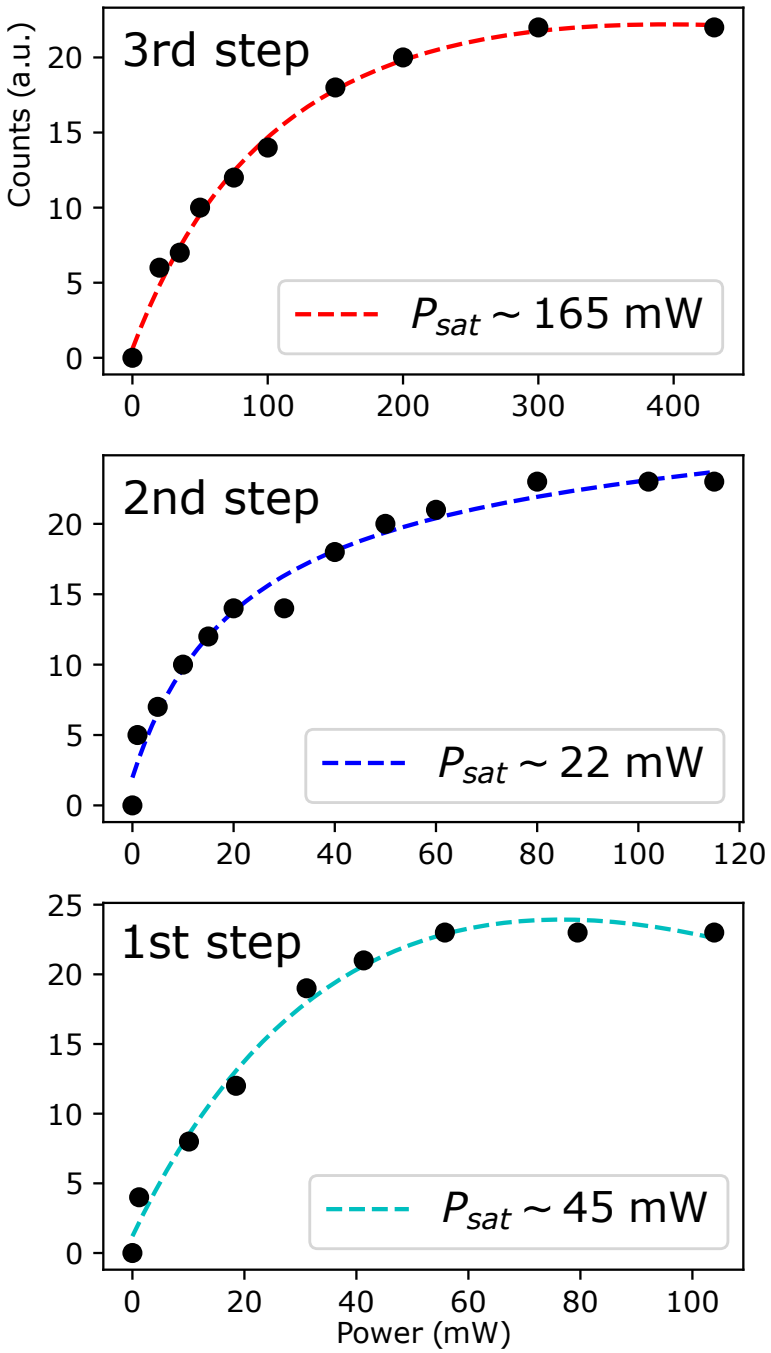

Figure 8.5: *Laser saturation measurements. Left: First step. Center: Second step. Right: Third step.*

$$I(P) = a + b \cdot P + c \cdot \frac{P}{P + P_{sat}} \tag{8.1}$$

The discrepancy between the saturation powers between this work and [127] are generated by the loses on the mirrors located on the path between the laser table and the target chamber, as the powers were measured on the laser table. In addition, the loses are wavelength dependent due to the different mirrors used and there can be differences on the laser spot sizes.

Wavelength scans were performed at different laser powers (Figure 8.6). The FWHM bellow saturation is 34 GHz. As the measurement was performed using a single etalon and scanning the first step, this resolution can be related with the linewidth of the laser for a UV light ($3 * 10$ GHz).

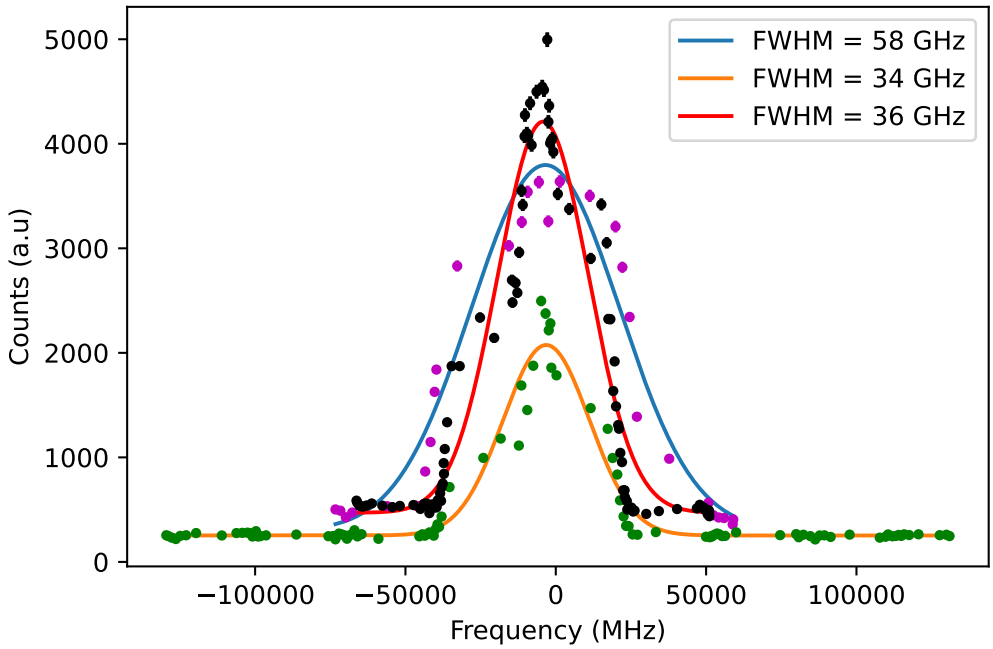

Figure 8.6: *Wavelength resonant first step scan for power bellow saturation (orange line), above saturation (blue line) and at saturation (red line).*

The results of these test prove the capability of the method to produce palladium isotopes. As a result, a proposal will be submitted to measure neutron deficient isotopes across the N=50 shell gap, and aiming to reach to the N=Z line.

8.2 S^3-Low Energy Branch

Looking towards the limits of stability, the measurement of palladium isotopes up to ^{91}Pd could be a possibility on the future S^3-Low Energy Branch (S^3-LEB) at the SPIRAL2 facility in GANIL.

As part of the new generation of nuclear experimental facilities, the SPIRAL2 project will explore the use of fusion-evaporation reactions to study exotic neutron-deficient isotopes at the N = Z region around ^{100}Sn and in the very-heavy and super-heavy element regions [148]. The superconducting LINAC will produce stable ion beams from He to U with energies from 0.75 up to 14.5 MeV/u, and intensities from 1pμA up to Ni [148]. In order to handle the very intense heavy ion-beams beams assuring high mass resolution and large transmission capabilities, the Super Separator Spectrometer (S^3) was developed to perform experiments with extremely low cross sections [149].

The detection instrumentation at the focal plane of S^3 consist on two complementary set-ups: a highly sensitive decay spectroscopy set-up SIRIUS (Spectroscopy and Identification of Rare Isotopes Using S^3) and S^3-LEB to perform precision mass measurements and laser spectroscopy. SIRIUS and S^3-LEB are constructed as mobile setups to exchange each other at the S^3 focal plane.

At SIRIUS, the ions are implanted into a Double-sided Silicon Strip Detector (DSSD) of 10x10 cm^2 which each side segmented into 128 strips. The DSSD is covered by a box-like arrangement of Pad silicon detectors with 8 x 8 pixels to measure charged particles and a large volume Ge array to detect γ-rays. Before implantation tracker Secondary Electron Detectors (SED) are located in beam direction for veto and time-of-flight purposes [150].

The S^3-LEB is shown at Figure 8.7. At this setup, the radioactive ion beams (RIBs), will enter into the gas cell through a thin entrance window. This window will have to withstand a pressure difference of 10^7 to 10^{10} orders of magnitude between the S^3 beam line and the S^3-LEB gas cell. Inside the gas cell, the ions are thermalized and neutralized in the Argon buffer gas. The gas cell will operate at 200-500 mbar leading a extraction time of about 300 ms.

The atoms are extracted in a collimated and homogeneous hypersonic gas jet, created by a Laval nozzle attached to the gas cell exit throat. As was discussed at section 3.4, resonance laser ionization at low pressure and low temperature gas jet conditions lead on a reduction of about an order of magnitude on the broadening effects, compared to hot cavity and in-gas cell, while maintaining high selectivity

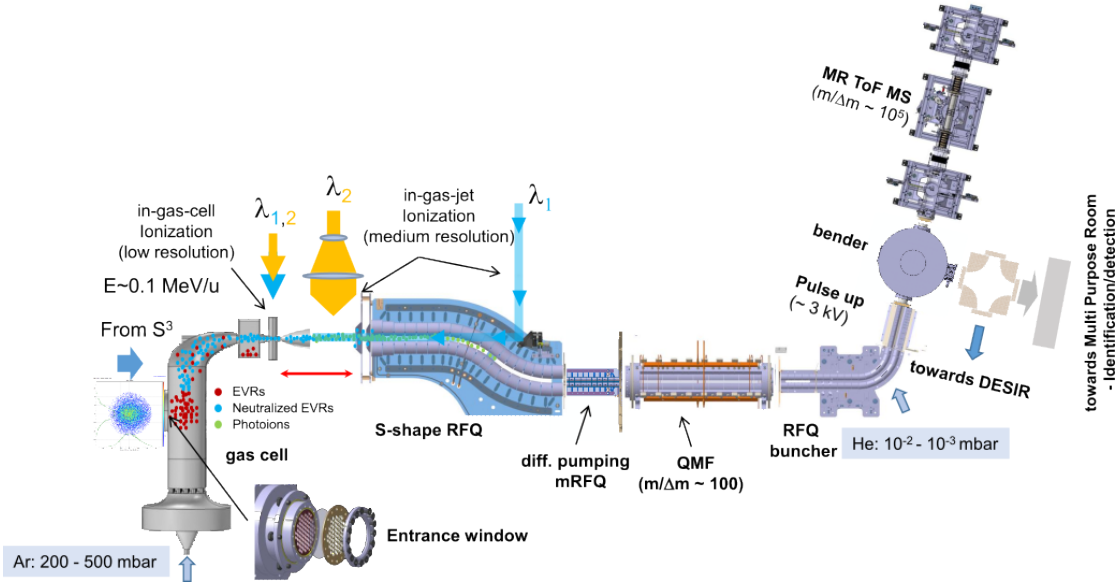

Figure 8.7: *Schematic overview of the S^3-LEB.*

and efficiency [96]. The atoms of interest are resonantly ionized inside the gas jet by laser beams coming from transversal and anti-collinear directions.

The photo-ions are drag by a linear DC gradient on top of the RF voltage of the S-shape RFQ (SRFQ), extracting the ions from the jet. In addition, the SRFQ actuates as a primary differential pumping section 10^{-2}-10^{-1} mbar at the entrance, against 10^{-4}-10^{-3} mbar at the exit. The high vacuum (10^{-8}-10^{-7} mbar) is achieved after the mini-RFQ (mRFQ), which purpose is to maximize the transmission between the different vacuum regions.

To remove some remaining contaminants from the laser ionized beam a quadrupole mass filter (QMF) is located before the RFQ cooler buncher. As the IGISOL cooler-buncher (section 4.1), in order to perform precision measurements, the ions are cooled by helium gas collisions to minimize the longitudinal and transversal emittance of the beam and bunched using a potential well.

After the extraction of the RFQ cooler buncher the ions are post-accelerated by a 3 kV potential generated by a pulse up drift tube. The ion beam energy is designed for optimal injection on the Multi Reflection Time Of Flight Mass Spectrometer (PILGRIM) [151]. Therefore, following the pulse up, the ion beam can be send to PILGRIM for mass measurement or alternatively for purification before sending it to the future decay spectroscopy station called Spectroscopy Electron Alpha in Silicon bOx couNter (SEASON) or towards the future DESIR facility [152].

The S^3-LEB can be used to perform high resolution laser spectroscopy combined with mass and/or decay measurements or to provide beams for precision measurements for different detector systems at DESIR.

For the experiments at S^3-LEB, efficient RIS schemes are needed in order to take profit of the S^3 production rates. In addition, high sensitivity to the nuclear parameters is desired to extract the nuclear observables with good resolution.

Off-line measurements had been carried at GISELE (see section 4.3) in order to test and develop RIS for the S^3-LEB day-one cases [118]. A study of the N=Z region around ^{100}Sn will be performed. Alongside these elements, Pd has been considered as one of the proposed cases and the offline work for the preparation was performed at GISELE.

8.2.1 Test and development of RIS

The purpose of the GISELE laboratory has evolved from a resonant ionization laser ion source [117] to a offline laboratory to study resonant ionization scheme for the S^3-LEB elements of interest [118]. In this context, laser ionization spectroscopy measurements have been performed on stable palladium atoms generated by an ABU. Details about the laboratory are presented at section 4.3

Previous this work, development and testing of highly efficient excitation schemes for resonance ionization of palladium was carried out at the RISIKO mass separator of the institute for physics of Mainz University [127]. Three RIS schemes developed are presented at Figure 8.8.

The three step scheme, Figure 8.8 C, is the RIS scheme used during the palladium in-source production test (see section 4.2). Consequently, it has been the first scheme studied. The sensitivity to nuclear observables of the first step 276nm transition has been studied using the broadband Ti:sapphire cavities with a single etalon and the NB single mode injection cavity.

The saturation curves for this RIS scheme are shown at Figure 8.9. The saturation powers for the first and second steps are in agreement with the literature values [127]. Regarding the ionization step, the saturation power is in disagreement, probably because it never fully saturates.

In order to study the isotope shift and hyperfine structure, a NB laser injection cavity has been used to study the 276 nm first step transition. Before the measure-

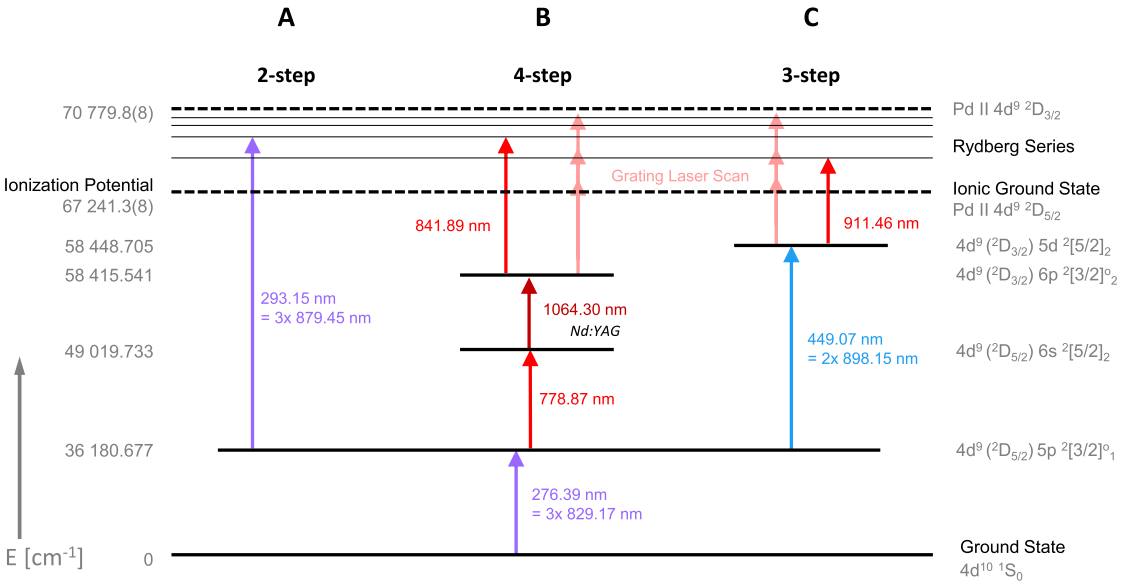

Figure 8.8: *Pd excitation schemes. [127]*

ment, the voltages of the electrodes inside the ABU have been optimized to obtain the maximum mass separation through the TOF tube. To obtain the frequency spectra a gate is applied on the TOF signal of the isotope of interest, as is shown on Figure 8.10.

The experimental data has been fitted with a Voigt profile function by the SATLAS package [131]. The isotope shift has been calculated as the weighted mean from the shift respect ^{108}Pd on seven different measurements (Figure 8.11) and the statistical error σ arises from the standard error of the SATLAS fit scaled with the reduced χ-square (see Equation 6.2 and Equation 6.3).

Table 8.1: *Measured isotopes shift for the $4d^{10}\,^1S_0$-$4d^9 5p^3\,^1P_1$ transition, using ^{108}Pd as reference isotope.*

Isotope	This work (MHz)	Literature [153] (MHz)
102	215(6)	-
104	145(5)	-
105	78(6)	-
106	66(5)	62.7(5)
110	-67(5)	-66.4(13)

The mass and field shift has been extracted using the King Plot technique (Figure 8.12). The field shift (0.5(17) GHz/fm^2) has been found to be almost six times

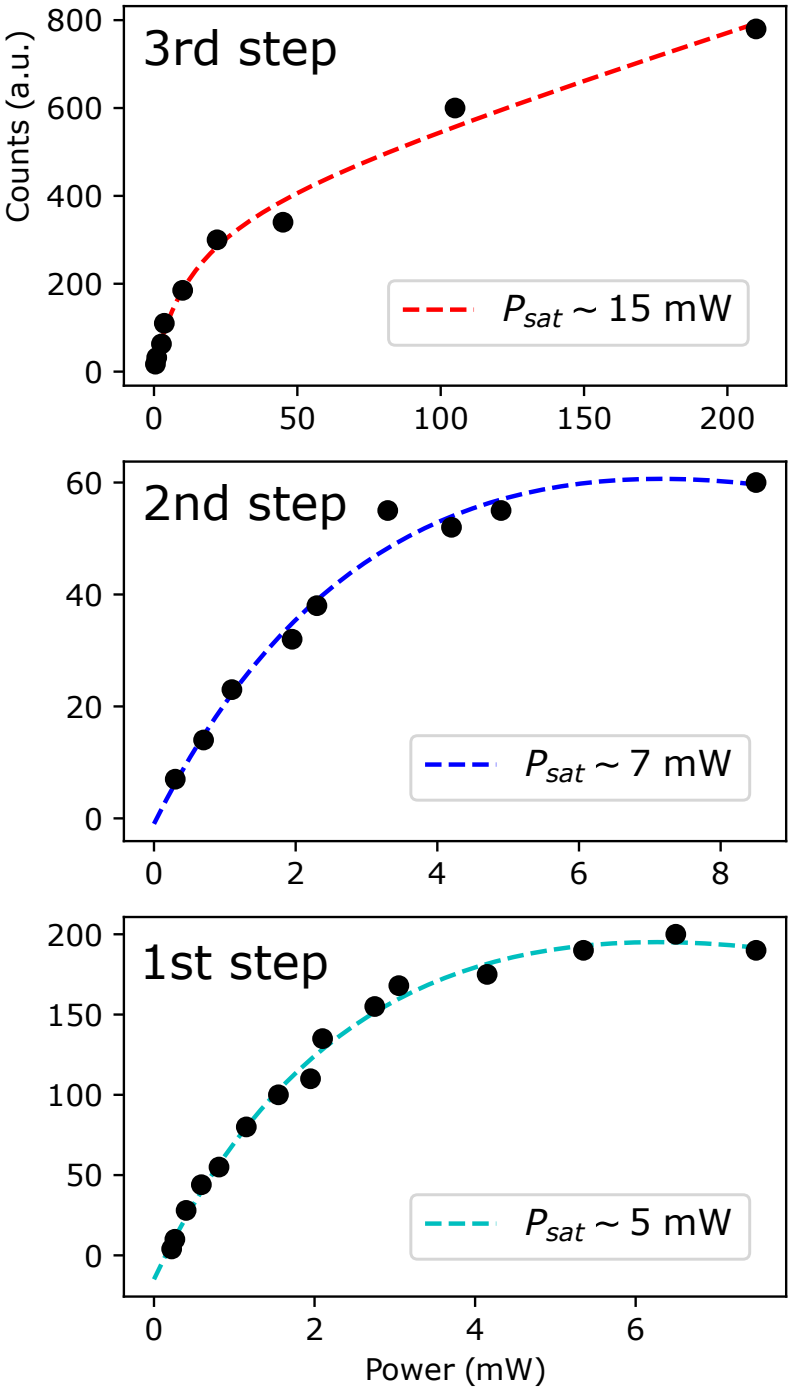

Figure 8.9: *Saturation curves RIS scheme C using broadband lasers.*

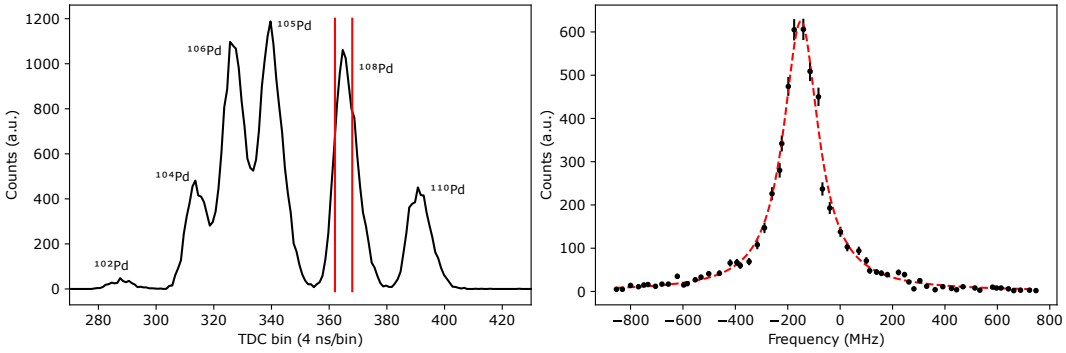

Figure 8.10: *TOF gate to obtain the frequency spectra of ^{108}Pd. Left: Time-of-Flight and gate (red lines) applied to extract the ^{108}Pd frequency spectra. Right: ^{108}Pd 276 nm resonance.*

smaller than the field shift from the 363 nm transition used for the collinear experiment (-2.9(6) GHz/fm^2). As a result, the sensitivity for measuring the mean-square charge radii will be also small.

The hyperfine parameters has been obtained by fitting the hyperfine splitting of ^{105}Pd isotope. The atomic spin of the states on the studied transition are $J = 0 \longrightarrow J = 1$, therefore the structure will be composed by three resonances, according to the selection rules presented at subsection 3.2.2.

Table 8.2: *Measured A and B hyperfine parameters of ^{105}Pd for the $4d^{10}\,^1S_0$-$4d^9 5p\,^3P_1$ transition.*

Hyperfine parameter	**This work (MHz)**	**Literature [153] (MHz)**
A	-127(3)	-126.9(6)
B	4(4)	2.0(9)

The selected transition has a small field shit and hyperfine parameter B. Consequently, the extraction of the mean-square charge radii and quadrupole spectroscopic moment will be hindered by the low sensitivity.

In order to have a good understanding on the evolution of deformation on the palladium isotopic chain is necessary to measure a different transition. To select the new transition, several aspects have to be considered. From one hand, using the atomic beam unit (ABU), it is not possible to populate isomeric atomic states, as a result, the first transition on the RIS scheme has to be from the atomic ground state.

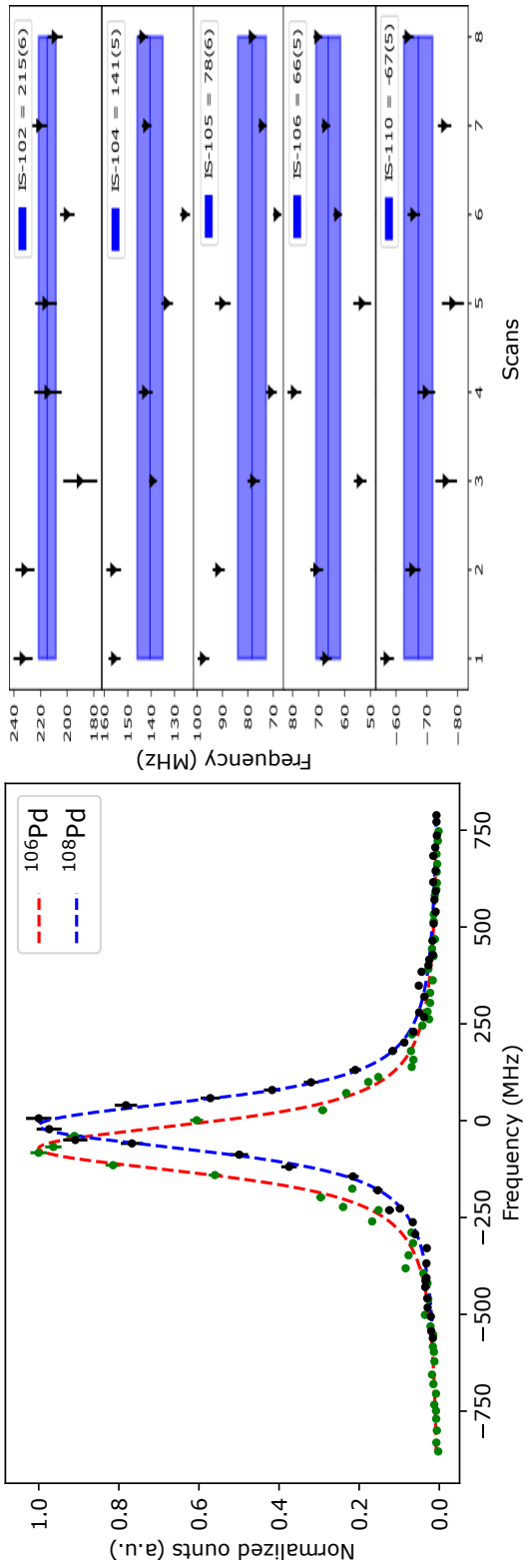

Figure 8.11: *Measured isotope shift from the first step 276 nm transition. Left: Shift between the ^{106}Pd and ^{108}Pd resonances. Right: Isotope shift measured on 7 scans using ^{108}Pd as reference isotope.*

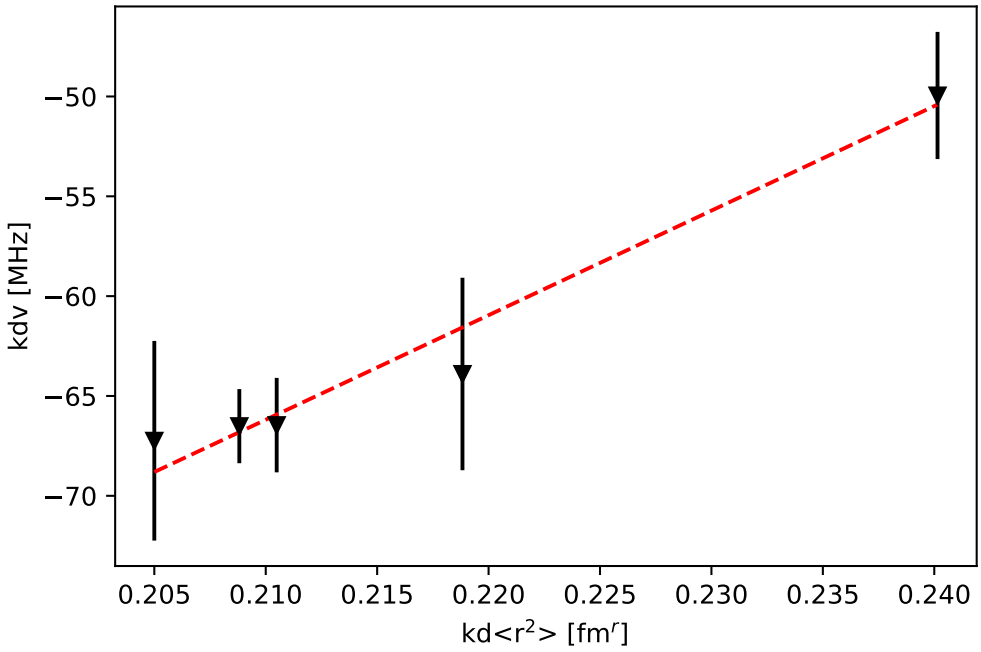

Figure 8.12: *King Plot - 276 nm transition. M = -0.176(81) GHz amu, F = 0.5(17) GHz/fm^2.*

From the other hand, palladium has only three transitions from its atomic ground state, being the three previously measured [153]. The literature isotope shifts and hyperfine parameters are presented at Table 8.3.

Table 8.3: *Isotope shifts and hyperfine parameters of Pd transition starting from the ground state.*

Transition	$\delta\nu^{108-106}$ **[153] (MHz)**	**A [153] (MHz)**	**B [153] (MHz)**
$4d^{10}\ {}^1S_0 \longrightarrow 4d^9 5p\ {}^3P_1$	62.7(5)	-126.9(6)	2.0(9)
$4d^{10}\ {}^1S_0 \longrightarrow 4d^9 5p\ {}^3D_1$	45(6)	-212(5)	-57(8)
$4d^{10}\ {}^1S_0 \longrightarrow 4d^9 5p\ {}^1P_1$	44(3)	-300(1)	-215.5(8)

As can be shown at Table 8.3, all transitions from the atomic ground state have a small isotope shift.

To overcome the problematic of the sensitivity and benefit from the highly efficient excitation schemes developed at RISIKO (Figure 8.8), second step transitions were

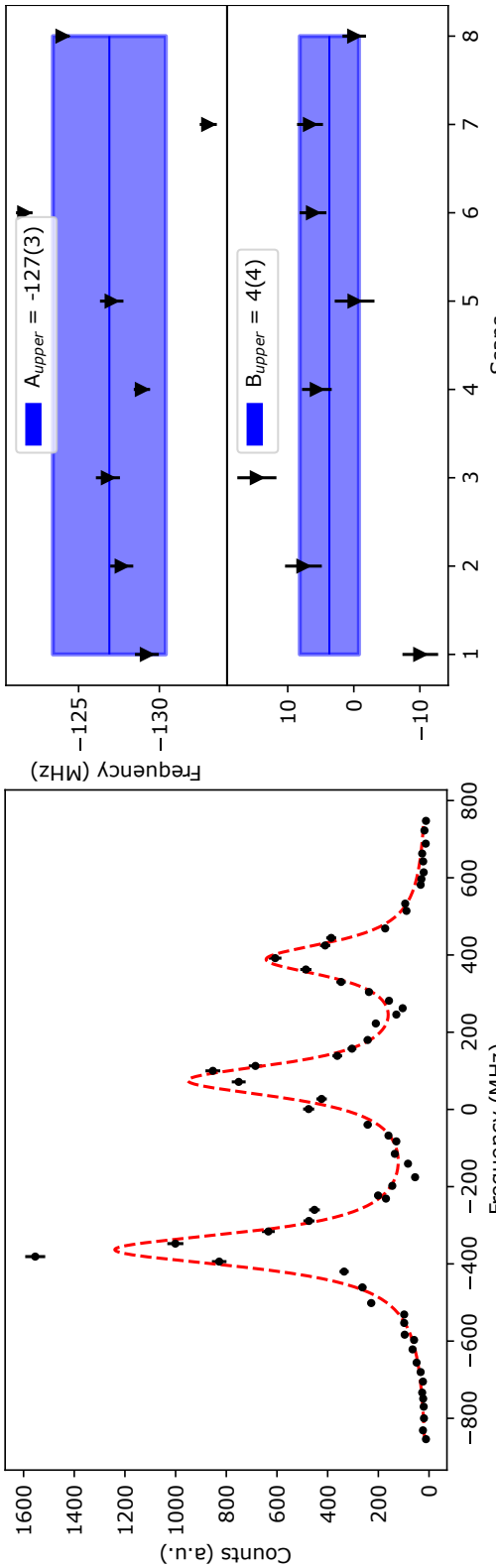

Figure 8.13: *Hyperfine structure from the* $4d^{10}1S_0$-$4d^9 5p^3P_1$ *transition on* ^{105}Pd.

proposed to be studied. From the available transitions, s to p atomic transitions are expected to be more sensitive to the isotope shift as the electron wave function has higher probability of been inside the nucleus (see section 3.2.1). Accordingly, the 779 nm transition on scheme B at Figure 8.8 will be studied at the GISELE laboratory.

The third step of the RIS scheme is not accessible at GISELE due to the lack of a 1064 Nd:YAG laser. Therefore, a new three step resonant ionization scheme was search to maintain the first two steps intact, but using a transition directly from the 49019.733 cm^{-1} level to a Rydberg state.

Rydberg states on palladium atom have been previously studied [154, 155]. Several wavelength scans were performed covering the regions where Rydberg states with odd parity were expected. A Rydeberg state was found at 59651.1 cm^{-1}, completing the RIS scheme.

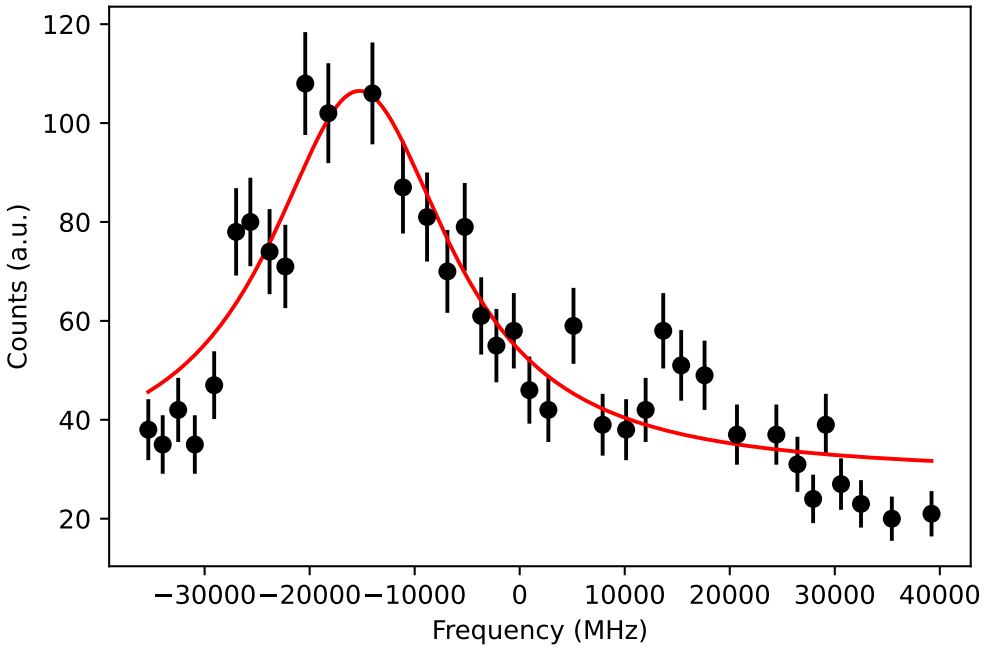

Figure 8.14: *Resonant ionization through the 59651.1 cm^{-1} Rydberg state.*

Chapter 9

Outlook

The collinear laser spectroscopy measurements presented at this thesis have been the first time laser spectroscopy has been performed on radioactive Pd isotopes. Reference [134] published the charge radii and compared the results to nuclear DFT calculations Skyrme and Fayans. This thesis has gone a step forward on the study of deformation on palladium isotopes thanks to the extraction of the electromagnetic moments and the addition of ^{113}Pd ground state and ^{115}Pd ground and isomeric states.

This present work has establish unambiguously the spins assignments for the ground states of ^{99,113,115}Pd and the isomeric state of ^{115}Pd. The comparison with theoretical Fayans and Gogny calculations indicate softness on palladium isotopes, and triaxiality have been suggested on the neutron rich region. In addition, an analysis on the odd-even staggering has delve into the idea that odd-even staggering is influenced by other mechanism than pairing.

This results shed light on the uncharted refractory region. In order to keep this progress, first steps have been taken for future measurements towards the proton drip line. A production test have been performed using resonant ionisation laser spectroscopy in a hot cavity catcher. According to the measured efficiencies and taken into account the transmission until the Penning trap, the hot cavity measurements is expected to cross the N=50 shell closure and puss towards the N=Z line.

The limited resolution of the hot cavity will be complemented by the future in-gas jet laser spectroscopy measurements on the S^3-Low Energy Branch. Recent rate estimates provided by S^3 prove the possibility of measuring palladium beyond the

N=Z line. For this purpose, offline studies have been performed on palladium RIS in order to find a scheme with high sensibility to the nuclear observables. In addition, optical developments have been performed in order to enhance the performance of the GISELE laser laboratory.

Bibliography

[1] P. Stránskỳ, A. Frank, and R. Bijker, "On prolate shape predominance in nuclear deformation," in *Journal of Physics: Conference Series*, vol. 322, p. 012018, IOP Publishing, 2011.

[2] J. Gundlach, K. Snover, J. Behr, C. Gossett, M. Kicinska-Habior, and K. Lesko, "Oblate deformed shapes of hot rotating nuclei deduced from giant-dipole-resonance decay studies," *Physical review letters*, vol. 65, no. 20, p. 2523, 1990.

[3] P. A. Butler, L. Gaffney, P. Spagnoletti, K. Abrahams, M. Bowry, J. Cederkäll, G. De Angelis, H. De Witte, P. Garrett, A. Goldkuhle, *et al.*, "Evolution of octupole deformation in radium nuclei from coulomb excitation of radioactive ra 222 and ra 228 beams," *Physical review letters*, vol. 124, no. 4, p. 042503, 2020.

[4] R. K. Gupta, S. Singh, G. Münzenberg, and W. Scheid, "Neutron-halo nuclei in cold synthesis and cluster decay of heavy nuclei: Z= 104 nucleus as an example," *Physical Review C*, vol. 51, no. 5, p. 2623, 1995.

[5] K. Heyde and J. L. Wood, "Shape coexistence in atomic nuclei," *Reviews of Modern Physics*, vol. 83, no. 4, p. 1467, 2011.

[6] B. Marsh, T. D. Goodacre, S. Sels, Y. Tsunoda, B. Andel, A. Andreyev, N. Althubiti, D. Atanasov, A. Barzakh, J. Billowes, *et al.*, "Characterization of the shape-staggering effect in mercury nuclei," *Nature Physics*, vol. 14, no. 12, pp. 1163–1167, 2018.

[7] P. Campbell, I. Moore, and M. Pearson, "Laser spectroscopy for nuclear structure physics," *Progress in Particle and Nuclear Physics*, vol. 86, pp. 127–180, 2016.

[8] K. Krane and D. Halliday, "Introductory nuclear physics, wi¬ ley," *New York*, p. 169, 1988.

[9] J. W. Negele, "The mean-field theory of nuclear structure and dynamics," *Reviews of Modern Physics*, vol. 54, no. 4, p. 913, 1982.

[10] R. Casten and R. F. Casten, *Nuclear structure from a simple perspective*, vol. 23. Oxford University Press on Demand, 2000.

[11] M. G. Mayer, "On closed shells in nuclei. ii," *Physical Review*, vol. 75, no. 12, p. 1969, 1949.

[12] E. Caurier, G. Martínez-Pinedo, F. Nowacki, A. Poves, and A. Zuker, "The shell model as a unified view of nuclear structure," *Reviews of modern Physics*, vol. 77, no. 2, p. 427, 2005.

[13] D. R. Hartree, "The wave mechanics of an atom with a non-coulomb central field. part ii. some results and discussion," in *Mathematical Proceedings of the Cambridge Philosophical Society*, vol. 24, pp. 111–132, Cambridge University Press, 1928.

[14] V. Fock, "Näherungsmethode zur lösung des quantenmechanischen mehrkörperproblems," *Zeitschrift für Physik*, vol. 61, no. 1, pp. 126–148, 1930.

[15] J. MacDonald, "Successive approximations by the rayleigh-ritz variation method," *Physical Review*, vol. 43, no. 10, p. 830, 1933.

[16] J. C. Slater, "A simplification of the hartree-fock method," *Physical review*, vol. 81, no. 3, p. 385, 1951.

[17] P. Hodgson, "Effective mass in nuclei," *Contemporary Physics*, vol. 24, no. 5, pp. 491–503, 1983.

[18] G. Colò, "Density functional theory (dft) for atomic nuclei: a simple introduction," in *Proceedings of the International School of Physics "Enrico Fermi*, vol. 201, pp. 95–128, 2019.

[19] J. Dechargé and D. Gogny, "Hartree-fock-bogolyubov calculations with the d 1 effective interaction on spherical nuclei," *Physical Review C*, vol. 21, no. 4, p. 1568, 1980.

[20] T. Skyrme, "The effective nuclear potential," *Nuclear Physics*, vol. 9, no. 4, pp. 615–634, 1958.

[21] P.-G. Reinhard and H. Flocard, "Nuclear effective forces and isotope shifts," *Nuclear Physics A*, vol. 584, no. 3, pp. 467–488, 1995.

[22] S. Fayans, E. Trykov, and D. Zawischa, "Influence of effective spin-orbit interaction on the collective states of nuclei," *Nuclear Physics A*, vol. 568, no. 3, pp. 523–543, 1994.

[23] S. Fayans, "Towards a universal nuclear density functional," *Journal of Experimental and Theoretical Physics Letters*, vol. 68, no. 3, pp. 169–174, 1998.

[24] P.-G. Reinhard and W. Nazarewicz, "Toward a global description of nuclear charge radii: Exploring the fayans energy density functional," *Physical Review C*, vol. 95, no. 6, p. 064328, 2017.

[25] S. Fayans, S. Tolokonnikov, E. Trykov, and D. Zawischa, "Nuclear isotope shifts within the local energy-density functional approach," *Nuclear Physics A*, vol. 676, no. 1-4, pp. 49–119, 2000.

[26] A. J. Miller, K. Minamisono, A. Klose, D. Garand, C. Kujawa, J. Lantis, Y. Liu, B. Maaß, P. Mantica, W. Nazarewicz, *et al.*, "Proton superfluidity and charge radii in proton-rich calcium isotopes," *Nature physics*, vol. 15, no. 5, pp. 432–436, 2019.

[27] A. Goodman, G. Struble, J. Bar-Touv, and A. Goswami, "Generalized pairing in light nuclei. ii. solution of the hartree-fock-bogoliubov equations with realistic forces and comparison of different approximations," *Physical Review C*, vol. 2, no. 2, p. 380, 1970.

[28] J. Erler, P. Klüpfel, and P.-G. Reinhard, "A stabilized pairing functional," *The European Physical Journal A*, vol. 37, no. 1, pp. 81–86, 2008.

[29] P. Klüpfel, P.-G. Reinhard, T. J. Bürvenich, and J. A. Maruhn, "Variations on a theme by skyrme: A systematic study of adjustments of model parameters," *Phys. Rev. C*, vol. 79, p. 034310, Mar 2009.

[30] M. Hammen, W. Nörtershäuser, D. Balabanski, M. Bissell, K. Blaum, I. Budinčević, B. Cheal, K. Flanagan, N. Frömmgen, G. Georgiev, *et al.*, "From calcium to cadmium: Testing the pairing functional through charge radii measurements of cd 100- 130," *Physical review letters*, vol. 121, no. 10, p. 102501, 2018.

[31] M. Stoitsov, N. Schunck, M. Kortelainen, N. Michel, H. Nam, E. Olsen, J. Sarich, and S. Wild, "Axially deformed solution of the skyrme-hartree–fock–bogoliubov equations using the transformed harmonic oscillator basis (ii) hfbtho v2. 00d: A new version of the program," *Computer Physics Communications*, vol. 184, no. 6, pp. 1592–1604, 2013.

[32] J.-F. Berger, J.-P. Blaizot, D. Bouche, P. Chaix, J.-P. Delaroche, M. Dupuis, M. Girod, J. Gogny, B. Grammaticos, D. Iracane, *et al.*, "Daniel gogny," *The European Physical Journal A*, vol. 53, no. 10, pp. 1–9, 2017.

[33] D. Brink and E. Boeker, "Effective interactions for hartree-fock calculations," *Nuclear Physics A*, vol. 91, no. 1, pp. 1–26, 1967.

[34] L. Robledo, T. Rodríguez, and R. Rodríguez-Guzmán, "Mean field and beyond description of nuclear structure with the gogny force: a review," *Journal of Physics G: Nuclear and Particle Physics*, vol. 46, no. 1, p. 013001, 2018.

[35] D. Gogny, "Self-consistent pairing calculations," tech. rep., CEA Centre d'Etudes de Bruyeres-le-Chatel, 1975.

[36] J. Berger, M. Girod, and D. Gogny, "Microscopic analysis of collective dynamics in low energy fission," *Nuclear Physics A*, vol. 428, pp. 23–36, 1984.

[37] F. Chappert, M. Girod, and S. Hilaire, "Towards a new gogny force parameterization: Impact of the neutron matter equation of state," *Physics Letters B*, vol. 668, no. 5, pp. 420–424, 2008.

[38] S. Goriely, S. Hilaire, M. Girod, and S. Péru, "First gogny-hartree-fock-bogoliubov nuclear mass model," *Physical review letters*, vol. 102, no. 24, p. 242501, 2009.

[39] T. R. Rodríguez, A. Arzhanov, and G. Martínez-Pinedo, "Toward global beyond-mean-field calculations of nuclear masses and low-energy spectra," *Physical Review C*, vol. 91, no. 4, p. 044315, 2015.

[40] C. W. Wong, "Generator-coordinate methods in nuclear physics," *Physics Reports*, vol. 15, no. 5, pp. 283–357, 1975.

[41] T. R. Rodriguez, "Structure of krypton isotopes calculated with symmetry-conserving configuration-mixing methods," *Physical Review C*, vol. 90, no. 3, p. 034306, 2014.

[42] V. Paar, "A parabolic rule for the energy dependence on x= i (i+ 1) for proton-neutron multiplets in odd-odd nuclei," *Nuclear Physics A*, vol. 331, no. 1, pp. 16–28, 1979.

[43] E. Rutherford, "Lxxix. the scattering of α and β particles by matter and the structure of the atom," *The London, Edinburgh, and Dublin Philosophical Magazine and Journal of Science*, vol. 21, no. 125, pp. 669–688, 1911.

[44] G. Fricke, K. Heilig, and H. F. Schopper, "Nuclear charge radii," 2004.

[45] P.-G. Reinhard, W. Nazarewicz, and R. G. Ruiz, "Beyond the charge radius: the information content of the fourth radial moment," *Physical Review C*, vol. 101, no. 2, p. 021301, 2020.

[46] E. Seltzer, "K x-ray isotope shifts," *Physical Review*, vol. 188, no. 4, p. 1916, 1969.

[47] T. Schmidt, "Über die magnetischen momente der atomkerne," *Zeitschrift für Physik*, vol. 106, no. 5, pp. 358–361, 1937.

[48] P. Ring and P. Schuck, *The nuclear many-body problem*. Springer Science & Business Media, 2004.

[49] E. Clément, "Shape coexistence in neutron-deficient krypton and selenium isotopes studied by low-energy coulomb excitation of radioactive ion beams," *Theses, Université Paris Sud-Paris XI*, 2006.

[50] D. Zawischa, "On the origin of odd-even-staggering of nuclear charge radii," *Physics Letters B*, vol. 155, no. 5-6, pp. 309–312, 1985.

[51] S. Ahmad, W. Klempt, R. Neugart, E. Otten, P.-G. Reinhard, G. Ulm, K. Wendt, I. Collaboration, *et al.*, "Mean square charge radii of radium isotopes and octupole deformation in the 220–228ra region," *Nuclear Physics A*, vol. 483, no. 2, pp. 244–268, 1988.

[52] T. D. Goodacre, A. Afanasjev, A. Barzakh, B. Marsh, S. Sels, P. Ring, H. Nakada, A. Andreyev, P. Van Duppen, N. Althubiti, *et al.*, "Laser spectroscopy of neutron-rich hg 207, 208 isotopes: Illuminating the kink and odd-even staggering in charge radii across the n= 126 shell closure," *Physical Review Letters*, vol. 126, no. 3, p. 032502, 2021.

[53] U. C. Perera, A. Afanasjev, and P. Ring, "Charge radii in covariant density functional theory: a global view," *Physical Review C*, vol. 104, no. 6, p. 064313, 2021.

[54] H. Grawe, A. Blazhev, M. Górska, R. Grzywacz, H. Mach, and I. Mukha, "Nuclear structure far off stability–implications for nuclear astrophysics," *The European Physical Journal A-Hadrons and Nuclei*, vol. 27, no. 1, pp. 257–267, 2006.

[55] B. Cederwall, F. G. Moradi, T. Bäck, A. Johnson, J. Blomqvist, E. Clément, G. De France, R. Wadsworth, K. Andgren, K. Lagergren, *et al.*, "Evidence

for a spin-aligned neutron–proton paired phase from the level structure of 92pd," *Nature*, vol. 469, no. 7328, pp. 68–71, 2011.

[56] C. Hinke, M. Böhmer, P. Boutachkov, T. Faestermann, H. Geissel, J. Gerl, R. Gernhäuser, M. Górska, A. Gottardo, H. Grawe, *et al.*, "Superallowed gamow–teller decay of the doubly magic nucleus 100sn," *Nature*, vol. 486, no. 7403, pp. 341–345, 2012.

[57] I. Talmi, "On the odd-even effect in the charge radii of isotopes," *Nuclear Physics A*, vol. 423, no. 2, pp. 189–196, 1984.

[58] M. Reponen, R. de Groote, L. Al Ayoubi, O. Beliuskina, M. Bissell, P. Campbell, L. Cañete, B. Cheal, K. Chrysalidis, C. Delafosse, *et al.*, "Evidence of a sudden increase in the nuclear size of proton-rich silver-96," *Nature Communications*, vol. 12, no. 1, pp. 1–8, 2021.

[59] F. Charlwood, K. Baczynska, J. Billowes, P. Campbell, B. Cheal, T. Eronen, D. Forest, A. Jokinen, T. Kessler, I. Moore, *et al.*, "Nuclear charge radii of molybdenum fission fragments," *Physics Letters B*, vol. 674, no. 1, pp. 23–27, 2009.

[60] B. Cheal, K. Baczynska, J. Billowes, P. Campbell, F. Charlwood, T. Eronen, D. Forest, A. Jokinen, T. Kessler, I. Moore, *et al.*, "Laser spectroscopy of niobium fission fragments: first use of optical pumping in an ion beam cooler buncher," *Physical review letters*, vol. 102, no. 22, p. 222501, 2009.

[61] P. Campbell, H. Thayer, J. Billowes, P. Dendooven, K. Flanagan, D. Forest, J. Griffith, J. Huikari, A. Jokinen, R. Moore, *et al.*, "Laser spectroscopy of cooled zirconium fission fragments," *Physical review letters*, vol. 89, no. 8, p. 082501, 2002.

[62] J. Äystö, C. Davids, J. Hattula, J. Honkanen, K. Honkanen, P. Jauho, R. Julin, S. Juutinen, J. Kumpulainen, T. Lönnroth, A. Pakkanen, A. Passoja, H. Penttilä, P. Taskinen, E. Verho, A. Virtanen, and M. Yoshii, "Levels in 110pd, 112pd, 114pd and 116pd from the beta decays of the on-line mass separated rh isotopes," *Nuclear Physics A*, vol. 480, no. 1, pp. 104–124, 1988.

[63] M. Houry, R. Lucas, M.-G. Porquet, C. Theisen, M. Girod, M. Aiche, M. M. Aleonard, A. Astier, G. Barreau, F. Becker, J. F. Chemin, I. Deloncle, T. P. Doan, J. L. Durell, K. Hauschild, W. Korten, Y. Le Coz, M. J. Leddy, S. Perries, N. Redon, A. A. Roach, J. N. Scheurer, A. G. Smith, and B. J. Varley, "Structure of neutron rich palladium isotopes produced in heavy ion induced fission," *The European Physical Journal A - Hadrons and Nuclei*, vol. 6, pp. 43–48, Sep 1999.

[64] P. Sarriguren, "β-decay properties of neutron-rich ge, se, kr, sr, ru, and pd isotopes from deformed quasiparticle random-phase approximation," *Physical Review C*, vol. 91, no. 4, p. 044304, 2015.

[65] R. Aryaeinejad, J. D. Cole, R. C. Greenwood, S. S. Harrill, N. P. Lohstreter, K. Butler-Moore, S. Zhu, J. H. Hamilton, A. V. Ramayya, X. Zhao, W. C. Ma, J. Kormicki, J. K. Deng, W. B. Gao, I. Y. Lee, N. R. Johnson, F. K. McGowan, G. Ter-Akopian, and Y. Oganessian, "Band crossing observed in neutron-rich pd isotopes via spontaneous fission of ^{252}Cf," *Phys. Rev. C*, vol. 48, pp. 566–573, Aug 1993.

[66] T. Naz, G. Bhat, S. Jehangir, S. Ahmad, and J. Sheikh, "Microscopic description of structural evolution in pd, xe, ba, nd, sm, gd and dy isotopes," *Nuclear Physics A*, vol. 979, pp. 1–20, 2018.

[67] B. Fogelberg, Y. Zongyuan, B. Ekström, E. Lund, K. Aleklett, and L. Sihver, "Isomerism, total decay energies, and absolute γ-ray intensities of the heavy pd and ag isotopes," *Zeitschrift für Physik A Atomic Nuclei*, vol. 337, pp. 251–255, Sep 1990.

[68] W. Urban, A. Złomaniec, G. Simpson, J. Pinston, J. Kurpeta, T. Rzaca-Urban, J. Durell, A. Smith, B. Varley, N. Schulz, *et al.*, "New spins for ground states and isomers in 115pd and 117pd," *The European Physical Journal A-Hadrons and Nuclei*, vol. 22, no. 2, pp. 157–161, 2004.

[69] D. Fong, J. K. Hwang, A. V. Ramayya, J. H. Hamilton, Y. X. Luo, P. M. Gore, E. F. Jones, W. B. Walters, J. O. Rasmussen, M. A. Stoyer, S. J. Zhu, I. Y. Lee, A. O. Macchiavelli, S. C. Wu, A. V. Daniel, G. M. Ter-Akopian, Y. T. Oganessian, J. D. Cole, R. Donangelo, and W. C. Ma, "Negative parity bands of ^{115}Pd and band structures in ^{113,115,117}Pd," *Phys. Rev. C*, vol. 72, p. 014315, Jul 2005.

[70] W. Demtröder, *Atoms, molecules and photons*, vol. 3. Springer, 2010.

[71] E. Schrödinger, "An undulatory theory of the mechanics of atoms and molecules," *Physical review*, vol. 28, no. 6, p. 1049, 1926.

[72] A. Sommerfeld, "Zur quantentheorie der spektrallinien," *Annalen der Physik*, vol. 356, no. 17, pp. 1–94, 1916.

[73] R. Glass and A. Hibbert, "Relativistic effects in many electron atoms," *Computer Physics Communications*, vol. 16, no. 1, pp. 19–34, 1978.

[74] L. H. Thomas, "The motion of the spinning electron," *Nature*, vol. 117, no. 2945, pp. 514–514, 1926.

[75] W. H. King, *Isotope shifts in atomic spectra*. Springer Science & Business Media, 2013.

[76] I. Tupitsyn, V. Shabaev, J. C. López-Urrutia, I. Draganić, R. S. Orts, and J. Ullrich, "Relativistic calculations of isotope shifts in highly charged ions," *Physical Review A*, vol. 68, no. 2, p. 022511, 2003.

[77] E. C. SELTZER, "k x-ray isotope shifts," *Phys. Rev.*, vol. 188, pp. 1916–1919, Dec 1969.

[78] L. Vazquez Rodriguez, *Laser spectroscopy of tin across N= 82*. PhD thesis, Université Paris-Saclay (ComUE), 2018.

[79] S. Geldhof, "Developments for high-resolution laser spectroscopy and application to palladium isotopes," *JYU dissertations*, 2020.

[80] V. Gerginov, A. Derevianko, and C. E. Tanner, "Observation of the nuclear magnetic octupole moment of c s 133," *Physical Review Letters*, vol. 91, no. 7, p. 072501, 2003.

[81] R. de Groote, S. Kujanpää, Á. Koszorús, J. Li, and I. Moore, "Magnetic octupole moment of yb 173 using collinear laser spectroscopy," *Physical Review A*, vol. 103, no. 3, p. 032826, 2021.

[82] A. Bohr and V. Weisskopf, "The influence of nuclear structure on the hyperfine structure of heavy elements," *Physical Review*, vol. 77, no. 1, p. 94, 1950.

[83] J. E. Rosenthal and G. Breit, "The isotope shift in hyperfine structure," *Physical Review*, vol. 41, no. 4, p. 459, 1932.

[84] M. Crawford and A. Schawlow, "Electron-nuclear potential fields from hyperfine structure," *Physical Review*, vol. 76, no. 9, p. 1310, 1949.

[85] J. R. Persson, "Table of hyperfine anomaly in atomic systems," *Atomic Data and Nuclear Data Tables*, vol. 99, no. 1, pp. 62–68, 2013.

[86] A. Einstein, "Zur quantentheorie der strahlung," *First published in*, pp. 121–128, 1916.

[87] C. Foot, "Atomic physics, ser," *Oxford Master Series in Atomic, Optical and Laser Physics*, vol. 5, p. 134, 2005.

[88] W. Gins, "Development of a dedicated laser-polarization beamline for isolde-cern," 2019.

[89] M. Reponen, "Resonance laser ionization developments for igisol-4," *Research report/Department of Physics, University of Jyväskylä*, no. 8/2012, 2012.

[90] V. Sonnenschein, "Laser developments and high resolution resonance ionization spectroscopy of actinide elements," *Research report/Department of Physics, University of Jyväskylä*, no. 1/2015, 2014.

[91] G. Neyens, "Nuclear magnetic and quadrupole moments for nuclear structure research on exotic nuclei," *Reports on progress in physics*, vol. 66, no. 4, p. 633, 2003.

[92] P. Jacquinot and R. Klapisch, "Hyperfine spectroscopy of radioactive atoms," *Reports on Progress in Physics*, vol. 42, no. 5, p. 773, 1979.

[93] G. Alkhazov, A. Barzakh, V. Denisov, K. Mezilev, Y. N. Novikov, V. Panteleyev, A. Popov, E. Sudentas, V. Letokhov, V. Mishin, *et al.*, "A new highly efficient method of atomic spectroscopy for nuclides far from stability," *Nuclear Instruments and Methods in Physics Research Section B: Beam Interactions with Materials and Atoms*, vol. 69, no. 4, pp. 517–520, 1992.

[94] Y. Kudryavtsev, R. Ferrer, M. Huyse, P. Van den Bergh, and P. Van Duppen, "The in-gas-jet laser ion source: Resonance ionization spectroscopy of radioactive atoms in supersonic gas jets," *Nuclear Instruments and Methods in Physics Research Section B: Beam Interactions with Materials and Atoms*, vol. 297, pp. 7–22, 2013.

[95] T. Sonoda, T. E. Cocolios, J. Gentens, M. Huyse, O. Ivanov, Y. Kudryavtsev, D. Pauwels, P. Van den Bergh, and P. Van Duppen, "The laser ion source trap (list) coupled to a gas cell catcher," *Nuclear Instruments and Methods in Physics Research Section B: Beam Interactions with Materials and Atoms*, vol. 267, no. 17, pp. 2918–2926, 2009.

[96] R. Ferrer, A. Barzakh, B. Bastin, R. Beerwerth, M. Block, P. Creemers, H. Grawe, R. de Groote, P. Delahaye, X. Fléchard, *et al.*, "Towards high-resolution laser ionization spectroscopy of the heaviest elements in supersonic gas jet expansion," *Nature communications*, vol. 8, no. 1, pp. 1–9, 2017.

[97] J. Ärje, J. Äystö, H. Hyvönen, P. Taskinen, V. Koponen, J. Honkanen, K. Valli, A. Hautojärvi, and K. Vierinen, "The ion guide isotope separator

on-line, igisol," *Nuclear Instruments and Methods in Physics Research Section A: Accelerators, Spectrometers, Detectors and Associated Equipment*, vol. 247, no. 3, pp. 431–437, 1986.

[98] R. Macfarlane, R. Gough, N. Oakey, and D. Torgerson, "The helium-jet recoil transport method," *Nuclear Instruments and Methods*, vol. 73, no. 3, pp. 285–291, 1969.

[99] N. Bohr and J. Lindhard, *Electron capture and loss by heavy ions penetrating through matter*. I kommission hos Munksgaard, 1954.

[100] P. Stevenson, J. Larson, and J. Leary, "Proc. int. conf. on the properties of nuclei far from the region of beta-stability," *CERN 70–30*, vol. 1, p. 143, 1970.

[101] P. Karvonen, I. Moore, T. Sonoda, T. Kessler, H. Penttilä, K. Peräjärvi, P. Ronkanen, and J. Äystö, "A sextupole ion beam guide to improve the efficiency and beam quality at igisol," *Nuclear Instruments and Methods in Physics Research Section B: Beam Interactions with Materials and Atoms*, vol. 266, no. 21, pp. 4794–4807, 2008.

[102] I. Moore, P. Dendooven, and J. Ärje, "The igisol technique—three decades of developments," *Hyperfine interactions*, vol. 223, no. 1, pp. 17–62, 2014.

[103] H. Penttilä, "The layout of the igisol 3 facility," *Hyperfine Interactions*, vol. 223, no. 1, pp. 5–16, 2014.

[104] T. Kessler, I. Moore, Y. Kudryavtsev, K. Peräjärvi, A. Popov, P. Ronkanen, T. Sonoda, B. Tordoff, K. Wendt, and J. Äystö, "Off-line studies of the laser ionization of yttrium at the igisol facility," *Nuclear Instruments and Methods in Physics Research Section B: Beam Interactions with Materials and Atoms*, vol. 266, no. 4, pp. 681–700, 2008.

[105] L. J. Vormawah, M. Vilén, R. Beerwerth, P. Campbell, B. Cheal, A. Dicker, T. Eronen, S. Fritzsche, S. Geldhof, A. Jokinen, S. Kelly, I. D. Moore, M. Reponen, S. Rinta-Antila, S. O. Stock, and A. Voss, "Isotope shifts from collinear laser spectroscopy of doubly charged yttrium isotopes," *Phys. Rev. A*, vol. 97, p. 042504, Apr 2018.

[106] M. Vilén, L. Canete, B. Cheal, A. Giatzoglou, R. de Groote, A. de Roubin, T. Eronen, S. Geldhof, A. Jokinen, A. Kankainen, I. Moore, D. Nesterenko, H. Penttilä, I. Pohjalainen, M. Reponen, and S. Rinta-Antila, "A new off-line ion source facility at igisol," *Nuclear Instruments and Methods in Physics*

Research Section B: Beam Interactions with Materials and Atoms, vol. 463, pp. 382–383, 2020.

[107] A. Nieminen, J. Huikari, A. Jokinen, J. Äystö, P. Campbell, and E. Cochrane, "Beam cooler for low-energy radioactive ions," *Nuclear Instruments and Methods in Physics Research Section A: Accelerators, Spectrometers, Detectors and Associated Equipment*, vol. 469, no. 2, pp. 244–253, 2001.

[108] A. Nieminen, P. Campbell, J. Billowes, D. Forest, J. Griffith, J. Huikari, A. Jokinen, I. Moore, R. Moore, G. Tungate, *et al.*, "On-line ion cooling and bunching for collinear laser spectroscopy," *Physical review letters*, vol. 88, no. 9, p. 094801, 2002.

[109] J. Ketelaer, J. Krämer, D. Beck, K. Blaum, M. Block, K. Eberhardt, G. Eitel, R. Ferrer, C. Geppert, S. George, F. Herfurth, J. Ketter, S. Nagy, D. Neidherr, R. Neugart, W. Nörtershäuser, J. Repp, C. Smorra, N. Trautmann, and C. Weber, "Triga-spec: A setup for mass spectrometry and laser spectroscopy at the research reactor triga mainz," *Nuclear Instruments and Methods in Physics Research Section A: Accelerators, Spectrometers, Detectors and Associated Equipment*, vol. 594, no. 2, pp. 162–177, 2008.

[110] R. de Groote, A. de Roubin, P. Campbell, B. Cheal, C. Devlin, T. Eronen, S. Geldhof, I. Moore, M. Reponen, S. Rinta-Antila, and M. Schuh, "Upgrades to the collinear laser spectroscopy experiment at the igisol," *Nuclear Instruments and Methods in Physics Research Section B: Beam Interactions with Materials and Atoms*, vol. 463, pp. 437–440, 2020.

[111] Sirah, "Datasheet matisse 2 ts," 2017.

[112] R. Kirchner, "On the release and ionization efficiency of catcher-ion-source systems in isotope separation on-line," *Nuclear Instruments and Methods in Physics Research Section B: Beam Interactions with Materials and Atoms*, vol. 70, no. 1, pp. 186–199, 1992.

[113] R. Kirchner and E. Roeckl, "A cathode with long lifetime for operation of ion sources with chemically aggressive vapours," *Nuclear Instruments and Methods*, vol. 127, no. 2, pp. 307–309, 1975.

[114] M. Reponen, I. Moore, I. Pohjalainen, S. Rothe, M. Savonen, V. Sonnenschein, and A. Voss, "An inductively heated hot cavity catcher laser ion source," *Review of Scientific Instruments*, vol. 86, no. 12, p. 123501, 2015.

[115] S. Rothe, T. D. Goodacre, D. Fedorov, V. Fedosseev, B. Marsh, P. Molkanov, R. Rossel, M. Seliverstov, M. Veinhard, and K. Wendt, "Laser ion beam production at cern-isolde: New features–more possibilities," *Nuclear Instruments and Methods in Physics Research Section B: Beam Interactions with Materials and Atoms*, vol. 376, pp. 91–96, 2016.

[116] T. Eronen, V. Kolhinen, V.-V. Elomaa, D. Gorelov, U. Hager, J. Hakala, A. Jokinen, A. Kankainen, P. Karvonen, S. Kopecky, *et al.*, "Jyfltrap: a penning trap for precision mass spectroscopy and isobaric purification," in *Three decades of research using IGISOL technique at the University of Jyväskylä*, pp. 61–81, Springer, 2012.

[117] N. Lecesne, R. Alvès-Condé, E. Coterreau, F. De Oliveira, M. Dubois, J. Flambard, H. Franberg, T. Gottwald, P. Jardin, J. Lassen, *et al.*, "Gisele: A resonant ionization laser ion source for the production of radioactive ions at ganil," *Review of Scientific Instruments*, vol. 81, no. 2, p. 02A910, 2010.

[118] J. Romans, A. Ajayakumar, M. Authier, F. Boumard, L. Caceres, J.-F. Cam, A. Claessens, S. Damoy, P. Delahaye, P. Desrues, *et al.*, "First offline results from the s3 low-energy branch," *Atoms*, vol. 10, no. 1, p. 21, 2022.

[119] A. White, "Frequency stabilization of gas lasers," *IEEE Journal of Quantum Electronics*, vol. 1, no. 8, pp. 349–357, 1965.

[120] J. Romans *KULeuven PhD Thesis*, 2022.

[121] S. Raeder, R. Ferrer, C. Granados, M. Huyse, T. Kron, Y. Kudryavtsev, N. Lecesne, J. Piot, J. Romans, H. Savajols, *et al.*, "Performance of dye and ti: sapphire laser systems for laser ionization and spectroscopy studies at s3," *Nuclear Instruments and Methods in Physics Research Section B: Beam Interactions with Materials and Atoms*, vol. 463, pp. 86–95, 2020.

[122] "Bsf10-b - Ø1" uvfs beam sampler for beam pick-off, arc: 650-1050 nm, 5mm thick."

[123] "Pa44m3kw - piezo ring chip, 150 v, 3.9 µm displacement, 15.0 mm od, 9.0 mm id, 3.2 mm long, pre-attached wires."

[124] C. Fabry, "Theorie et applications d'une nouvelle methods de spectroscopie intereferentielle," *Ann. Chim. Ser. 7*, vol. 16, pp. 115–144, 1899.

[125] S. Geldhof, S. El Youbi, I. Moore, I. Pohjalainen, V. Sonnenschein, R. Terabayashi, and A. Voss, "Development of a saturated absorption spectroscopy setup at igisol for characterisation of fabry-pérot interferometers," *Hyperfine Interactions*, vol. 238, no. 1, pp. 1–12, 2017.

[126] M. Reponen, I. Moore, I. Pohjalainen, V. Sonnenschein, and A. Jokinen, "The furios laser ion source at igisol-4," *Nuclear Instruments and Methods in Physics Research Section B: Beam Interactions with Materials and Atoms*, vol. 317, pp. 422–425, 2013.

[127] T. Kron, Y. Liu, S. Richter, F. Schneider, and K. Wendt, "High efficiency resonance ionization of palladium with ti: sapphire lasers," *Journal of Physics B: Atomic, Molecular and Optical Physics*, vol. 49, no. 18, p. 185003, 2016.

[128] W. Zhao, J. Simsarian, L. A. Orozco, and G. Sprouse, "A computer-based digital feedback control of frequency drift of multiple lasers," *Review of scientific instruments*, vol. 69, no. 11, pp. 3737–3740, 1998.

[129] T. Kessler, *Development and application of laser technologies at radioactive ion beam facilities*. No. 8/2008, University of Jyväskylä, 2008.

[130] S. Geldhof, P. Campbell, B. Cheal, R. de Groote, W. Gins, and I. Moore, "Collinear laser spectroscopy of stable palladium isotopes at the igisol facility," *Hyperfine Interactions*, vol. 241, no. 1, pp. 1–9, 2020.

[131] W. Gins, R. P. de Groote, M. L. Bissell, C. G. Buitrago, R. Ferrer, K. M. Lynch, G. Neyens, and S. Sels, "Analysis of counting data: Development of the satlas python package," *Computer Physics Communications*, vol. 222, pp. 286–294, 2018.

[132] B. Efron, "Computers and the theory of statistics: thinking the unthinkable," *SIAM review*, vol. 21, no. 4, pp. 460–480, 1979.

[133] A. Voss, V. Sonnenschein, P. Campbell, B. Cheal, T. Kron, I. D. Moore, I. Pohjalainen, S. Raeder, N. Trautmann, and K. Wendt, "High-resolution laser spectroscopy of long-lived plutonium isotopes," *Phys. Rev. A*, vol. 95, p. 032506, Mar 2017.

[134] S. Geldhof, M. Kortelainen, O. Beliuskina, P. Campbell, L. Caceres, L. Cañete, B. Cheal, K. Chrysalidis, C. Devlin, R. de Groote, *et al.*, "Impact of nuclear deformation and pairing on the charge radii of palladium isotopes," *Physical Review Letters*, vol. 128, no. 15, p. 152501, 2022.

[135] A. Steudel, "Die hyperfeinstruktur im pd i-spektrum und die kernmomente des pd105," *Zeitschrift für Physik*, vol. 132, no. 4, pp. 429–445, 1952.

[136] E. Bhattacharyya, "Decay of105ag," *Il Nuovo Cimento (1955-1965)*, vol. 24, no. 6, pp. 1000–1005, 1962.

[137] B. Nyman, J. Sieniawski, and H. Pettersson, "Internal conversion and gamma-ray studies of the decay of 101pd," *Physica Scripta*, vol. 5, no. 1-2, p. 13, 1972.

[138] M. Huyse, K. Cornelis, G. Lhersonneau, J. Verplancke, W. Walters, K. Heyde, P. Van Isacker, M. Waroquier, G. Wenes, and H. Vincx, "The decay of mass-separated 99g, mag," *Nuclear Physics A*, vol. 352, no. 2, pp. 247–266, 1981.

[139] H. Penttilä, T. Enqvist, P. Jauho, A. Jokinen, M. Leino, J. Parmonen, J. Äystö, and K. Eskola, "β-decay of 113rh and the observation of 113mpd: Isomer systematics in odd-a palladium isotopes," *Nuclear Physics A*, vol. 561, no. 3, pp. 416–430, 1993.

[140] N. Stone, "Table of nuclear magnetic dipole and electric quadrupole moments," *Atomic Data and Nuclear Data Tables*, vol. 90, no. 1, pp. 75–176, 2005.

[141] D. T. Yordanov, D. Balabanski, M. Bissell, K. Blaum, A. Blazhev, I. Budinčević, N. Frömmgen, C. Geppert, H. Grawe, M. Hammen, *et al.*, "Spins and electromagnetic moments of cd 101–109," *Physical Review C*, vol. 98, no. 1, p. 011303, 2018.

[142] Y. Luo, J. Rasmussen, J. Hamilton, A. Ramayya, S. Frauendorf, J. Hwang, N. Stone, S. Zhu, N. Brewer, E. Wang, *et al.*, "New insights into the nuclear structure in neutron-rich 112,114,115,116,117,118 pd," *Nuclear Physics A*, vol. 919, pp. 67–98, 2013.

[143] A. Esmaylzadeh, V. Karayonchev, G. Häfner, J. Jolie, M. Beckers, A. Blazhev, A. Dewald, C. Fransen, A. Goldkuhle, L. Knafla, *et al.*, "Triaxiality in the mid-shell nucleus pd 112," *Physical Review C*, vol. 103, no. 5, p. 054324, 2021.

[144] M. Kortelainen, J. McDonnell, W. Nazarewicz, E. Olsen, P.-G. Reinhard, J. Sarich, N. Schunck, S. Wild, D. Davesne, J. Erler, *et al.*, "Nuclear energy density optimization: Shell structure," *Physical Review C*, vol. 89, no. 5, p. 054314, 2014.

[145] R. De Groote, J. Billowes, C. L. Binnersley, M. L. Bissell, T. E. Cocolios, T. Day Goodacre, G. J. Farooq-Smith, D. Fedorov, K. T. Flanagan, S. Franchoo, *et al.*, "Measurement and microscopic description of odd–even staggering of charge radii of exotic copper isotopes," *Nature Physics*, vol. 16, no. 6, pp. 620–624, 2020.

[146] S. Eliseev, K. Blaum, M. Block, C. Droese, M. Goncharov, E. M. Ramirez, D. Nesterenko, Y. N. Novikov, and L. Schweikhard, "Phase-imaging ion-cyclotron-resonance measurements for short-lived nuclides," *Physical Review Letters*, vol. 110, no. 8, p. 082501, 2013.

[147] *M. Reponen private communication.*

[148] F. Déchery, H. Savajols, M. Authier, A. Drouart, J. Nolen, D. Ackermann, A. Amthor, B. Bastin, A. Berryhill, D. Boutin, *et al.*, "The super separator spectrometer s3 and the associated detection systems: Sirius & leb-reglis3," *Nuclear Instruments and Methods in Physics Research Section B: Beam Interactions with Materials and Atoms*, vol. 376, pp. 125–130, 2016.

[149] A. Villari, A. Drouart, J. Nolen, and S. collaboration, "S3: the super separator spectrometer for linag," in *AIP Conference Proceedings*, vol. 912, pp. 436–445, American Institute of Physics, 2007.

[150] N. Karkour, B. Sulignano, J. Piot, H. Savagols, A. Drouart, M. Authier, V. Alaphilippe, A. Boujrad, P. Brionnet, T. Chaminade, *et al.*, "Sirius project (spectroscopy & identification of rare isotopes using s3)," in *2016 IEEE Nuclear Science Symposium, Medical Imaging Conference and Room-Temperature Semiconductor Detector Workshop (NSS/MIC/RTSD)*, pp. 1–6, IEEE, 2016.

[151] P. Chauveau, P. Delahaye, G. De France, S. El Abir, J. Lory, Y. Merrer, M. Rosenbusch, L. Schweikhard, and R. Wolf, "Pilgrim, a multi-reflection time-of-flight mass spectrometer for spiral2-s3 at ganil," *Nuclear Instruments and Methods in Physics Research Section B: Beam Interactions with Materials and Atoms*, vol. 376, pp. 211–215, 2016. Proceedings of the XVIIth International Conference on Electromagnetic Isotope Separators and Related Topics (EMIS2015), Grand Rapids, MI, U.S.A., 11-15 May 2015.

[152] J.-C. Thomas and B. Blank, "The desir facility at spiral2," in *Nuclear Structure Problems*, pp. 224–229, World Scientific, 2013.

[153] E. Van Duijn, S. Witte, R. Zinkstok, and W. Hogervorst, "Hyperfine structure and isotope shift measurements on 4d10 1s0→ 4d9 5p j= 1 transitions in pd i using deep-uv cw laser spectroscopy," *The European Physical Journal D-Atomic, Molecular, Optical and Plasma Physics*, vol. 19, no. 1, pp. 25–29, 2002.

[154] M. Baig, A. Rashid, Z. Iqbal, and J. Hormes, "High resolution absorption spectrum of palladium in the 4d subshell excitation region," *Journal*

of Physics B: Atomic, Molecular and Optical Physics, vol. 24, no. 9, p. 2295, 1991.

[155] T. Kobayashi, C. R. Locke, and K. Midorikawa, "Spectroscopic investigation of autoionizing rydberg states of palladium accessible after odd-mass-selective laser excitation," *Japanese Journal of Applied Physics*, vol. 56, no. 1, p. 010302, 2016.